

**FAULT DETECTION AND DIAGNOSIS:  
APPLICATION IN MICROELECTROMECHANICAL  
SYSTEMS**

DOCTORAL DISSERTATION  
OF

VASILIKI REPPA

DIPLOMA IN ELECTRICAL AND COMPUTER ENGINEERING

UNIVERSITY OF PATRAS  
DEPARTMENT OF ELECTRICAL AND COMPUTER ENGINEERING

DISSERTATION No: 250

JULY 2010



## CERTIFICATION

This is to certify that VASILIKI REPPA, who received her Diploma in Electrical and Computer Engineering from the University of Patras, defended her Doctoral dissertation, entitled

**«FAULT DETECTION AND DIAGNOSIS: APPLICATION IN MICROELECTROMECHANICAL SYSTEMS»**

in public on the 8<sup>th</sup> of July, 2010, in the Department of Electrical and Computer Engineering, at the University of Patras. The Doctoral dissertation was examined and approved by the 7-faculty member examination committee:

**Kostas Berberidis**, Professor in the Computer Engineering and Informatics Department of the University of Patras

**Evangelos Dermatas**, Associate Professor in the Electrical and Computer Engineering Department of the University of Patras

**Petros Groumpos**, Professor in the Electrical and Computer Engineering Department of the University of Patras, member of the 3-supervising committee

**Demosthenes Kazakos**, Assistant Professor in the Electrical and Computer Engineering Department of the University of Patras

**Nick Koussoulas**, Professor in the Electrical and Computer Engineering Department of the University of Patras, member of the 3-supervising committee

**Triantafillos Pimenides**, Professor in the Electrical and Computer Engineering Department of the University of Patras,

**Anthony Tzes**, Professor in the Electrical and Computer Engineering Department of the University of Patras, principal supervisor, head of the 3-supervising committee

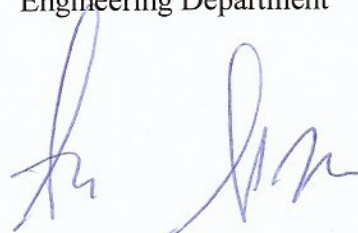
Patras, 8<sup>th</sup> of July, 2010

Principal Supervisor



A. Tzes

Head of the Electrical and Computer Engineering Department



A. Tzes



*To my parents, Maria and Dimitris*



## ACKNOWLEDGEMENT

All my life I set goals and exerted efforts to achieve them. One of the major goals was to complete my doctoral dissertation. In order to manage it, I realized that except from studying, I should have patience, persistence, as well as critical mind and good perception. Certainly, these wouldn't be enough, if some people didn't assist and support me and give me the opportunity to collaborate with them. Through this dissertation, I have the chance to express a public "thank you" to all of them.

First of all, I am especially grateful to Prof. Anthony Tzes for agreeing to supervise my doctoral studies with a very interesting research objective. The completeness of my doctoral thesis would be unattainable without his scientific guidance, his support and his confidence in me and my work, especially when I had lost mine. With his enthusiasm and insatiable thirst for knowledge, his will to expand his research activities and his encouragement to attend international conferences in order to broaden my research horizons, he made me want to pursue research after my doctoral studies.

I would like to thank the other members of the examination committee, Prof. Petros Groumpos, Prof. Evangelos Dermatas, Prof. Demosthenes Kazakos, Prof. Nick Koussoulas, Prof. Kostas Berberidis and Prof. Triantafillos Pimenides for their time and recommendations. Particularly, I would like to thank Prof. Groumpos as President and CEO of Patras Scientific Park for giving me the opportunity to work in many innovative projects and Dr. Chrysostomos Stylios, Research and Development Consultant of Patras Scientific Park for his collaboration in these projects.

I was very fortunate to work in a very pleasant environment, created by the former and current labmates, George Nikolakopoulos, George Georgoulas, Nancy Panousopoulou, Themis Kolyvas, Yannis Koveos, Nikos Athanasopoulos, Marialena Vagia, John Stergiopoulos, Kostas Alexis, Eleni Kelasidi and John Arvanitakis. I would like to thank them for the very pleasant coffee and lunch breaks, their support and help. Particularly, I'm indebted to Nancy, Themis and Yannis, because we spent many nights and weekends working at the lab and they were always willing to answer my questions and give solutions not only to scientific problems. I would like to express a big "thank you" to Konstantinos Koutroumpas for his emotional and psychological support and understanding especially during the last year of my doctoral dissertation, as well as for the fact that he was the "clear mind" that I needed when everything seemed confusing.

During the course of my doctoral studies, I joined the Storage Technologies Department of IBM Zurich Research Laboratory as a student intern. I am thankful to Dr. Evangelos Eleftheriou, Manager of Storage Technologies Department and Dr. Haris Pozidis, Manager of Memory and Probe Technologies Group for giving me the opportunity to work in an international environment and gain experimental experience. I would like to thank Dr. Abu Sebastian, Dr. Aggeliki Pantazi and especially Dr. Deepak R. Sahoo for teaching me and helping me understand the experiments and apply the fault detection and diagnosis techniques.

I am grateful that my doctoral studies were the reason for knowing new people, getting closer to some others and making very good collaborations. However, I met some people in my school and undergraduate years that they were always by my side. I would like to thank my friends Nicky Koffa and Ioulietta Zindrou, because since we were little we learned to make dreams and try always for the best. I would like to thank Nicky not only for her 23-years friendship, but also because she and her husband Tassos Stratis remind me that life is not only working and studying. Furthermore, I would like to thank my friends Marina Maniadi and George Thomou, and Alekos Ntounas for their support, assistance and protection that gave me since the first time in Patras.

Finally, I would like to express my deepest gratitude to my parents, Maria and Dimitris and to them I dedicate this thesis. I thank them for the values with which they raised me and the sacrifices they made in order to accomplish my goals. I thank them for supporting my choices and standing by me in joy and sorrow. They made me what I am today.



---

This doctoral thesis was partially supported by "C. Carathéodory" initiative research program of University of Patras (C. 152).



# CONTENTS

<b>ABSTRACT</b>	<b>xiv</b>
<b>Nomenclature</b>	<b>xvii</b>
<b>1 Introduction</b>	<b>1</b>
1.1 Review of Fault Detection and Diagnosis Methods . . . . .	1
1.1.1 Fault Detection Methods . . . . .	3
1.1.2 Fault Diagnosis Methods . . . . .	7
1.2 Review of MEMS Failure Modes and Detection Methods . . . . .	10
1.3 Dissertation Objective . . . . .	14
1.3.1 Review of Related Literature . . . . .	15
1.3.2 Contribution of the Dissertation . . . . .	20
1.3.3 Structure of the Dissertation . . . . .	21
<b>2 Set Membership Identification</b>	<b>23</b>
2.1 Introduction . . . . .	23
2.2 Modeling Assumptions . . . . .	24
2.3 Ellipsoid and Orthotope Preliminaries . . . . .	25
2.3.1 Orthotope . . . . .	25
2.3.2 Ellipsoid and Support Orthotope . . . . .	26
2.4 Data-Generated Hyperspace . . . . .	27
2.4.1 Data-hyperstrip . . . . .	27
2.4.2 Data-hypersector . . . . .	28
2.5 Set Membership Identification . . . . .	30
2.5.1 Orthotope-based Set Membership Identification . . . . .	30
2.5.2 Ellipsoid-based Set Membership Identification . . . . .	32
2.5.2.1 Ellipsoid-SMI using data-hyperstrips . . . . .	33
2.5.2.2 Ellipsoid-SMI using data-hypersectors . . . . .	35
2.5.3 Data-Hyperspace Configuration Selection for Optimal SMI . . . . .	36
2.6 Special Cases . . . . .	37
2.6.1 Time Invariant Parameters . . . . .	37
2.6.2 Equation Error . . . . .	39
2.7 Conclusions . . . . .	39

---

<b>3</b>	<b>Fault Detection and Diangosis</b>	<b>41</b>
3.1	Introduction . . . . .	41
3.2	Fault Detection and Diagnosis Assumptions . . . . .	41
3.3	Fault Detection Procedure . . . . .	43
3.4	Fault Diagnosis Procedure . . . . .	44
3.4.1	Fault Isolation Procedure . . . . .	49
3.4.1.1	Fault Isolation based on Orthotopic SMI . . . . .	49
3.4.1.2	Fault Isolation based on ellipsoidal SMI . . . . .	52
3.4.2	Fault Identification Procedure . . . . .	54
3.4.2.1	Fault Identification based on Orthotopic SMI . . . . .	54
3.4.2.2	Fault Identification based on ellipsoidal SMI . . . . .	54
3.5	Special Case:Time Invariant Parameters . . . . .	54
3.5.1	Fault Detection Procedure . . . . .	55
3.5.2	Fault Diagnosis Procedure . . . . .	56
3.5.2.1	Fault Isolation Procedure . . . . .	61
3.5.2.2	Fault Identification Procedure . . . . .	62
3.6	Fault Detection and Diagnosis Issues . . . . .	63
3.6.1	Undetected Faults . . . . .	63
3.6.1.1	Undetected faults in the Orthotope-based Fault Detection Procedure . . . . .	63
3.6.1.2	Undetected faults in Ellipsoid-based Fault Detec- tion Procedure . . . . .	63
3.6.2	Backward-in-time fault detection procedure . . . . .	64
3.6.2.1	Orthotope-based Backward-in-Time Fault Detection . . . . .	64
3.6.2.2	Ellipsoid-based Backward-in-Time Fault Detection . . . . .	65
3.6.3	Characterization of Algorithm Sensitivity . . . . .	69
3.7	Conclusions . . . . .	71
<b>4</b>	<b>Fault Detection and Diagnosis applied in Microelectromechanical Systems</b>	<b>73</b>
4.1	Introduction . . . . .	73
4.2	Parallel-Plate Electrostatic Micro-Actuator . . . . .	74
4.3	Torsional Resonant Atomic Force Microscope . . . . .	82
4.3.1	Lumped-Parameter Modelling . . . . .	82
4.3.2	Detection and Diagnosis of Tip-Fractures . . . . .	86
4.4	Conclusions . . . . .	93
<b>5</b>	<b>Concluding Remarks</b>	<b>95</b>
5.1	Conclusions . . . . .	95
5.2	Areas for Further Research . . . . .	97
5.3	Dissertation Publications . . . . .	98
	<b>Bibliography</b>	<b>100</b>

---

---

<b>A</b>	<b>Mathematical Auxiliary Analysis</b>	<b>109</b>
A.1	Computation of the Perturbation Ellipsoid . . . . .	109
A.2	Time Invariant Jump Linearly Parametrizable Model . . . . .	110
A.3	Proof of Theorem II.3.6.2 . . . . .	110
A.4	Computation of Modal-Shape of Torsional Resonant AFM . . . . .	112
<b>B</b>	<b>Algorithms</b>	<b>115</b>
B.1	OVE-based Algorithms . . . . .	115
B.2	Backward-in-Time Fault Detection Algorithm . . . . .	117

## LIST OF FIGURES

1.1	Location of faults. . . . .	2
1.2	Time dependency of faults. . . . .	3
1.3	Physical and model based fault diagram. . . . .	4
1.4	Classification of fault detection methods . . . . .	5
1.5	a) Physical-based fault-symptom relationship, b) Diagnosis-based symptom-fault relationship [1]. . . . .	9
1.6	Classification of fault diagnosis methods . . . . .	11
1.7	Time evolution of parametric fault . . . . .	14
1.8	Different representations of the parametric sets approximating the feasible parameter set ( $n=2$ ) . . . . .	16
2.1	Outer bounding parametric sets ( $n=2$ ): a) orthotope, b) ellipsoid and support orthotope . . . . .	25
2.2	Graphical representation of data-hyperstrip ( $n=2$ ) . . . . .	28
2.3	Graphical representation of the data-hypersector ( $n=2$ ) . . . . .	30
2.4	Graphical representation of the computation of $\Omega(i)$ using: a) data-hyperstrips and b) data-hypersectors ( $n=2$ ) . . . . .	32
2.5	Graphical representation of the data-hyperstrip and the support hyperplanes of ellipsoid ( $n=2$ ) . . . . .	34
2.6	Graphical representation of the computation of $\Theta(i)$ using a data-hyperstrip ( $n=2$ ) . . . . .	35
2.7	Graphical representation of the computation of $\Theta(i)$ using data-hypersectors ( $n=2$ ) . . . . .	36
2.8	An example of empty intersection $\hat{\Theta}(i)$ and $S^{np}(i)$ ( $n=2$ ) . . . . .	37
2.9	Feasible parameter set generated by a) data-hyperstrips, b) data-hypersectors ( $n=2$ ) . . . . .	38
3.1	Graphical representation of the jump-parameter case ( $n = 2$ ). . . . .	42
3.2	Graphical representation of fault detection based on the empty intersection between an orthotope and: a) a data-hyperstrip, b) a data-hypersector ( $n = 2$ ). . . . .	44
3.3	Graphical representation of fault detection based on the empty intersection between an ellipsoid and: a) a data-hyperstrip, b) a data-hypersector ( $n = 2$ ) . . . . .	44

---

3.4	Detected fault case and orthotope-based resetting procedure ( $n = 2$ ).	48
3.5	Detected fault case and ellipsoid-based resetting procedure ( $n = 2$ ).	48
3.6	Graphical representation of the worst case orthotopes, $\hat{\Omega}(i_1 i_0)$ , and the orthotopes arisen from the normal operation of the SMI (Section 2.5.1), $\Omega(i_1)$ . . . . .	51
3.7	Graphical representation of the computation of the intersection of support orthotopes ( $n = 2$ ). . . . .	57
3.8	Activation of the FD-criterion using orthotopes with $i^{d_j} = i^{f_j}$ ( $n = 2$ ).	57
3.9	Resetting procedure based on the intersection of support orthotopes ( $n = 2$ ) . . . . .	61
3.10	Fault isolation example ( $n = 2$ ) . . . . .	62
3.11	Undetected fault case ( $n = 2$ ). . . . .	64
3.12	Incorrect time instant of fault detection in case of orthotopic FDD ( $n = 2$ ). . . . .	65
3.13	‘Backward-in-time’ fault detection procedure in case of orthotopic FDD ( $n = 2$ ). . . . .	66
3.14	Incorrect time instant of fault detection in case of ellipsoidal FDD ( $n = 2$ ) . . . . .	66
3.15	Fault detection example ( $n = 2$ ). . . . .	68
3.16	Backward-in-time fault detection example ( $n = 2$ ). . . . .	69
4.1	a) Simplified testbed layout and b) mass-spring-damper model of a parallel-plate electrostatic micro-actuator. . . . .	75
4.2	Fault detection case via the (D) scheme at $i^{d5} = 6001$ . . . . .	77
4.3	Empty intersection case between $\mathcal{X}(6000)$ and $\Omega^\Theta(6001)$ . . . . .	78
4.4	Electrostatic microactuator–Time evolution of upper and lower bounds of $\theta_1^\circ$ generated by the FDD schemes. . . . .	78
4.5	Electrostatic microactuator–Time evolution of upper and lower bounds of $\theta_2^\circ$ generated by the FDD schemes. . . . .	79
4.6	Electrostatic microactuator–Time evolution of upper and lower bounds of $\theta_3^\circ$ generated by the FDD schemes. . . . .	79
4.7	Fault Identification of microactuator parameter vector . . . . .	81
4.8	Schematic diagram of a torsionally resonant AFM interacting with a sample surface . . . . .	82
4.9	TR-AFM–Time evolution of upper and lower bounds of $\theta_1^\circ$ generated by the FDD schemes. . . . .	89
4.10	TR-AFM–Time evolution of upper and lower bounds of $\theta_2^\circ$ generated by the FDD schemes. . . . .	89
4.11	TR-AFM–Fault detection of $\theta_1^\circ(i)$ applying (B) and (D) FDD schemes.	90
4.12	TR-AFM–Fault detection of $\theta_2^\circ(i)$ applying (B) and (D) FDD schemes.	91
4.13	TR-AFM–Fault detection and isolation of $c_l(i)$ applying (B) and (D) FDD schemes. . . . .	92

---

---

4.14	TR-AFM–Fault detection and isolation of $R_t(i)$ applying (B) and (D) FDD schemes. . . . .	92
4.15	TR-AFM–Fault identification of $R_t(i)$ applying (B) and (D) FDD schemes. . . . .	93



## LIST OF TABLES

1.1	Qualitative evaluation of theoretical process model-based FD techniques [1] . . . . .	8
1.2	MEMS failure mechanisms and modes . . . . .	12
4.1	Electrostatic Micro-actuator Fault Instances . . . . .	76
4.2	Electrostatic Micro-actuator–Time Instances of Fault Occurrence and Detection . . . . .	77
4.3	Electrostatic Micro-actuator Parameter Vector Isolation Instants . . . . .	80
4.4	TR-AFM–Time Instances of Fault Occurrence and Detection . . . . .	88

## ABSTRACT

Supervisory control schemes incorporated in complex systems aim at maximizing reliability, safety and quality, while minimizing downtime and cost of manufacturing. However, all these requirements are affected by the occurrence of faults, giving rise to the application of fault detection and diagnosis modules. In order to increase the efficiency of these methods, their design should be realized by: a) gaining a deep understanding of what kind of faults are expected to occur in the system under investigation and how they are going to evolve, and b) by selecting the feature that describes the status of the system and will change due to a fault.

This thesis presents the development of a fault detection and diagnosis (FDD) procedure capable of capturing, isolating and identifying multiple abrupt parametric faults. The proposed method relies on parameter estimation deployed in a set membership framework. This approach presupposes the utilization of a linearly parametrizable model and the a priori knowledge of bounded noise errors and parameter perturbations. Under these assumptions, a data-hyperspace is generated at every time instant. The goal of set membership identification (SMI) is the determination of the parametric set, formed as an orthotope or ellipsoid, within which the nominal parameter vector resides and intersects with the data-hyperspace.

The fault detection mechanism is activated when the normal operation of the SMI procedure is interrupted due to an empty intersection of the data-hyperspace and the estimated parametric set. At the detection instant, a resetting procedure is performed in order to compute the parameter set and the data-hyperspace that contain the varied nominal parameter vector, allowing the SMI algorithm to continue its operation. During the fault isolation, consistency tests are executed, relying on the projections of the worst case parametric sets and the ones arisen from the normal operation of SMI. A faulty component is indicated when these projections do not intersect, while the distance of their centers is used for fault identification. In case of the ellipsoidal SMI-based FDD and under the assumption of a time invariant parameter vector, a new fault detection criterion is defined based on the intersection of support orthotopes of ellipsoids. A more accurate estimation of the time instant of fault occurrence is proposed based on the application of a backward-in-time procedure starting from the fault detection instant, while the conditions under which a fault will never be detected by the orthotopic and ellipsoidal SMI based FDD are provided.

This dissertation explores the efficiency of the proposed FDD methodology for capturing failure modes of two microelectromechanical systems; an electrostatic parallel-plate microactuator and a torsionally resonant atomic force microscope. The need for applying a FDD procedure in a microactuator emanates from the fact that this device is embedded in other MEMS devices and possible abnormal operation may cause severe damages. On the other hand, the TR-AFM is utilized for investigating the tribological phenomena of materials and generating high resolutions 3D images

of the samples. When failure modes appear in its tip, the quality of these images is affected, inferring wrong information about the materials' properties. From an engineering point of view, failure modes appeared in the microcomponents of the microactuator and the TR-AFM are encountered as parameter variations and are captured, isolated and identified by the proposed FDD methodology.

---

---

# Nomenclature

- $\hat{\Omega}(i)$  augmented orthotope
- $\hat{\Omega}(i_1 | i_0)$  worst-case orthotope
- $\hat{\Omega}^\Theta(i_1 | i_0)$  worst-case support orthotope of  $\Theta(i_1 | i_0)$
- $\hat{\Omega}_u(i_1 | i_0)$  projection of  $\hat{\Omega}(i_1 | i_0)$  on the  $u$  axis
- $\hat{\Omega}_u^\Theta(i_1 | i_0)$  projection of  $\hat{\Omega}^\Theta(i_1 | i_0)$  on the  $u$  axis
- $\hat{\Theta}(i)$  augmented ellipsoid
- $\mathcal{X}(i)$  intersection of orthotopes
- $\mathcal{X}_u(i)$  projection of  $\mathcal{X}(i)$  on the  $u$ th axis
- $\Omega(i)$  orthotope
- $\Omega^r(i)$  resetting orthotope
- $\Omega^w(i)$  perturbation orthotope
- $\Omega^\Theta(i)$  support orthotope of  $\Theta(i)$
- $\Omega_u(i)$  projection of  $\Omega(i)$  on the  $u$ th axis
- $\Omega_u^\Theta(i)$  projection of  $\Omega^\Theta(i)$  on the  $u$ th axis
- $\phi(i)$  noise-free regression vector of linearly parametrizable model
- $\phi^m(i)$  observed regression vector of linearly parametrizable model
- $\Theta(i)$  ellipsoid
- $\theta^c(i)$  center of  $\Theta(i)$
- $\Theta^r(i)$  resetting ellipsoid
- $\Theta^w(i)$  perturbation ellipsoid

- 
- $\theta^\circ(i)$  nominal parameter vector  
 $\theta_u^\circ(i)$   $u$ th component of  $\theta^\circ(i)$   
 $\theta_{\mathcal{X}_u}^c(i)$  center of  $\mathcal{X}_u(i)$   
 $\theta_{\mathcal{X}_u}^-(i), \theta_{\mathcal{X}_u}^+(i)$  coordinates of  $\mathcal{X}(i)$ 's vertices  
 $\theta_{\mathcal{X}}^c(i)$  center of  $\mathcal{X}(i)$   
 $\theta_{\Omega^\Theta}^c(i)$  center of  $\Omega^\Theta(i)$   
 $\theta_{\Omega_u^\Theta}^c(i)$  center of  $\Omega_u^\Theta(i)$   
 $\theta_{\Omega_u^\Theta}^-(i), \theta_{\Omega_u^\Theta}^+(i)$  coordinates of  $\Omega^\Theta(i)$ 's vertices  
 $\theta_{\Omega_u}^c(i)$  center of  $\Omega_u(i)$   
 $\theta_{\Omega_u}^-(i), \theta_{\Omega_u}^+(i)$  coordinates of  $\Omega(i)$ 's vertices  
 $\theta_\Omega^c(i)$  center of  $\Omega(i)$   
 $e_y(i)$  ( $e_y^{\max}$ ) output error (worst-case bound)  
 $e_{\phi_u}(i)$  ( $e_{\phi_u}^{\max}$ ) measurement noise corrupting the  $u$ th component of regression vector (worst case bound)  
 $F(i)$  feasible parameter set  
 $n$  length of parameter vector  
 $P(i)$  shape matrix of  $\Theta(i)$   
 $S(i)$  data-hyperspace  
 $S^{mp}(i)$  data-hypersector  
 $S^p(i)$  data-hyperstrip  
 $w(i)$  parameter perturbation vector  
 $w_u(i), (w_u^{\min}, w_u^{\max})$   $u$ th component of  $w(i)$  (worst-case bounds)  
 $y(i)$  noise-free output of linearly parametrizable model  
 $y^m(i)$  observed output of linearly parametrizable model  
 $\Theta(i_1 | i_0)$  worst-case ellipsoid
-

# Chapter 1

## Introduction

### 1.1 Review of Fault Detection and Diagnosis Methods

In recent years, in the automation industry, there has been a migration from classical control objectives such as stability and performance to less traditional ones like robustness and fault tolerance. The reason for reassessing the goals was the need for compensating the occurrence of **faults**, defined as *the unpermitted deviations of at least one characteristic property or parameter (**feature**) of the system from the acceptable, usual, standard condition*. The faults can emanate from: a) the wrong design and/or assembling, b) the improper operation or missing maintenance, and c) the material ageing, corrosion or wear during normal operation. The unavoidable occurrence of faults gives rise to the application of fault detection, isolation and identification modules.

The goals of fault detection [2], [3], [1], [4], [5], [6] is the determination of faults present in a system (in an extended definition) and their instant of detection. The procedure of finding the location of the fault is defined as fault isolation. In [2], [3], [1], the definition of fault isolation is extended to include the determination of the kind and the time of fault detection, while the fault identification is described as the procedure of determining the size and the time variant behavior of the fault. The determination of the size of the fault is also included in the definition of the fault identification provided in [5], [6], along with the assessment of the type (nature) of the fault and its cause. Finally, the combined isolation and the identification tasks are referred as fault diagnosis in [2], [4], [3], [1], while in [5], [6] the fault diagnosis includes also the detection mechanism.

Since an integrated system consists of mechanical and electrical components, electronic hardware and software, the possible **apparent physical faults** and the mechanisms that cause them are different between these system parts [1]. Faults of mechanical components may occur due to distortion (buckling, deformation), fatigue and fracture (cycle fatigue, thermal fatigue), wear (abrasive, adhesive, cavitation), or

## 1. INTRODUCTION

---

corrosion (galvanic, chemical, etc.) and may evolve in a drift-like manner (wear, corrosion), or abruptly (distortion, fracture)). On the other hand, electrical components usually consist of a large number of sub-components with various failure modes, like short-cuts, loose or broken connections, parameter changes, contact problems, contamination, etc. Generally, faults in electrical components appear more randomly than the mechanical faults. Faults in electronic hardware exhibit a systematic behavior and mainly stem from specification or design mistakes. Finally, software faults (bugs) occur due to incorrect specification, coding, logics, calculation overflow, etc.

Under the fault-relevant knowledge, the first step of the FDD design is the **fault modelling**, which describes how the physical faults can be reflected to the process models. Consider the generic system description

$$Y(t) = g(U(t), x(t), \theta), \quad (1.1)$$

where  $Y(t)$ ,  $U(t)$ ,  $x(t)$  are the output, input and state signal variables and  $\theta$  parameter vector. The faults are characterized as **additive**, when correspond to unknown inputs acting on the process, which affect the process outputs and are independent of the known inputs [4]. An example of an additive fault is presented in Fig. 1.1a [1], where:

$$Y(t) = Y^\circ(t) + \Delta Y(t) = Y^\circ(t) + f(t). \quad (1.2)$$

The faults are characterized as **multiplicative (parametric)**, when correspond to variations in some process parameters that affect the process outputs and depend on the magnitude of the known inputs [4]. An example of a multiplicative fault is depicted in Fig. 1.1b [1], where for  $\theta = a$ ,

$$Y(t) = (a + \Delta a(t))U(t) = aU(t) + \Delta a(t)U(t) = Y^\circ(t) + f(t)U(t). \quad (1.3)$$

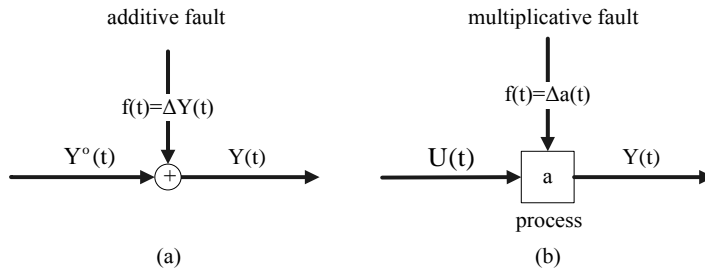


**Figure 1.1:** Location of faults.

Moreover, the fault modelling is complemented using the available information about the expected time evolution of the fault. Specifically, a fault is characterized as:



a) **abrupt** (stepwise) (Fig. 1.2a), when occurs suddenly and remains for the rest of the system operation (**permanent** fault) or remains for a finite time window (**transient** fault) [7], b) **incipient** (Fig. 1.2b), when evolves gradually, [8] and c) **intermittent** (Fig. 1.2c), when occurs and vanishes suddenly for a number of aperiodic finite time windows [9].

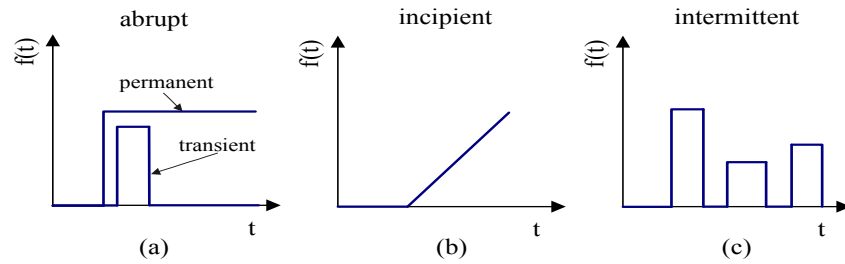


Figure 1.2: Time dependency of faults.

### 1.1.1 Fault Detection Methods

The fault modelling procedure is followed by the selection of the most appropriate Fault Detection (FD) method according to the available measurable signals and the mathematical models [1]. The construction of a mathematical model can be realized via theoretical or experimental analysis. The **theoretical models** are based on the mathematical formulation of the laws of nature and can be distinguished in static or dynamic and continuous-time or discrete-time models. However, due to the complexity of the resulted theoretical model, further simplifications may be needed. A common simplification is the transition from the partial differential equations that describe the time and space dependency of distributed parameter systems to ordinary differential equations that describe lumped parameter systems, by limiting the parameters on a fixed location. On the other hand, **experimental models** express the mathematical relationship between measured input and output signals, which is subsequently evaluated using identification methods. It has to be mentioned that the theoretical models contain the functional description between the physical data of the process and its parameters, while the experimental ones contain parameters as numerical values, whose functional relationship with the physical data of the process is undefined. Therefore, the utilization of theoretical models has the advantage of determining the mathematical relationship between the model parameter vector  $\theta$  and the physical parameter vector  $p$  via nonlinear algebraic equations  $\theta = h(p)$ , as depicted in Fig. (1.3). If there is one-to-one mapping between the physical and model parameters, the isolation of a fault in physical parameters can be accomplished by using the estimates of the model parameters.

## 1. INTRODUCTION

---

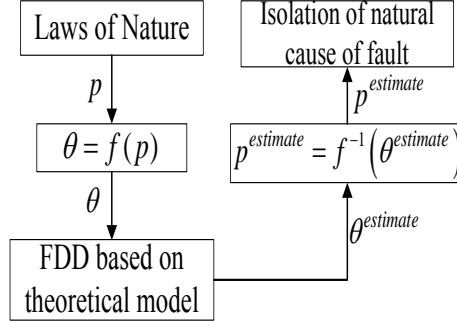
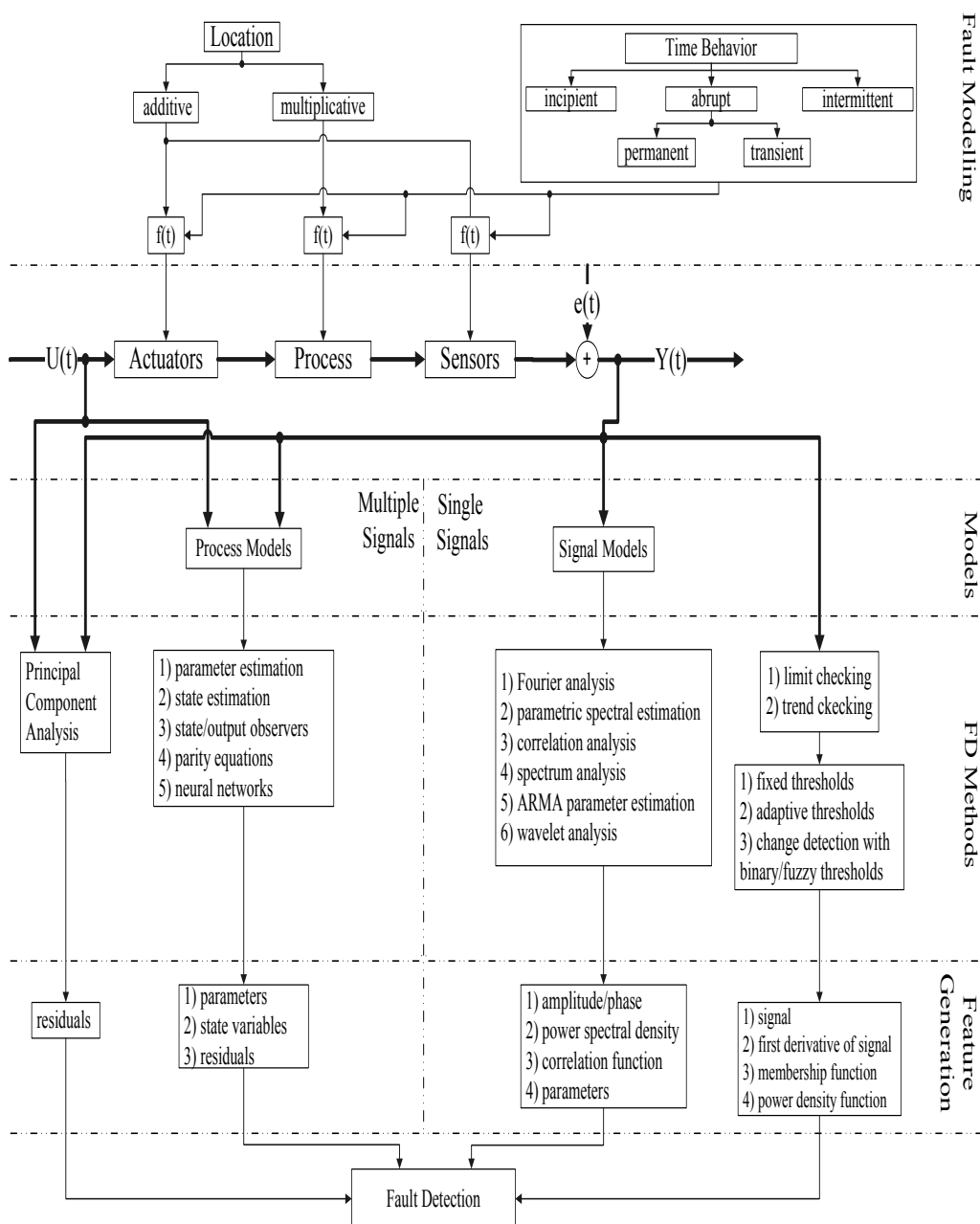


Figure 1.3: Physical and model based fault diagram.

The most common FD methods can be assorted according to the number of the measurable signals and utilized models, as shown in Fig. 1.4. The simplest FD procedure uses a single signal, the process output  $Y(t)$ , under the assumption that a fault somewhere in the process will be perceptible as change in  $Y(t)$ . The goal of this procedure is to compare the monitored signal  $Y(t)$  (**limit checking**) or its first derivative  $\dot{Y}(t)$  (**trend checking**) in relation to thresholds, which can be fixed or adaptive. The power density function and membership function of  $Y(t)$  may also be used as features for fault detection, being compared with thresholds (change detection) [10], [11]. In the case that multiple measured signals are available, but the high computer effort and the high data correlation (i.e. chemical plants) do not ‘allow’ the utilization of a model, **principal component analysis** is applied. The main concept of this method is the projection of the original process data onto a smaller number of principal components, based on the fact that a small number of faults produce unusual patterns. The faults are supposed to be detected using residuals, created by the principal components [12], [13].

More sophisticated FD methods are assumed to be the signal and process model-based ones. **Signal model-based FD methods** utilize mathematical descriptions of periodic, stochastic and non-stationary signals. A periodical signal represented as single amplitude/ phase /frequency modulated oscillation, or superposition of oscillations, can be: a) developed in Fourier series, b) described by parametric signal models in frequency domain, or c) characterized by correlation functions. Correlation functions are also used in the case of stochastic signals, along with power spectral density and stochastic difference equations, while non-stationary signals are analysed by short-time Fourier transform or wavelets [14], [15], [16]. The objective of the signal model-based FD methods is to detect additive or multiplicative faults as changes in the signal features (amplitude, phase, power spectral density, correlation function) that are compared with the observed ones under faultless behavior.

## 1.1 Review of Fault Detection and Diagnosis Methods



**Figure 1.4:** Classification of fault detection methods

## 1. INTRODUCTION

---

**Process model-based FD methods** utilize multiple measured signals and experimental or theoretical models [17]. **Neural networks** have been employed using experimental models for FD [18]. The neural network approach has two phases, training and testing. During the first phase, the neural network is trained to define the underlying relationship between the measured inputs and outputs. After training, the neural networks are tested with a sample data set, which was not used during training. Once they are trained and tested, residuals are generated for fault detection, describing the discrepancies between the resulted experimental model and the process. The residuals are also used as features in the model-based FD methods based on **parity equations**, **state/output observers** and **state estimation**, in which continuous/discrete time state-space models or transfer functions are treated as the process models [19], [20]. The residuals' structure of the first two methods is very similar and differs only in the way that the input and output measurements are filtered. In the latter FD method, the residuals correspond to the difference between the output measurements and the output predicted using an old estimate. Finally, a very common process model-based FD technique that does not make use of residuals is based on **parameter estimation** [21]. The utilized model is based on a linear relationship between the parameters and the observations, given as:

$$y = \phi^T \theta, \quad (1.4)$$

where  $y$  is the model output,  $\phi$  is called the regression vector and  $\theta$  is the model parameter vector. The components of the parameter vector are functions of the physical parameters, while the model output  $y$  and the components of the regression vector are functions of measurable signals. This model is called **linearly parametrizable** (in the literature, it can be found as linear regression, regression form, linear in parameters or affine in parameters).

As shown in Fig. 1.4, the output of the signal/process model-based modules are treated as features describing the status of the process (e.g. parameters, state variables, residuals, correlation functions etc.). Hence, the fault detection methods seek to capture the unusual changes of the observable features from their nominal values. These quantifiable changes are denoted as **analytic symptoms**. Moreover, **heuristic symptoms** may be produced by using qualitative information from human operators. In addition, information about the process history, such as performed maintenance, repair, former faults, life cycle and load measures, or fault-statistical data gained from the experience investigating the same or similar processes are characterized as heuristic symptoms.

Process model-based FD methods can be further categorized based on the way that they treat 'variance' terms like noise affecting the data, and 'bias' terms like model errors, else system disturbances. **Statistical** approaches take into account the mean and variance of the amplitude probability density function (pdf) of the model errors, disturbances or noise, while the **deterministic** approaches consider the errors, disturbances or noise as unknown-but-bounded with known bounds. The choice

of the statistical or the deterministic strategy will have impact upon the feature generation.

A qualitative evaluation between process model-based FD techniques is summarized in Table 1.1 [4], relying on their design assumptions, fault detectability and general issues relevant to the process. Parity equations, observers and state estimation based FD methods have almost identical characteristics, but parity equations are simpler to be designed and implemented. In addition, sometimes instability in the detection procedure may emerge using state observer-based methods. The basic assumptions for all of them is the precise knowledge of the model structure and the invariant status of the parameters. On the other hand, in parameter estimation techniques, the model structure is assumed to be known and the parameters may be regarded not only as constant, but also as time-varying. All the process model-based FD methods need to know how the uncontrollable inputs are induced in the model (i.e. the way they are filtered). Parameter estimation methods can handle noise of medium magnitude, in contrast with the rest of the methods that can compensate small-magnitude noise.

Parameter estimation and parity equations may be used for fault detection in non-linear processes under certain assumptions and appropriate modifications. Moreover, the on-line real-time application of all the process model-based FD methods for fast processes is in general realizable. In case of the observer-based and state estimation methods, an increased number of observers is required. Multiple faults can be detected and isolated using parity equations and output observers only in MIMO processes. In case of state observers and state estimation, isolability may be feasible, if the information for faults is conveyed in the state variables.

Parity equations, observer and state estimation based-FD methods are very efficient in detecting additive faults in sensor and actuators. Parameter estimation is the most suitable method for detecting primarily multiplicative faults in the processes and faults which change the dynamics of sensors and actuators. Finally, model-based FD methods based on parameter estimation are very sensitive in small changes, while sometimes faults must be large enough so as to be detected by parity equations, observer and state estimation based methods.

### 1.1.2 Fault Diagnosis Methods

The objective of the fault diagnosis (FDs) procedure is the determination of the symptom to fault relationship, described as:

$$S \in \mathcal{S}^{n_s} \xrightarrow{\mathcal{M}} F \in \mathcal{F}^{n_f}, \quad (1.5)$$

where  $S$  is the symptom vector that contains all the available analytic and heuristic symptoms,  $F$  is the fault vector containing the possible theoretical faults reflected to parameters or signals and  $\mathcal{M}$  is assumed to be the diagnostic model, whose determination is based on the fault-relevant knowledge about the process.

## 1. INTRODUCTION

---

**Table 1.1:** Qualitative evaluation of theoretical process model-based FD techniques [4]

Comparison Criteria	Theoretical Process Model-based FD Techniques			
	Parity Equations	State Estimation		Parameter Estimation
		State Observer	Output Observer	
<b>assumptions</b>				
model structure	exactly known	exactly known		known
model parameters	known, constant	known, constant		unknown, constant or time-varying
models for unknown inputs	exactly known	exactly known		exactly known
noise	small	small		medium
stability of detection scheme	no problem	depends on the design	no problem	no problem
<b>detectable faults</b>				
additive faults	yes	yes		yes
parametric faults	no	no		yes
abrupt faults	yes	yes		yes
incipient faults	yes	yes		yes
multiple faults	SISO:no,MIMO:yes	SISO:no,MIMO:yes		SISO,MIMO:yes
fault isolation	SISO:no,MIMO:yes	SISO:no,MIMO:yes		SISO,MIMO:yes
<b>general</b>				
robustness in parameter changes	problematic	problematic		unproblematic
nonlinear processes	many classes possible	limited		many classes possible
nonlinear processes	many classes possible	limited		many classes possible
static processes	yes	no		straightforward
computational effort	small/medium	medium		medium/larger
closed loop	yes	yes		yes, external excitation

## 1.1 Review of Fault Detection and Diagnosis Methods

---

The "functional mapping relationship" follows in general a physical cause-effects relationship, as shown in Fig. 1.5. Figure 1.5a shows that a fault influences a number of events regarded as intermediate steps, which then influence the measurable or observable symptoms, both by internal physical properties (physical-based fault-symptom relationship). In case that the underline physical laws are unknown or too complicated for calculations, the fault diagnosis proceeds the reverse way, namely from the observed symptoms to the faults (diagnosis-based symptom-fault relationship) (Fig. 1.5b). This implies the inversion of causality. However, there are cases in which the intermediate events between faults and symptoms are not visible from the symptoms' behavior. The a priori knowledge of the fault-symptom causalities is called structured knowledge.

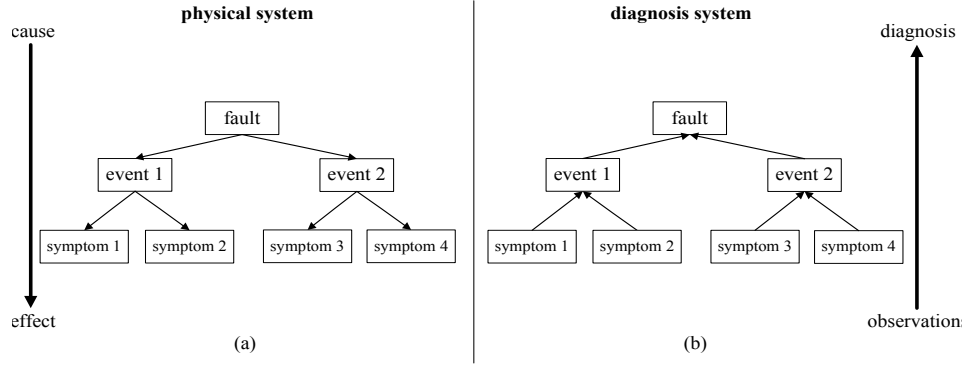


**Figure 1.5:** a) Physical-based fault-symptom relationship, b) Diagnosis-based symptom-fault relationship [4].

The FDs methods are distinguished based on the available fault-relevant knowledge about the process. If there is no information about the fault-symptom causalities (unstructured knowledge), **classification methods** are applied. Reference patterns  $S_{ref}$  are determined for the normal performance and the corresponding symptom vectors  $S$  are determined experimentally for certain faults  $F$ . The relationship between the fault vector  $F$  and  $S$  is therefore learned (or trained) experimentally and stored, forming an explicit knowledge base. Faults  $F$  can be captured by comparing the observed  $S$  with the normal reference  $S_{ref}$ . The classification-based FDs methods are categorized as: a) pattern recognition methods [22], b) statistical methods using Bayesian classifiers or decision trees [23], c) approximation methods using a polynomial classifier, d) density-based functions using a geometric classifier [24], and e) artificial intelligence methods, using fuzzy and/or neural net classifier [25].

If the basic relationships between the faults and the symptoms are at least partially known, **inference methods** can be applied for fault diagnosis. The qualitative knowledge of the physical-based fault-symptom and the diagnosis-based symptom-fault analysis can be expressed in form of rules: IF *condition* THEN *conclusion*. The

## 1. INTRODUCTION

---

condition part contains facts in the form of symptoms as inputs, and the conclusion part includes events and faults as a logical cause of the facts. If several symptoms indicate an event or fault, the facts are associated by AND and OR connectors. The most common inference method is the fault-tree analysis [26], in which the symptoms and the events are considered as binary variables and the condition part of the rules is calculated by Boolean equations for parallel-serial connection. However, this procedure has not proven to be successful, because of the continuous nature of faults and symptoms. Therefore, approximating reasoning methods are used as an alternative. Different forward and backward chaining reasoning techniques [27] using fuzzy logic or probabilities are implemented, taking into account the effects of the rule weighting and the available heuristic knowledge, originated from the experience of operators and system engineers. Finally, a more sophisticated inference method is related to the neuro-fuzzy systems [28]. The advantage of this method is that it can fuse information from both human experts (heuristic knowledge) and experimental data (analytic knowledge), resulting in generation of new rules from data or refinement of the existing rules by adapting parameters within them.

If a theoretical process model-based method is used for detecting multiplicative (parametric) faults, the fault causalities can be determined using quantitative knowledge. Particularly, a physical-based fault symptom relationship can be calculated via the functional relationship between the physical and model parameters,  $\theta = h(p)$ , while the diagnosis-based symptom fault relationship can be determined by the inverse functional relationship  $h^{-1}$ . In addition, if the analytic symptoms are residuals, generated by a FD method based on parity equations or observers, a fault signature matrix (FSM) is constructed. The rows of the FSM correspond to the symptoms and its columns correspond to all possible additive and multiplicative faults, while its elements indicate the relationship between a symptom and the listed faults [29], [30]. A general overview of how the FDs methods are categorized according to the symptoms and fault-relevant knowledge acquisition is presented in Fig.1.6.

### 1.2 Review of MEMS Failure Modes and Detection Methods

MicroElectroMechanical Systems (MEMS) consist of electrical and mechanical components scaled down to the micrometer scale and integrated on a common substrate. Their fabrication is the outcome of a batch processing and they are allocated for functioning individually as well as in arrays. Their diminution of size has resulted in their utilization in several domains, such as medicine and biology [31], avionics [32], space [33], wireless communications [34], vehicles [35], data storage technologies [36], metrology [37], etc. It is therefore of paramount importance to maintain their reliability and functionality for a prolonged period of time.

The difficulty in ensuring proper MEMS-behavior and maintenance of their functions in routine circumstances emanates from the limited information about the microscopic failure mechanisms, which differ from the macroscopic counterparts [38].



## 1.2 Review of MEMS Failure Modes and Detection Methods

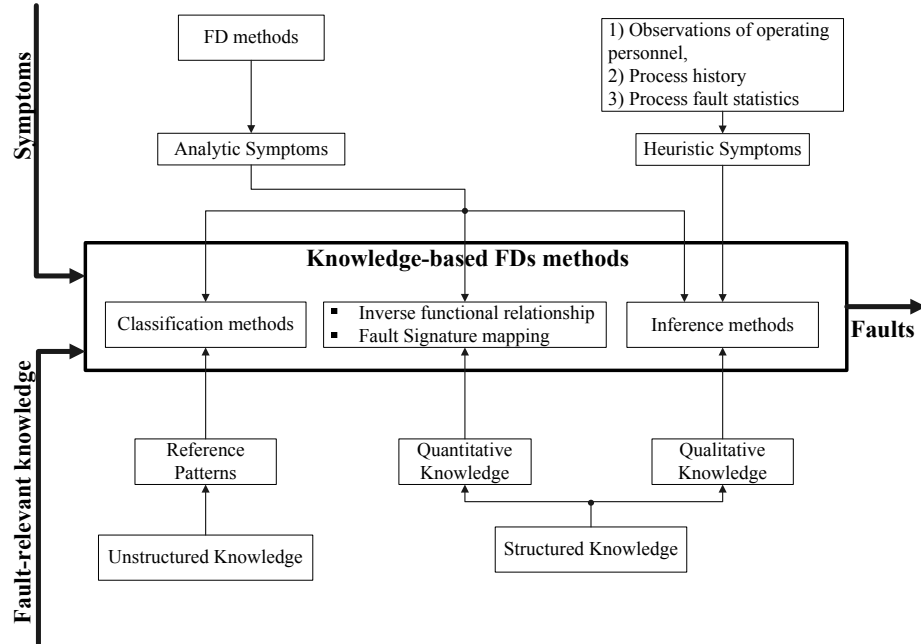


Figure 1.6: Classification of fault diagnosis methods

By failure mechanism, we mean the physical cause of an apparent system damage, called failure mode. The most common failure mechanisms and failure modes in MEMS are depicted in Table 1.2 [39].

The list of MEMS faults is usually derived via **failure analysis**, during which failure mechanisms are evaluated and failure modes are observed after elaborating characterization tests [40], [41]. After identifying and understanding the sources of the problems, different solutions are investigated for improving the fabrication process, such as studying the strength of different MEMS coating films in relation to failure mechanisms [42]. However, albeit their will to take into account all the available information on the MEMS failure modes and mechanisms at the earlier stages of manufacturing, new types of failures may be raised at later process steps and packaging. Therefore, fault modelling and simulation are proven to be necessary in the MEMS industry [43].

**Fault modelling** focuses on abstracting the behavior of physical MEMS defects to a high level representation of the device under test. Fault modelling can be accomplished using CAD tools, such as CAMEL (Contamination And Reliability Analysis of MicroElectromechanical Layout) [44], which interprets the system structural variations by finite element techniques and computes lumped parameters to represent the fault models as electric circuits [44]. The initial step of **fault simulation** involves modelling both the mechatronic and electrical elements in the same

## 1. INTRODUCTION

---

**Table 1.2:** MEMS failure mechanisms and modes

<b>Fault Modes</b>	<b>Failure Mechanisms</b>
Stiction	Capillary forces Van der Waals molecular forces Casimir forces Hydrogen bridging Electrostatic forces
Wear	Adhesion Abrasion Corrosion Friction
Fracture	Stress induced bending, shearing, torsion Shock induced Fatigue
Crystallographic defect	Point defects Dislocations Planar defects Bulk defects
Creep	Applied stress Intrinsic stress Stray stresses (thermal, residual)
Degradation of dielectrics	Leakage Charging Breakdown
Environmentally induced failure	Vibration Shock Humidity effects Radiation effects Contamination Temperature changes
Electric-related failures	Electrostatic discharge Electrical overstress Electromigration Electrical breakdown Electromagnetic pulses
Packaging reliability	Hermeticity and vacuum maintenance Thermal issues
Other failure modes	Parasitic capacitance Dampening effects Delamination

---

## 1.2 Review of MEMS Failure Modes and Detection Methods

---

simulation environment [45]. Then, fault models are injected in the fault-free MEMS description, and the simulated faulty behaviors are classified and used to form fault models at the next level of abstraction. Fault simulation is enhanced by **test generation**, which checks whether or not a fault can be detected after applying a range of input stimuli [46].

Moreover, a laboratory prototype should be tested in order to be promoted to a commercial product which is going to be used in other applications. The goal of **testing** is to validate the product functionality and verifying if the data sheet specifications are sufficed. For this reason, analogue and digital built-in self-test techniques are applied [47], [48]. However, MEMS devices should be tested many times during their life cycle, not only after manufacturing (production testing) [49]. Therefore, **model-based techniques** are developed for detecting failure modes in a general supervisory scheme. Particularly, process model-based methods relying on neural networks [50], [51], Kalman filters [52], Recursive Least Squares identification [53] and interval analysis [54] have been applied for detection of failure modes in MEMS.

### 1.3 Dissertation Objective

The main objective of this dissertation is the synthesis of **process model based FDD methods** aiming at capturing **parametric faults** that occur suddenly at multiple time instances, as shown in Fig.1.7. Due to the type of the fault to be detected, the proposed FDD methods are based on parameter estimation.

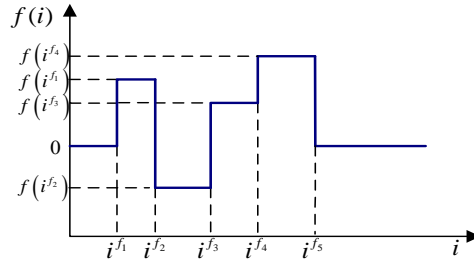


**Figure 1.7:** Time evolution of parametric fault

The parameter estimation is performed using a linearly parametrizable model, which, under the assumption of multiple abrupt parametric faults, is described as:

$$y(i) = \phi(i)^T \theta^\circ(i), \quad (1.6)$$

$$\theta^\circ(i) = \theta^\circ(i-1) + w(i) + (\Delta\theta(i) - \Delta\theta(i^{f_j})), \quad i^{f_j} < i \leq i^{f_{j+1}}, \quad (1.7)$$

$$y^m(i) = y(i) + e_y(i), \quad (1.8)$$

$$\phi_u^m(i) = \phi_u(i) + e_{\phi_u}(i), \quad (1.9)$$

where  $y^m(i) \in \mathbb{R}$ ,  $\phi^m(i) \in \mathbb{R}^n$  are the output and regression vector containing measurable signals,  $e_y(i) \in \mathbb{R}$  is measurement noise and/or model error affecting the noise-free model output  $y(i)$ ,  $e_{\phi_u}(i) \in \mathbb{R}^n$  is the measurement noise corrupting the noise-free  $u$ th component of regression vector  $\phi_u(i)$ .  $\theta^\circ(i) \in \mathbb{R}^n$  is the unknown nominal model parameter vector to be identified,  $w(i) \in \mathbb{R}^n$  is the vector modelling parameter perturbations,  $\Delta\theta(i) \in \mathbb{R}^n$  is the vector modelling abrupt parameter variations.

The parameter perturbations and noises are treated as unknown but bounded variables, with a priori known bounds. Under these assumptions, the parameter estimation is implemented in a Set Membership framework, namely **Set Membership Identification** (SMI), computing at every time instant the feasible parameter set that contains the nominal parameter vector. In addition, a data-hyperspace is generated taking into account the linearly parametrizable model, the measurement data and the a priori known noise bounds. In this research work, the SMI is encountered as an optimization problem, aiming at the recursive computation of the parametric set that outer bounds the feasible parameter set and intersects with the generated data-hyperspace. Two distinct SMI approaches are utilized, depending on the configuration

of the outer bounding parametric set: a) the orthotopic SMI, and b) the ellipsoidal SMI.

A fault is detected at the time instant that the estimated outer bounding parametric set does not intersect with the data-generated hyperspace, due to an abrupt parameter change. In order to proceed with the fault diagnosis, a resetting procedure is performed using set-theoretic operations, aiming at the determination of the new outer bounding parameter set that contains the new nominal parameter vector. During the fault isolation, consistency tests are executed, relying on the projections of the worst case parametric sets and the ones arisen from the normal operation of SMI, while the distance of their centers is used in fault identification.

The secondary objective of this dissertation is the application of the SMI-based FDD method in typical MEMS-technology examples, such as: a) a parallel-plate electrostatic microactuator, and b) a torsionally-resonant atomic force microscope (TR-AFM). The electrostatic microactuator is usually embedded in other devices for positioning or acceleration purposes in the microworld. The most common failure mechanisms of a microactuator is the particle contamination affecting the micromechanical components (mass, spring), fatigue causing the fracture of the microsprings, loss of hermeticity leading to damping changes. On the other hand, the TR-AFM is the device that is used for investigating the tribological phenomena of materials such as surface roughness, adhesion, friction etc and generating high resolutions 3D images of the samples. The most common failure mechanisms of a TR-AFM is the particle contamination of its tip affecting the tip's mass, the adhesion and friction leading to tip's wear and fatigue resulted in tip's fracture. From an engineering point of view, the failure modes of these devices are treated as parameter variations. Simulation studies are elaborated, in order to verify of the efficacy the proposed methods in detecting the failure modes of these two MEMS-technology applications.

### 1.3.1 Review of Related Literature

Several works in the literature have dealt with fault detection and diagnosis developed in a set membership framework. The set membership approach is used in the process model based FDD methods based on parity equations [55], [56], observers [57], [58], neural and neuro-fuzzy model [59], [60] to overcome the requirement of knowing the model structure or neuron, taking into consideration interval models [61]. The set membership techniques are also utilized in FDD methods based on parameter estimation. The diversification of the recorded method relies on the description of the parameter set that approximates the feasible parameter set. The different representations of the parametric set are shown in Fig. 1.8. Since these methods are related to the objective of this dissertation, a brief description of them follows in this section.

## 1. INTRODUCTION

---

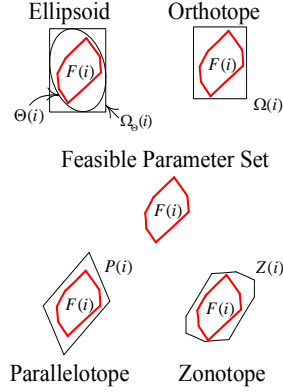


**Figure 1.8:** Different representations of the parametric sets approximating the feasible parameter set ( $n=2$ )

The common ground on these methods is the description of the linearly parametrizable model, given as

$$y^m(i) = \phi(i)^T \theta^\circ(i) + v(i) \quad (1.10)$$

$$\theta^\circ(i) = \theta^\circ(i-1) + w(i) \quad (1.11)$$

where  $v(i)$  is the equation error, corresponding to measurement noise and/or model error. The equation error and the parameter perturbation vector  $w(i)$  are assumed to be unknown but bounded with a priori known bounds. Under the assumption that

$$|v(i)| \leq v^{\max} \quad (1.12)$$

and using the linearly parametrizable model (1.10), the nominal parameter vector  $\theta^\circ(i)$  resides within a data-hyperspace, described as:

$$S(i) = \{ \theta : y^m(i) - v^{\max} \leq \phi(i)^T \theta \leq \bar{y}^m(i) + v^{\max} \}. \quad (1.13)$$

This data-hyperspace is defined by two parallel-hyperplanes and hereafter will be referred as data-hyperstrip.

In [62], the proposed fault detection strategy aims at capturing abrupt and incipient parametric faults in time-varying systems, modelled through (1.10)-(1.11) with  $v(i) \in [v^{\min}, v^{\max}]$ . The parameter perturbation  $w(i)$  is assumed to reside within an ellipsoid  $\Theta^w(0, R^w)$  ( $\Theta^w$  for brevity) and  $R^w$  is the a priori known symmetric positive definite shape matrix. Taking into account that  $\theta^\circ(i-1) \in \Theta(i-1)$ , the computation of  $\Theta(i)$  for which  $\theta^\circ(i) \in \Theta(i)$  is realized in a sequential manner using the Optimal

Volume Ellipsoid (OVE) algorithm [63], [64] as:

$$\hat{\Theta}(i) = \arg[\min_{\Theta} \{ \text{vol}(\Theta) : \theta^\circ(i) = \theta^\circ(i-1) + w(i) \in \Theta, \theta^\circ(i-1) \in \Theta(i-1), w(i) \in \Theta_w \}], \quad (1.14)$$

$$\Theta(i) = \arg \left[ \min_{\Theta} \left\{ \text{vol}(\Theta) : \Theta \supseteq \hat{\Theta}(i) \cap S(i) \right\} \right] \quad (1.15)$$

The following approaches for fault detection are proposed. The first approach addresses that a fault is said to have occurred when

$$\hat{\Theta}(i) \cap S(i) = \emptyset. \quad (1.16)$$

The second FD approach is used to monitor the system for incipient faults, according to which a fault is detected when

$$\Theta(i) \cap \Theta^\circ = \emptyset. \quad (1.17)$$

where  $\Theta^\circ$  is produced by the OVE algorithm under nominal operating conditions. If (1.17) is not valid, it is possible that the actual plant matches the nominal plant model.

In [65], the assumptions described in [62] and the fault detection procedure based on the first criterion are utilized. Moreover, two approaches for ‘recovering’ the parameters after the fault detection are presented. In the first approach, called resetting algorithm, the ellipsoid  $\hat{\Theta}(i)$  is replaced by a ‘large’ enough ellipsoid  $\Theta^{\text{reset}}$  that is guaranteed to contain the new nominal parameter vector. Then, ellipsoid  $\Theta(i) = \Theta'(i)$ , where  $\Theta'(i)$  is computed via (1.15) using  $\Theta^{\text{reset}}$  instead of  $\hat{\Theta}(i)$ . In the second approach, called projection algorithm, ellipsoid  $\hat{\Theta}(i)$  is projected onto the data-hyperstrip  $S(i)$ . Then,  $\Theta(i)$  equals to the minimum volume ellipsoid  $\Theta^p(i)$  that outer bounds the aforementioned projection. In the dissertation, it is referred that using the resetting algorithm, the new nominal parameter vector is guaranteed to be captured immediately after a fault is detected, but initially the ellipsoid may be too large to be effective for applications such as robust adaptive control. On the other hand, using the projection algorithm, there is no guarantee that the new nominal parameter vector will reside in the computed ellipsoid  $\Theta^p(i)$ , but its volume may be smaller than the volume of  $\Theta'(i)$ . Therefore, the work in this dissertation proposes an integrated approach, choosing which of the resetting or projection algorithm should be applied, intending to exploit their advantages and surpass their drawbacks.

In [66], an input-output adaptive thresholding scheme is employed using the adaptive ARMA model for detecting abrupt faults for a time-invariant system. The proposed approach relies on the prediction of the worst-case system output uncertainty bounds. The determination of the multi-step ahead system output uncertainty interval is performed using the parameter bounds, whose computation is realized in two steps. Initially, an ellipsoid  $\Theta(i)$  outer bounding the feasible parameter set is computed using the Set Membership Weighted Recursive Least Squares (SM-WRLS) [67].

## 1. INTRODUCTION

---

The next step involves the computation of the support orthotope  $\Omega^\circ(i)$  that tightly outer bounds the generated ellipsoid. The coordinates of the orthotope's vertices correspond to the parameter bounds [68]. Then, using interval arithmetic the multi-step ahead output predicted bounds  $y^-(i|i-\ell)$ ,  $y^+(i|i-\ell)$  are generated. A fault is detected when the actual output does not lie between these bounds, namely:

$$y(i) \notin [y^-(i|i-\ell), y^+(i|i-\ell)]. \quad (1.18)$$

A fault detection scheme for linear discrete systems is presented in [69]. Instead of considering (1.14),  $\theta^\circ(i)$  is assumed to remain constant over a sliding window with length  $L'$ , or  $\theta(i) = \theta(i-1) = \dots = \theta(i-L')$ . The window's minimum length  $L^*$  is assumed to be known, whereas the time instants at which the parameter vector can change (jump) are unknown. This jump-parameter system configuration is used for capturing abrupt faults. Under the assumption of a time sliding window  $[i-L+1, \dots, i]$ , an orthotope  $\Omega(i)$  that outer bounds the feasible parameter set  $F_L(i)$  is computed as:

$$\Omega(i) = \{ \theta : \theta^-(i) \preceq \theta \preceq \theta^+(i) \}, \quad (1.19)$$

$$\theta^-(i) = \left[ \min_{\theta(i) \in F_L(i)} \theta_1(i), \dots, \min_{\theta(i) \in F_L(i)} \theta_n(i) \right]^T, \quad (1.20)$$

$$\theta^+(i) = \left[ \max_{\theta(i) \in F_L(i)} \theta_1(i), \dots, \max_{\theta(i) \in F_L(i)} \theta_n(i) \right]^T, \quad (1.21)$$

$$F_L(i) = \left\{ \theta : \theta \in \bigcap_{q=i-L+1}^i S(q) \right\} \quad (1.22)$$

The bounds  $\theta^-(i)$  and  $\theta^+(i)$  can be found from the optimal solutions of linear programming problem with  $n$  variables and  $2L+2n$  constraints. In the sequel, the generated parameter bounds are used for computing of the  $\ell$ -step ahead output uncertainty predicted bounds  $y^-(i|i-\ell)$ ,  $y^+(i|i-\ell)$ . A fault is said to have occurred, when the linear programming problem gives a non feasible solution, meaning that

$$\Omega(i) = \emptyset, \text{ or, } y(i) \notin [y^-(i|i-\ell), y^+(i|i-\ell)]. \quad (1.23)$$

The possible reasons that cause the fault are due to: a) the utilization of an underestimated noise bound, b) an abrupt parameter variation (jump), c) the modification of the system's internal structure or d) the lack of persistent excitation, denoted as  $\text{rank}([\phi(i-L+1), \dots, \phi(i)]) \leq n$ . In addition, the authors highlight that there is no mutual exclusion or inclusion of the two fault detection criteria and a simple example generating four different scenarios is used to illustrate this assertion.

In [70], a robust FD strategy is proposed for capturing abrupt parametric faults relying on a parallelotope-based SMI approach. The linearly parametrizable model given in (1.10)-(1.11) is employed using  $|w(i)| \preceq \lambda$ . Also  $\theta^\circ(i)$  is assumed to be



unknown and belongs to a compact set  $E$ . Three cases are considered in terms of  $\lambda$ : a)  $\lambda = 0$ , denoting that  $\theta^\circ(i)$  does not vary within  $E$ , but it is known that it will not vary, b)  $\lambda = \bar{\lambda}$ , meaning that the parameter vector is varying, but the parameter perturbation is bounded, and c)  $\lambda = \infty$ , implying that the parameter perturbation is implicitly bounded only by the initial parameter set  $E$  and can vary at will within that set. At every time instant, it is assumed that  $\theta^\circ(i)$  resides in a parallelotope  $\mathcal{P}(i)$ , which is computed in a recursive manner as:

$$\mathcal{P}(i) = \arg_{\mathcal{P}} \left[ \min \left\{ \text{vol}(\mathcal{P}) : \mathcal{P} \supseteq \hat{\mathcal{P}}(i) \cap S(i) \right\} \right], \quad (1.24)$$

$$\hat{\mathcal{P}}(i) = \arg_{\mathcal{P}} [\mathcal{P} : \mathcal{P} \supseteq Z(i)], \text{ with} \quad (1.25)$$

$$Z(i) = \arg_Z \left\{ Z : Z = \mathcal{P}(i-1) \oplus \Omega^\lambda, \theta^\circ(i) \in Z, \theta^\circ(i-1) \in \mathcal{P}(i-1), w(i) \in \Omega^\lambda \right\} \quad (1.26)$$

$$\Omega^\lambda = \{ \theta : -\lambda \preceq \theta \preceq \lambda \} \quad (1.27)$$

where  $Z(i)$  corresponds to a zonotope which contains the sum  $\theta^\circ(i) + w(i)$  and  $\oplus$  denotes the Minkowski sum. In the time invariant case,  $\lambda = 0 \Rightarrow \hat{\mathcal{P}}(i) = \mathcal{P}(i-1)$ , while in case that  $\lambda = \infty \Rightarrow \hat{\mathcal{P}}(i) = E, \forall i$ . A fault is said to have occurred, when

$$\hat{\mathcal{P}}(i) \cap S(i) = \emptyset. \quad (1.28)$$

In order to check the intersection between the parallelotope and the data hyperstrip, the intersection between the data hyperstrip  $S(i)$  and the support hyperstrip of  $\hat{\mathcal{P}}(i)$ , defined by the hyperplanes that are tangent to  $\hat{\mathcal{P}}(i)$  and parallel to  $S(i)$  is checked. Finally, as far as concerns the fault isolation and estimation procedure, the concept of resetting the parameter set to a ‘large’ enough set that contains all faulty and non-faulty parameters, presented in [65], is adopted.

In [71], a robust FD procedure using a zonotope-based set membership consistency test for capturing sensor and parametric faults is presented. The assumptions related to the noise, parameter perturbations and the initial set presented in [70] are also used in this work. The objective of the set membership procedure is to compute at every time instant the parameter set, represented as a zonotope, that contains the nominal parameter vector  $\theta^\circ(i)$ . This is realized as:

$$Z(i) = \arg_Z \left[ \min \left\{ \text{vol}(Z) : Z \supseteq \hat{Z}(i) \cap S(i) \right\} \right], \text{ with} \quad (1.29)$$

$$\hat{Z}(i) = \arg_Z \left\{ Z : Z = Z(i-1) \oplus \Omega^\lambda, \theta^\circ(i) \in Z, \theta^\circ(i-1) \in Z(i-1), w(i) \in \Omega^\lambda \right\} \quad (1.30)$$

$$\Omega^\lambda = \{ \theta : -\lambda \preceq \theta \preceq \lambda \}. \quad (1.31)$$

It has to be mentioned that when  $\lambda = 0$ ,  $\hat{Z}(i) = Z(i-1)$  and when  $\lambda = \infty$ ,  $\hat{Z}(i) = E$ . A fault is said to have occurred, when

$$\hat{Z}(i) \cap S(i) = \emptyset. \quad (1.32)$$


---

## 1. INTRODUCTION

---

For checking the intersection between the zonotope and the data hyperstrip, the intersection between the data hyperstrip  $S(i)$  and the support hyperstrip of  $Z(i)$ , defined by the hyperplanes that are tangent to  $Z(i)$  and parallel to  $S(i)$  is checked. At the time instant of fault detection, the parameter variation is calculated using the distance between the zonotope and the data-hyperspace. In the sequel, the authors provide the minimum sensor and parametric fault magnitude. In order to reduce the conservativeness of the initial choice of  $\lambda$ , the execution of the algorithm is suggested under the assumption of time-invariant parameters and using fault-free data, during which if an inconsistency is observed, the value of the calculated parameter variation is used as a candidate value for  $\lambda$ . Finally, the maximum of all the collected candidate values is used in the fault detection procedure. This concept is also proposed for direct application in the fault detection procedure. Hence, the algorithm for the time-invariant case is applied. When an inconsistency is detected, the zonotope is expanded by the calculated parameter variation and the intersection between the expanded zonotope and the current hyperstrip is checked. If the inconsistency persists, then a fault is indicated, otherwise the algorithm continues its execution.

### 1.3.2 Contribution of the Dissertation

The main contributions of this dissertation on the development of Fault Detection and Diagnosis techniques relying on geometrical Set Membership Identification with application in MEMS are:

- the design of methods for detecting and diagnosing multiple abrupt parametric faults,
- Fault Detection and Diagnosis methods relying on Set Membership Identification,
- the combination of orthotopic and ellipsoidal Fault Detection and Diagnosis methods for the time invariant parameters case,
- the extension of the Fault Detection and Diagnosis methods to the time-varying parameter case,
- the development of a backward-in-time procedure for a more accurate specification of the time of fault occurrence and the investigation of detectability and isolability issues,
- the application of the proposed FDD methods for capturing multiple abrupt failure modes appeared in the mass, stiffness and damping coefficient of a parallel-plate electrostatic microactuator,
- the lumped parameter modelling of a torsional-resonant Atomic Force Microscope for the application of the FDD methods so as to capture abrupt fractures of the tip's radius.

### 1.3.3 Structure of the Dissertation

The dissertation is organized in five chapters.

**Chapter 1:** The first chapter provides a review of the most common FDD methods, along with their general design specifications and a brief comparison between the process-model based methods. The need for capturing failure modes in Micro-ElectroMechanical Systems (MEMS) and the related detection methods is described in the next section, followed by the the objective of dissertation and a review of the related literature.

**Chapter 2:** The second chapter deals with the Set Membership Identification (SMI) techniques for time varying systems. Two approaches are analysed according to the representation of the parameter set outer bounding the feasible parameter set: a) the orthotopic, and b) the ellipsoidal SMI. The mathematical preliminaries related to the orthotopes and the ellipsoids are provided, followed by the description of the two data hyperspace configurations, denoted as data-hyperstrips and data-hypersectors. Further on, the development of the orthotopic SMI based on linear programming techniques is presented in detail, followed by the description of the Optimal Volume Ellipsoid algorithm which is implemented taking into account data-hyperstrips and its modification in order to handle data-hypersectors. Finally, the time-invariant system case and the equation error case are presented as special cases of the previous analysis.

**Chapter 3:** The detailed description of the FDD method based on orthotopic and ellipsoidal SMI is presented in Chapter 3. Initially, the FDD assumptions are addressed. The fault detection mechanism relies on outer bounding parametric set with the data-hyperspace. The fault detection is followed by a resetting procedure, aiming at the computation of the parameter set that is guaranteed to contain the new nominal parameter vector, exploiting the information of the worst-case parameter bounds. Moreover, set theoretic operations are provided for fault isolation, while the faulty status of the parameter components is determined using the projections of the parametric set and the variation of the faulty components is estimated using the centers of the projections. Further on, the customization of the FDD procedure for time-invariant parameters is presented, while for the case of the ellipsoidal SMI, the intersection of support orthotopes and its projection is used to enhance the FDD mechanism. The last section of the third chapter deals with the fault detection and diagnosis issues associated with the detectability of the faults, the better estimation of the time instances of fault occurrence using a backward-in-time procedure and the characterization of the algorithm sensitivity according to the assumptions.

**Chapter 4:** In this chapter, the suggested FDD methods are applied in a parallel-plate micro electrostatic actuator and a torsionally resonant atomic force microscope (TR-AFM). In the former example, the microactuator system is assumed time invariant and the objective of the study is to capture multiple parametric changes in its mass, spring stiffness and damping coefficient. In the latter example, in order to obtain a linearly parametrizable model, the lumped parameter modelling taking

## 1. INTRODUCTION

---

into account the partial differential equation of the TR-AFM is presented. Then, the resultant model is regarded as time varying, the FDD methods are applied aiming at the detection of abrupt fractures of the tip's radius.

**Chapter 5:** In the fifth chapter, the dissertation results are summarized, followed by the concluding remarks. In addition, areas for further research are proposed followed by the publications of this dissertation.

**Appendix A:** Appendix A provides the auxiliary mathematical analysis related to the SMI techniques, the FDD mechanism and the TR-AFM lumped modelling.

**Appendix B:** In Appendix B, the algorithms related to ellipsoidal SMI methods and the backward-in-time fault detection are presented.

## Chapter 2

# Set Membership Identification

### 2.1 Introduction

This chapter deals with parameter estimation based on a set membership approach, namely the Set Membership Identification (SMI). The set membership approach was initiated in the domain of state estimation by Witsenhausen [72] and Schweppe [73] and was used mostly for parameter estimation in a large number of research papers up to the present [74], [75], [76], [77], [78], [79]. The objective of the SMI techniques is the determination of the feasible parameter set that contains the nominal parameter vector and is consistent with a linearly parametrizable model, the measurement data and the a priori known bounded noise-error. Due to the complexity in computing the feasible parameter set, the majority of the SMI methods aims at the determination of a more conveniently computable parametric set that outer bounds the feasible parameter set.

In this research work, the feasible parameter set is outer bounded by two distinct geometrical sets; an orthotope and an ellipsoid. Under the assumption of a linearly parametrizable model, whose output and regression vector are functions of measurable signals corrupted by bounded noise, a data-hyperspace is generated, containing the nominal parameter vector. Moreover, in the general case, the system is encountered as time-varying, due to unknown but bounded perturbations in parameter vector. The orthotopic SMI is performed using linear programming techniques [68], while the ellipsoid SMI relies on the Optimal Volume Ellipsoid (OVE) algorithm [63].

## 2. SET MEMBERSHIP IDENTIFICATION

---

### 2.2 Modeling Assumptions

Consider the linearly parametrizable model of the system under investigation:

$$y(i) = \phi(i)^T \theta^\circ(i), \quad (2.1)$$

$$\theta^\circ(i) = \theta^\circ(i-1) + w(i), \quad (2.2)$$

where  $y(i) \in \mathbb{R}$  is the noise-free model output,  $\phi(i) \in \mathbb{R}^n$  is the noise-free regression vector,  $\theta^\circ(i) \in \mathbb{R}^n$  is the unknown nominal parameter vector to be identified,  $w(i) \in \mathbb{R}^n$  is the parameter perturbation vector. The model output  $y(i)$  and the components of the regression vector  $\phi(i) = [\phi_1(i), \dots, \phi_n(i)]^T$  are functions of measurable signals.

The observed model output is described as

$$y^m(i) = y(i) + e_y(i), \quad (2.3)$$

where  $e_y(i) \in \mathbb{R}$  is the output noise, modelling measurement noise and/or model error. Similarly, the observed  $u$ th component of regression vector is described as:

$$\phi_u^m(i) = \phi_u(i) + e_{\phi_u}(i), \quad (2.4)$$

with  $e_{\phi_u}(i) \in \mathbb{R}$ ,  $u = 1, \dots, n$ . The noise terms  $e_y(i)$  and  $e_{\phi_u}(i)$  are assumed unknown but bounded at every instant  $i$

$$\mu_y(i) |e_y(i)|^2 \leq 1 \quad (2.5)$$

$$\mu_{\phi_u}(i) |e_{\phi_u}(i)|^2 \leq 1, \quad (2.6)$$

with  $\mu_y(i)$ ,  $\mu_{\phi_u}(i) \in \mathbb{R}_+^*$ . Rather than necessitating the knowledge of the bounds at every time instant, without loss of generality, the worst-case bound  $e_{y(\phi_u)}^{\max} = \max_i \left( \frac{1}{\sqrt{\mu_{y(\phi_u)}(i)}} \right)$  and the worst-case bounds of the noise,

$$|e_y(i)| \leq e_y^{\max}, \quad (2.7)$$

$$|e_{\phi_u}(i)| \leq e_{\phi_u}^{\max}. \quad (2.8)$$

are assumed to be known.

The vector  $w(i)$  represents the changes in parameter vector at every time instant, whose components are assumed to be unknown but bounded:

$$w_u(i) \in [w_u^{\min}, w_u^{\max}], \quad \forall i, \quad u = 1, \dots, n \quad (2.9)$$

where  $w_u^{\min}$ ,  $w_u^{\max}$  are the a priori known worst case parameter perturbation bounds.

The goal of Set Membership Identification (SMI) is to determine at every time instant the feasible parameter set  $F(i)$  within which the nominal parameter vector  $\theta^\circ(i)$  resides and is consistent with the linearly parametrizable model described via (2.1) and (2.2), the measurement data given in (2.3) and (2.4), the bounded noise-terms

given by (2.7) and (2.8) and the bounded parameter perturbations described by (2.9). Due to the difficulty in computing the feasible parameter set, ellipsoids and orthotopes will be used to outer bound it. These geometrical sets were selected because of their simplified mathematical expressions presented in the sequel and due to their computational efficiency.

## 2.3 Ellipsoid and Orthotope Preliminaries

### 2.3.1 Orthotope

The orthotope is the parallelotope oriented parallel to the parametric axes, as shown in Fig. 2.1, and is defined as:

$$\Omega(i) = \left\{ \theta : \begin{bmatrix} \theta_{\Omega_1}^-(i) \\ \vdots \\ \theta_{\Omega_n}^-(i) \end{bmatrix} \preceq \theta \preceq \begin{bmatrix} \theta_{\Omega_1}^+(i) \\ \vdots \\ \theta_{\Omega_n}^+(i) \end{bmatrix} \right\}. \quad (2.10)$$

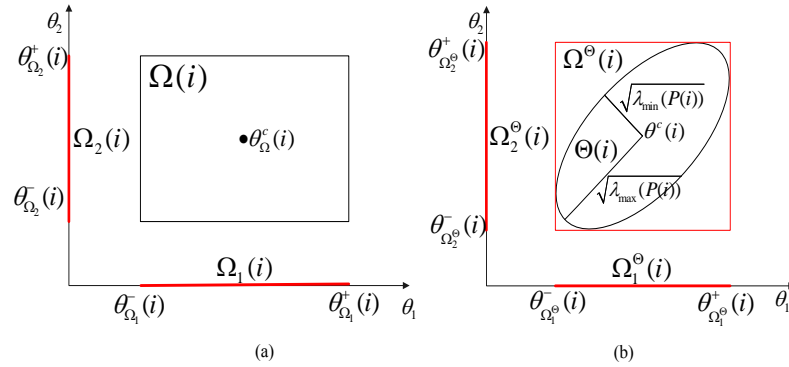


**Figure 2.1:** Outer bounding parametric sets ( $n=2$ ): a) orthotope, b) ellipsoid and support orthotope

The projection of the orthotope on the  $u$ th axis is defined as:

$$\Omega_u(i) = \text{proj}_u(\Omega(i)) = \left\{ \theta_u : \theta_u \in \left[ \theta_{\Omega_u}^-(i), \theta_{\Omega_u}^+(i) \right] \right\}, \forall u \in \{1, \dots, n\}, \quad (2.11)$$

where  $\text{proj}_u(X)$  denotes the projection of a parametric set  $X$  on the  $u$ th axis and its center is computed as:

$$\theta_{\Omega_u}^c(i) = \frac{\theta_{\Omega_u}^+(i) + \theta_{\Omega_u}^-(i)}{2}, \quad u = 1, \dots, n. \quad (2.12)$$

## 2. SET MEMBERSHIP IDENTIFICATION

---

Consequently, the centroid of  $\Omega(i)$  is given as:

$$\theta_{\Omega}^c(i) = [\theta_{\Omega_1}^c(i), \dots, \theta_{\Omega_n}^c(i)]^T. \quad (2.13)$$

### 2.3.2 Ellipsoid and Support Orthotope

The ellipsoid is defined as:

$$\Theta(i) = \left\{ \theta : (\theta - \theta^c(i))^T P(i)^{-1} (\theta - \theta^c(i)) \leq 1 \right\}, \quad (2.14)$$

where  $\theta^c(i)$  is its centroid and  $P(i) \succ 0$  is the symmetric shape matrix. The shape matrix denotes how far the ellipsoid extends from its centroid, as presented in Fig. 2.1b. In addition, the lengths of the semi-axes of the ellipsoid are equal to the square root of the eigenvalues of the shape matrix, while the principal axes of the ellipsoid have the same direction with the eigenvectors of the shape matrix. Alternatively, the ellipsoid can be computed in terms of its support function  $\rho(q|\Theta(i))$  as:

$$\Theta(i) = \{ \theta : \langle q, \theta \rangle \leq \rho(q|\Theta(i)) \}, \quad \forall q \in \mathbb{R}^n, \quad (2.15)$$

while the support function is computed as [80]:

$$\rho(q|\Theta(i)) = \sup_{\theta \in \Theta(i)} \langle q, \theta \rangle = \langle q, \theta^c(i) \rangle + \langle q, P(i)q \rangle^{1/2}, \quad q \in \mathbb{R}^n, \quad (2.16)$$

where  $\langle \cdot \rangle$  denotes the inner product function. Inequality (2.15) means that an ellipsoid is the hyperspace between an infinity number of support hyperplanes defined as:

$$h(i) = \{ \theta : \langle q, \theta \rangle = \rho(q|\Theta(i)) \}. \quad (2.17)$$

The parameter bounds correspond to the coordinates of vertices of the support orthotope of the ellipsoid,  $\Omega^{\Theta}(i)$ .  $\Omega^{\Theta}(i)$  is the convex polytope defined by the intersection of the support hyperplanes of the ellipsoid, which are parallel to the parametric axes:

$$\Omega^{\Theta}(i) = \left\{ \theta : \bigcap_{u=1}^{2n} \langle q_u^o, \theta \rangle \leq \rho(q_u^o|\Theta(i)) \right\}, \quad (2.18)$$

where

$$q_u^o = [0, \dots, 0, 1, 0, \dots, 0]^T, \quad q_{u+n}^o = -q_u^o \quad (2.19)$$

with the location of one at the  $u$ th position,  $u = 1, \dots, n$ . Hence, the parameter bounds are computed as:

$$\theta_{\Omega_u^{\Theta}}^+(i) = \rho(q_u^o|\Theta(i)), \quad (2.20)$$

$$\theta_{\Omega_u^{\Theta}}^-(i) = -\rho(q_{u+n}^o|\Theta(i)). \quad (2.21)$$



Moreover,  $\theta_{\Omega_u^\ominus}^-(i)$ ,  $\theta_{\Omega_u^\ominus}^+(i)$  are the minimum and maximum values of the projection of  $\Omega^\ominus(i)$  on the  $u$ th parameter axis, which is equivalent to the projection of  $\Theta(i)$  on the  $u$ th parameter axis, defined as:

$$\Omega_u^\ominus(i) = \underset{u}{\text{proj}}(\Omega^\ominus(i)) = \underset{u}{\text{proj}}(\Theta(i)) = \left\{ \theta_u : \theta_u \in \left[ \theta_{\Omega_u^\ominus}^-(i), \theta_{\Omega_u^\ominus}^+(i) \right] \right\}, \forall u \in \{1, \dots, n\} \quad (2.22)$$

## 2.4 Data-Generated Hyperspace

At every time instant, the nominal parameter vector  $\theta^\circ(i)$  resides in an unbounded, convex hyperspace  $S(i)$ ,

$$\theta^\circ(i) \in S(i) \quad (2.23)$$

which is compatible with the linearly parametrizable model described in (2.1) and (2.2), the measurement data given in (2.3) and (2.4) and the noise bounds (2.7) and (2.8). There are two configurations of the data hyperspace; the data-hyperstrip  $S^p(i)$  and the data-hypersector  $S^{mp}$  [81], [64], [82], [83].

### 2.4.1 Data-hyperstrip

Inducing (2.3) and (2.4) into (2.1) yields in:

$$\begin{aligned} y^m(i) &= [\phi_1^m(i), \dots, \phi_n^m(i)] \theta^\circ(i) + (e_y(i) - [e_{\phi_1}(i), \dots, e_{\phi_n}(i)] \theta^\circ(i)) \\ &= \phi^m(i)^T \theta^\circ(i) + \tilde{e}(i). \end{aligned} \quad (2.24)$$

Since the nominal parameter vector is unknown, the computation of the bounds of  $\tilde{e}(i)$  relies on the fact that  $\theta^\circ(i)$  resides within an estimated parametric set  $\mathcal{Z}(i)$ . Therefore, the values of  $\theta_1^\circ(i), \dots, \theta_n^\circ(i)$  are replaced by the estimated upper and lower parameter bounds  $\theta_{\mathcal{Z}_u}^-(i), \theta_{\mathcal{Z}_u}^+(i)$ , where  $\mathcal{Z}_u(i)$  denotes the projection of  $\mathcal{Z}(i)$  on the  $u$ th axis, and the noise  $\tilde{e}(i)$  is described as:

$$\begin{aligned} \tilde{e}(i) \in [\tilde{e}^{\min}(i), \tilde{e}^{\max}(i)] &= [-e_y^{\max}, e_y^{\max}] + [-e_{\phi_1}^{\max}, e_{\phi_1}^{\max}] \times [\theta_{\mathcal{Z}_1}^-(i), \theta_{\mathcal{Z}_1}^+(i)] + \dots + \\ & \quad [-e_{\phi_n}^{\max}, e_{\phi_n}^{\max}] \times [\theta_{\mathcal{Z}_n}^-(i), \theta_{\mathcal{Z}_n}^+(i)]. \end{aligned} \quad (2.25)$$

According to interval arithmetic, since the noise terms  $e_y(i), e_{\phi_1}(i), \dots, e_{\phi_n}(i)$  are distributed symmetrically around zero, then

$$|e_y(i)| \leq \tilde{e}^{\max}(i), \text{ with} \quad (2.26)$$

$$\tilde{e}^{\max}(i) = e_y^{\max} + \sum_{u=1}^n e_{\phi_u}^{\max} \max \left( \left| \theta_{\mathcal{Z}_u}^-(i) \right|, \left| \theta_{\mathcal{Z}_u}^+(i) \right| \right). \quad (2.27)$$

## 2. SET MEMBERSHIP IDENTIFICATION

---

Using (2.24) in (2.26) implies that

$$\theta^\circ(i) \in S^p(i), \text{ with} \quad (2.28)$$

$$S^p(i) = \{\theta : y^m(i) - \tilde{e}^{\max}(i) \leq \phi^m(i)^T \theta \leq y^m(i) + \tilde{e}^{\max}(i)\}. \quad (2.29)$$

$S^p(i)$  is called data-hyperstrip and corresponds to a hyperspace between two **parallel hyperplanes** (Fig. 2.2),

$$S_1^p(i) = \{\theta : \phi^m(i)^T \theta = y^m(i) - \tilde{e}^{\max}(i)\}, \quad (2.30)$$

$$S_2^p(i) = \{\theta : \phi^m(i)^T \theta = y^m(i) + \tilde{e}^{\max}(i)\}. \quad (2.31)$$

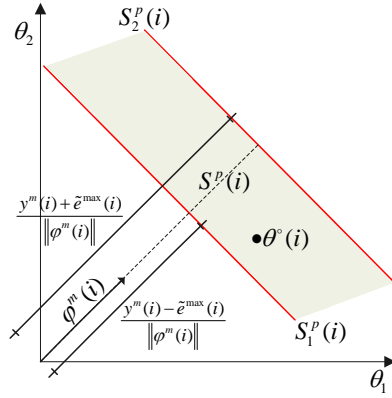


Figure 2.2: Graphical representation of data-hyperstrip (n=2)

### 2.4.2 Data-hypersector

An alternative configuration of the data-hyperspace without using the estimated parameter bounds can be accomplished under the a priori knowledge of the sign of  $\theta_u^\circ(i)$ ,  $\forall i, u = 1, \dots, n$ .

Introducing (2.1) into (2.3), and then into (2.7) yields:

$$y^m(i) - e_y^{\max} \leq \phi(i)^T \theta^\circ(i) \leq y^m(i) + e_y^{\max} \quad (2.32)$$

and combining (2.4) with (2.8) results in:

$$\phi_u^m(i) - e_{\phi_u}^{\max} \leq \phi_u(i) \leq \phi_u^m(i) + e_{\phi_u}^{\max}, \quad u = 1, \dots, n. \quad (2.33)$$

If  $\theta_u^\circ(i) > 0$ , then

$$(\phi_u^m(i) - e_{\phi_u}^{\max}) \theta_u^\circ(i) \leq \phi_u(i) \theta_u^\circ(i) \leq (\phi_u^m(i) + e_{\phi_u}^{\max}) \theta_u^\circ(i), \quad (2.34)$$

or, if  $\theta_u^\circ(i) < 0$ ,

$$(\phi_u^m(i) + e_{\phi_u}^{\max}) \theta_u^\circ(i) \leq \phi_u(i) \theta_u^\circ(i) \leq (\phi_u^m(i) - e_{\phi_u}^{\max}) \theta_u^\circ(i), \quad (2.35)$$

implying that:

$$\left( \phi_u^m(i) - \text{sgn}(\theta_u^\circ(i)) e_{\phi_u}^{\max} \right) \theta_u^\circ(i) \leq \phi_u(i) \theta_u^\circ(i) \leq \left( \phi_u^m(i) + \text{sgn}(\theta_u^\circ(i)) e_{\phi_u}^{\max} \right) \theta_u^\circ(i). \quad (2.36)$$

The summation of these terms yields:

$$\sum_{u=1}^n \left( \phi_u^m(i) - \text{sgn}(\theta_u^\circ(i)) e_{\phi_u}^{\max} \right) \theta_u^\circ(i) \leq \phi(i)^T \theta^\circ(i) \leq \sum_{u=1}^n \left( \phi_u^m(i) + \text{sgn}(\theta_u^\circ(i)) e_{\phi_u}^{\max} \right) \theta_u^\circ(i) \quad (2.37)$$

At every time instant, both inequalities (2.32) and (2.37) are valid, leading to:

$$\sum_{i=1}^n (\phi_u^m(i) - \text{sgn}(\theta_u^\circ) e_{\phi_u}^{\max}) \theta_u^\circ(i) \leq y^m(i) + e_y^{\max}, \quad (2.38)$$

$$\sum_{i=1}^n (\phi_u^m(i) + \text{sgn}(\theta_u^\circ) e_{\phi_u}^{\max}) \theta_u^\circ(i) \geq y^m(i) - e_y^{\max}. \quad (2.39)$$

Inequalities (2.38) and (2.39) imply that

$$\theta^\circ(i) \in S^{np}(i), \text{ with} \quad (2.40)$$

$$S^{np}(i) = \left\{ \theta : y^m(i) - e_y^{\max} \leq \phi^A(i)^T \theta, \phi^B(i)^T \theta \leq y^m(i) + e_y^{\max} \right\}, \quad (2.41)$$

with

$$\phi^A(i) = \begin{bmatrix} \phi_1^m(i) + \text{sgn}(\theta_1^\circ) e_{\phi_1}^{\max} \\ \vdots \\ \phi_n^m(i) + \text{sgn}(\theta_n^\circ) e_{\phi_n}^{\max} \end{bmatrix}, \quad (2.42)$$

$$\phi^B(i) = \begin{bmatrix} \phi_1^m(i) - \text{sgn}(\theta_1^\circ) e_{\phi_1}^{\max} \\ \vdots \\ \phi_n^m(i) - \text{sgn}(\theta_n^\circ) e_{\phi_n}^{\max} \end{bmatrix}. \quad (2.43)$$

$S^{np}$  is called data-hypersector and corresponds to the hyperspace between two **non-parallel hyperplanes** (Fig. 2.3),

$$S_1^{np}(i) = \{ \theta : \phi^A(i)^T \theta = y^m(i) - e_y^{\max} \}, \quad (2.44)$$

$$S_2^{np}(i) = \{ \theta : \phi^B(i)^T \theta = y^m(i) + e_y^{\max} \}. \quad (2.45)$$

## 2. SET MEMBERSHIP IDENTIFICATION

---

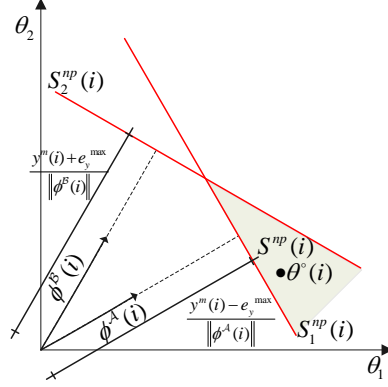


Figure 2.3: Graphical representation of the data-hypersector ( $n=2$ )

### 2.5 Set Membership Identification

The SMI procedure is encountered as an optimization problem aiming at the recursive computation of the ellipsoid or the orthotope that contains the nominal parameter vector at every time instant,

$$\theta^\circ(i) \in \Omega(i), \forall i \quad (2.46)$$

or

$$\theta^\circ(i) \in \Theta(i), \forall i. \quad (2.47)$$

given that  $\theta^\circ(i) \in S(i)$ .

#### 2.5.1 Orthotope-based Set Membership Identification

The condition (2.46) implies that  $\theta^\circ(i-1) \in \Omega(i-1)$ , while (2.9) implies that  $w(i) \in \Omega^w$ ,  $\forall i$ , with  $\Omega^w$  called perturbation orthotope and defined as:

$$\Omega^w = \left\{ \theta : \begin{bmatrix} w_1^{\min} \\ \vdots \\ w_n^{\min} \end{bmatrix} \preceq \theta \preceq \begin{bmatrix} w_1^{\max} \\ \vdots \\ w_n^{\max} \end{bmatrix} \right\}. \quad (2.48)$$

Given (2.2), the nominal parameter vector  $\theta^\circ(i)$  resides in the augmented orthotope  $\hat{\Omega}(i)$ , computed as:

$$\hat{\Omega}(i) = \arg \{ \Omega : \Omega = \Omega(i-1) \oplus \Omega^w \} \quad (2.49)$$

where  $\oplus$  denotes the Minkowski sum and

$$\hat{\Omega}(i) = \left\{ \theta : \begin{bmatrix} \hat{\theta}_{\Omega_1}^-(i) \\ \vdots \\ \hat{\theta}_{\Omega_n}^-(i) \end{bmatrix} \preceq \theta \preceq \begin{bmatrix} \hat{\theta}_{\Omega_1}^+(i) \\ \vdots \\ \hat{\theta}_{\Omega_n}^+(i) \end{bmatrix} \right\}, \quad (2.50)$$

with

$$(2.51)$$

$$\hat{\theta}_{\Omega_u}^-(i) = \theta_{\Omega_u}^-(i-1) + w_u^{\min}, \quad (2.52)$$

$$\hat{\theta}_{\Omega_u}^+(i) = \theta_{\Omega_u}^+(i-1) + w_u^{\max}. \quad (2.53)$$

Then, the orthotope  $\Omega(i)$  is computed in a recursive manner solving the optimization problem:

$$\Omega(i) = \arg \left\{ \Omega : \Omega \supseteq \left( \hat{\Omega}(i) \cap S(i) \right) \right\}, \quad (2.54)$$

$$\theta_u^-(i) = \min \left\{ \theta_u : \theta_u \in \text{proj}_u(\Omega(i)) \right\}, \quad (2.55)$$

$$\theta_u^+(i) = \max \left\{ \theta_u : \theta_u \in \text{proj}_u(\Omega(i)) \right\}. \quad (2.56)$$

If  $S(i) = S^p(i)$ , then it is defined through (2.29) with:

$$\tilde{e}^{\max}(i) = e_y^{\max} + \sum_{u=1}^n e_{\phi_u}^{\max} \max \left( \left| \hat{\theta}_{\Omega_u}^-(i) \right|, \left| \hat{\theta}_{\Omega_u}^+(i) \right| \right), \quad (2.57)$$

The problem stated in (2.54)-(2.56) can be expressed in a standard optimization form and can be solved via linear programming techniques. In particular, the parameter bounds  $\theta_{\Omega_u}^-(i)$  and  $\theta_{\Omega_u}^+(i)$  are the optimal solutions of the  $2n$  linear programming problem with  $2(n+1)$  constraints:

$$\theta_{\Omega_u}^-(i) = \min_{\theta} f_u^T \theta, \quad (2.58)$$

$$\theta_{\Omega_u}^+(i) = -\min_{\theta} f_{u+n}^T \theta, \quad u = 1, \dots, n \quad (2.59)$$

subject to

$$\mathcal{A}(i)\theta \leq b(i), \quad (2.60)$$

$$\hat{\theta}_{\Omega_u}^-(i) \leq \theta \leq \hat{\theta}_{\Omega_u}^+(i), \quad \forall u \in \{1, \dots, n\} \quad (2.61)$$

where  $f_u$  is the  $u$ th column of the matrix  $f = [I_{n \times n}, -I_{n \times n}]$ ,  $I$  is the  $n \times n$  identity matrix and

- $\mathcal{A}(i) = [-\phi^m(i), \phi^m(i)]^T$  and  $b(i) = [-y^m(i) + \tilde{e}^{\max}(i), y^m(i) + \tilde{e}^{\max}(i)]^T$ , if  $S(i) = S^p(i)$ ,

## 2. SET MEMBERSHIP IDENTIFICATION

- $\mathcal{A}(i) = [-\phi^A(i), \phi^B(i)]^T$  and  $b(i) = [-y^m(i) + e_y^{\max}, y^m(i) + e_y^{\max}]^T$ , if  $S(i) = S^{np}(i)$

It has to be mentioned that  $\Omega(i) \subseteq \hat{\Omega}(i)$  and consequently:

$$\hat{\theta}_{\Omega_u}^-(i) \leq \theta_{\Omega_u}^-(i), \quad (2.62)$$

$$\theta_{\Omega_u}^+(i) \leq \hat{\theta}_{\Omega_u}^+(i). \quad (2.63)$$

An example of the computation of  $\Omega(i)$  using either the hyperspace either  $S^p$  or  $S^{np}$  is presented in Fig.(2.4).

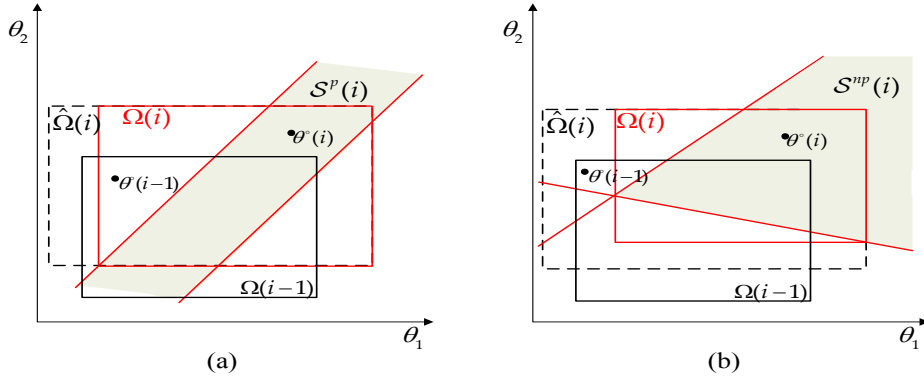


**Figure 2.4:** Graphical representation of the computation of  $\Omega(i)$  using: a) data-hyperstrips and b) data-hypersectors ( $n=2$ )

### 2.5.2 Ellipsoid-based Set Membership Identification

The condition (2.47) implies that  $\theta^{(i-1)} \in \Theta(\theta^c(i-1), P(i-1)) = \Theta(i-1)$ . Taking into account that the parameter perturbation vector resides in  $\Omega^w$  defined by (2.48),  $w(i) \in \Theta^w(w^c, P^w)$ ,  $\forall i$ , where  $\Theta^w(w^c, P^w) \supset \Omega^w$ .  $\Theta^w$  is called the perturbation ellipsoid and its computation is provided in Appendix A.1. Given (2.2), the nominal parameter vector  $\theta^{(i)}$  resides in the ellipsoid  $\hat{\Theta}(\hat{\theta}(i), \hat{P}(i))$ , called the augmented ellipsoid hereafter, defined as [84], [85]:

$$\hat{\Theta}(i) = \arg \min_{\Theta} \{ \text{vol}(\Theta) : \theta(i-1) + w(i) \in \Theta, \theta(i-1) \in \Theta(i-1), w(i) \in \Theta^w \}. \quad (2.64)$$

The centroid and the shape matrix of  $\hat{\Theta}(i)$  are computed as:

$$\hat{\theta}^c(i) = \theta^c(i-1) + w^c, \quad (2.65)$$

$$\hat{P}(i) = (\zeta + 1)P(i-1) + \left( \frac{1}{\zeta} + 1 \right) P^w. \quad (2.66)$$

The variable  $\zeta$  is the unique positive solution of  $\sum_{u=1}^n \frac{1}{\lambda_u + \zeta} = \frac{n}{\zeta(\zeta+1)}$  and  $\lambda_u$  are the solutions of the generalized eigenvalue problem  $P^w \chi_u = \lambda_u P(i-1) \chi_u$ .

The computation of  $\Theta(i)$  in recursive form is equivalent to the mathematical solution of the optimization problem, described as:

$$\Theta(i) = \arg \left[ \min_{\Theta} \left\{ \text{vol}(\Theta) : \Theta \supseteq \left[ \hat{\Theta}(i) \cap S(i) \right] \right\} \right]. \quad (2.67)$$

### 2.5.2.1 Ellipsoid-SMI using data-hyperstrips

If the ellipsoid-SMI is performed using data-hyperstrips, then  $S(i) = S^p(i)$  computed via (2.29) with:

$$\tilde{e}^{\max}(i) = e_y^{\max} + \sum_{u=1}^n e_{\phi_u}^{\max} \max \left( \left| \hat{\theta}_{\Omega_u^{\ominus}}^{-}(i) \right|, \left| \hat{\theta}_{\Omega_u^{\ominus}}^{+}(i) \right| \right), \quad (2.68)$$

where

$$\hat{\theta}_{\Omega_u^{\ominus}}^{+}(i) = \rho \left( q_u^{\circ} \mid \hat{\Theta}(i) \right), \quad (2.69)$$

$$\hat{\theta}_{\Omega_u^{\ominus}}^{-}(i) = -\rho \left( q_{u+n}^{\circ} \mid \hat{\Theta}(i) \right), \quad (2.70)$$

with  $q_u^{\circ}$ ,  $q_{u+n}^{\circ}$  given in (2.19).

The recursive computation of  $\Theta(i)$  based on (2.67) can be realized using the Optimal Volume Ellipsoid (OVE) algorithm. The main concept of its design is described in details in [63] and is presented in algorithmic form in [64]. It should be mentioned that the first step of the OVE algorithm checks if the intersection between the ellipsoid  $\hat{\Theta}(i)$  and the data-hyperspace  $S^p(i)$  is non-empty. This consistency check relies on the distance between the hyperplanes  $S_1^p(i)$ ,  $S_2^p(i)$  and the support hyperplanes of  $\hat{\Theta}(i)$  [86], parallel to  $S_1^p(i)$ ,  $S_2^p(i)$ , as presented in Fig. 2.5. Particularly, the support hyperplanes of  $\hat{\Theta}(i)$  are calculated as:

$$h_1(i) = \left\{ \theta : \phi^m(i)^T \theta = -\rho \left( -\phi^m(i), \hat{\Theta}(i) \right) \right\}, \quad (2.71)$$

$$h_2(i) = \left\{ \theta : \phi^m(i)^T \theta = \rho \left( \phi^m(i), \hat{\Theta}(i) \right) \right\}. \quad (2.72)$$

Therefore, if

$$y^m(i) + \tilde{e}^{\max}(i) \leq \phi^m(i)^T \hat{\theta}^c(i) - \sqrt{\phi^m(i)^T \hat{P}(i) \phi^m(i)} \quad \text{or} \quad (2.73)$$

$$y^m(i) - \tilde{e}^{\max}(i) \geq \phi^m(i)^T \hat{\theta}^c(i) + \sqrt{\phi^m(i)^T \hat{P}(i) \phi^m(i)} \quad (2.74)$$

then  $\hat{\Theta}(i) \cap S^p(i) = \emptyset$ .

When  $\hat{\Theta}(i) \cap S^p(i) \neq \emptyset$ , rather than computing directly  $\Theta(i)$  through (2.67), the ellipsoid  $\tilde{\Theta}(i)$  is computed as the solution of the reformulated optimization problem:

$$\tilde{\Theta}(i) = \arg \left[ \min_{\Theta} \left\{ \text{vol}(\Theta) : \Theta \supseteq [\mathcal{E} \cap \tilde{S}(i)] \right\} \right] \quad (2.75)$$

## 2. SET MEMBERSHIP IDENTIFICATION

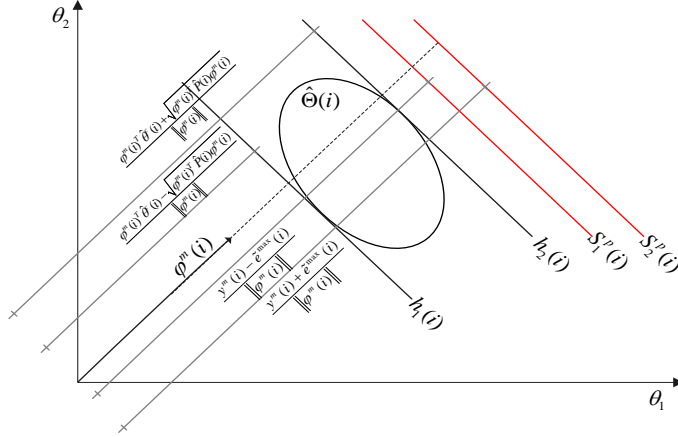


**Figure 2.5:** Graphical representation of the data-hyperstrip and the support hyperplanes of ellipsoid ( $n=2$ )

where: a)  $\mathcal{E} = \{\tilde{\theta} : \tilde{\theta}^T \tilde{\theta} \leq 1\}$  is the unit radius hypersphere, arisen from the affine transformation of  $\hat{\Theta}(i)$  using  $\theta = \hat{\theta}^c(i) + J\tilde{\theta}$ ,  $\hat{P}(i) = JJ^T$ , b)  $\tilde{S}(i)$  is the transformed hyperstrip  $\tilde{S}(i) = \left\{ \tilde{\theta} : \left| y^m(i) - \phi^m(i)^T \hat{\theta}^c(i) / \|\tilde{\phi}(i)\| - \tilde{\phi}(i)^T \tilde{\theta} / \|\tilde{\phi}(i)\| \right| \leq \varepsilon^{\max}(i) / \|\tilde{\phi}(i)\| \right\}$  using the transformed regression vector  $\tilde{\phi}(i)^T = \phi(i)^T J$ . The centroid and the shape matrix of  $\tilde{\Theta}(i)$  are defined as  $\tilde{\theta}^c(i) = \tau(i) \frac{\tilde{\phi}(i)}{\|\tilde{\phi}(i)\|}$  and  $\tilde{P}(i) = \delta(i)I + (\sigma(i) - \delta(i)) \frac{\tilde{\phi}(i)\tilde{\phi}(i)^T}{\|\tilde{\phi}(i)\|^2}$ , respectively. It has to be mentioned that the centroid  $\tilde{\theta}^c(i)$  lies along the transformed regression vector and its length equals to  $\tau(i)$ ,  $\delta(i) > 0$  equals to the squared length of semi-axis of  $\tilde{\Theta}(i)$  perpendicular to  $\tilde{\phi}(i)$ ,  $\sigma(i) > 0$  equals to the squared length of semi-axis of  $\tilde{\Theta}(i)$  along  $\tilde{\phi}(i)$ ,  $I$  is the identity  $n \times n$  matrix and  $P(i) = J\tilde{P}(i)J^T$ .

Following the previous operations, the centroid and shape matrix of ellipsoid  $\Theta(i)$  can be computed as:

$$\theta^c(i) = \hat{\theta}^c(i) + \frac{\tau(i)\hat{P}(i)\phi^m(i)}{\sqrt{\phi^m(i)^T \hat{P}(i)\phi^m(i)}}, \quad (2.76)$$

$$P(i) = \delta(i)\hat{P}(i) + [\sigma(i) - \delta(i)] \frac{\hat{P}(i)\phi^m(i)\phi^m(i)^T \hat{P}(i)}{\phi^m(i)^T \hat{P}(i)\phi^m(i)}. \quad (2.77)$$

The graphical representation of the computation of  $\Theta(i) \supset \hat{\Theta}(i) \cap S(i)$  is depicted in Fig. 2.6. The computation of the ellipsoid based on data-hyperstrips (OVE algorithm) is given in Appendix B.1.



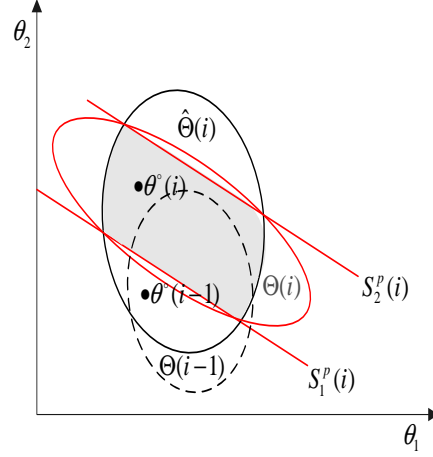


**Figure 2.6:** Graphical representation of the computation of  $\Theta(i)$  using a data-hyperstrip ( $n=2$ )

### 2.5.2.2 Ellipsoid-SMI using data-hypersectors

The ellipsoid-SMI procedure handling data-hypersectors can be performed, customizing the OVE algorithm. At first, the intersection of the data hypersector  $S_1^{np}(i)$  with the ellipsoid  $\hat{\Theta}(i)$  is investigated, based on the support hyperplanes of the ellipsoid. Particularly, it is checked if  $S_1^{np}(i) \in [h_{11}(i), h_{12}(i)]$  with

$$h_{11}(i) = \left\{ \theta : \phi^A(i)^T \theta = -\rho \left( -\phi^A(i), \hat{\Theta}(i) \right) \right\}, \quad (2.78)$$

$$h_{12}(i) = \left\{ \theta : \phi^A(i)^T \theta = \rho \left( \phi^A(i), \hat{\Theta}(i) \right) \right\}, \quad (2.79)$$

and  $S_2^{np}(i) \in [h_{21}(i), h_{22}(i)]$  with

$$h_{21}(i) = \left\{ \theta : \phi^B(i)^T \theta = -\rho \left( -\phi^B(i), \hat{\Theta}(i) \right) \right\}, \quad (2.80)$$

$$h_{22}(i) = \left\{ \theta : \phi^B(i)^T \theta = \rho \left( \phi^B(i), \hat{\Theta}(i) \right) \right\}. \quad (2.81)$$

When both  $S_1^{np}(i)$  and  $S_2^{np}(i)$  intersect with  $\hat{\Theta}(i)$  as shown in Fig. 2.7a, the computation of  $\Theta(i)$  is performed in two steps; initially, an ellipsoid  $\Theta'(i)$  is computed via the OVE algorithm as:

$$\Theta'(i) = \arg \left[ \min_{\Theta} \left\{ \text{vol}(\Theta) : \Theta \supset \hat{\Theta}(i) \cap [S_1^{np}(i), h_{12}(i)] \right\} \right], \quad (2.82)$$

as shown in Fig. (2.7b).

## 2. SET MEMBERSHIP IDENTIFICATION

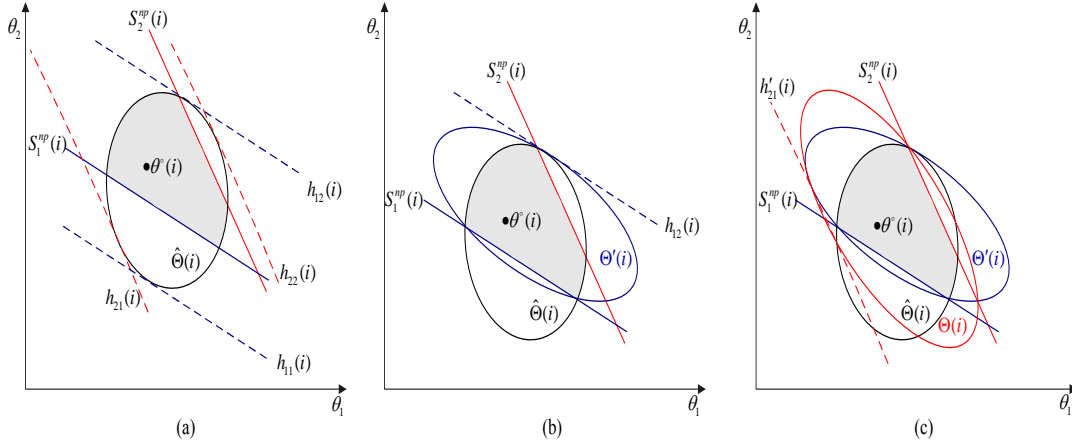


**Figure 2.7:** Graphical representation of the computation of  $\Theta(i)$  using data-hypersectors ( $n=2$ )

Then, the OVE algorithm is applied again, checking the intersection of  $\Theta'(i)$  with  $S_2^{np}(i)$ . If  $\Theta'(i) \cap S_2^{np}(i) \neq \emptyset$  (Fig. 2.7c), then

$$\Theta(i) = \arg \left[ \min \left\{ \text{vol}(\Theta) : \Theta \supset \bigcap [h'_{21}(i), S_2^{np}(i)] \right\} \right], \quad (2.83)$$

$$h'_{21}(i) = \left\{ \theta : \phi^{\mathcal{B}}(i)^T \theta = -\rho \left( -\phi^{\mathcal{B}}(i), \Theta'(i) \right) \right\}. \quad (2.84)$$

If  $\Theta'(i) \cap S_2^{np}(i) = \emptyset$ , it implies that:

$$\hat{\Theta}(i) \cap S^{np}(i) = \emptyset \text{ while } \left( \hat{\Theta}(i) \cap S_1^{np}(i) \neq \emptyset \text{ and } \hat{\Theta}(i) \cap S_2^{np}(i) \neq \emptyset \right). \quad (2.85)$$

This situation is presented in Fig. 2.8. The computation of  $\Theta(i)$  using data-hypersectors is described in Algorithm 2 in Appendix B.1.

### 2.5.3 Data-Hyperspace Configuration Selection for Optimal SMI

By definition, the data-hyperstrip  $S^p(i)$  depends on the estimated parameter bounds  $\hat{\theta}_{z_u}^-(i), \hat{\theta}_{z_u}^+(i)$ ,  $u = 1, \dots, n$ , where  $z_u$  corresponds to  $\Omega_u$  or  $\Omega_u^\Theta$ . This dependency is reflected to the width of the data-hyperstrip and consequently to the intersection  $\hat{\Theta}(i) \cap S^p(i)$  or  $\hat{\Omega}(i) \cap S^p(i)$ . If the initialization of an SMI algorithm is realized taking into account a ‘large’ set (ellipsoid or orthotope) that contains  $\theta^\circ(0)$ , the bounds of  $\tilde{e}(i)$  will be loosen resulting in loosen parameter bounds. On the other hand, the utilization of the data-hypersector  $S^{np}(i)$  provides tighter parameter bounds, but demands the knowledge of the sign of  $\theta_u^\circ(i)$  at every time instant. Moreover, the utilization of an incorrect sign of  $\theta_u^\circ(i)$  may lead to  $\theta^\circ(i) \notin S^{np}(i)$ .

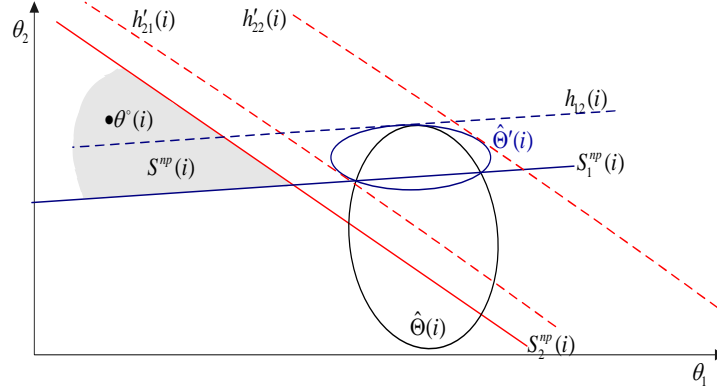


Figure 2.8: An example of empty intersection  $\hat{\Theta}(i)$  and  $S^{np}(i)$  ( $n=2$ )

In the case that the sign of  $\theta_u^\circ(i)$  is unknown, the signs of  $\hat{\theta}_{z_u}^-(i)$ ,  $\hat{\theta}_{z_u}^+(i)$  can be checked. If at the  $i$ th time instant  $\text{sgn}(\hat{\theta}_{z_u}^-(i)) = \text{sgn}(\hat{\theta}_{z_u}^+(i))$ ,  $\forall u$  then  $S(i) = S^{np}(i)$  defined through (2.41)-(2.43) using  $\text{sgn}(\theta_u^\circ(i)) = \text{sgn}(\hat{\theta}_{z_u}^+(i)(i))$ . If  $\text{sgn}(\hat{\theta}_{z_u}^-(i)) \neq \text{sgn}(\hat{\theta}_{z_u}^+(i))$ , then  $S(i) = S^p(i)$ .

## 2.6 Special Cases

### 2.6.1 Time Invariant Parameters

If the parameters of the system modelled by (2.1) and (2.2) are assumed to be time-invariant, then

$$w(i) = [w_1(i), \dots, w_n(i)]^T = [0, \dots, 0]^T, \quad (2.86)$$

$$\theta^\circ(i) = \theta^\circ(i-1) = \theta^\circ(0) = \theta^\circ, \quad \forall i, \quad (2.87)$$

resulting in:

$$y(i) = \phi(i)^T \theta^\circ. \quad (2.88)$$

Therefore, the objective of SMI is to determine the feasible parameter set  $F(i)$ , for which

$$\theta^\circ \in F(i), \quad \forall i. \quad (2.89)$$

Under the time-invariant parameters assumption, the feasible parameter set corresponds to the intersection of the data-hyperspace until the  $i$ th time instant:

$$F(i) = \bigcap_{i_0=1}^i S(i_0), \quad (2.90)$$

## 2. SET MEMBERSHIP IDENTIFICATION

with  $S(i) = S^p(i)$  (Fig.2.9a ) or  $S(i) = S^{np}(i)$  (Fig.2.9b).

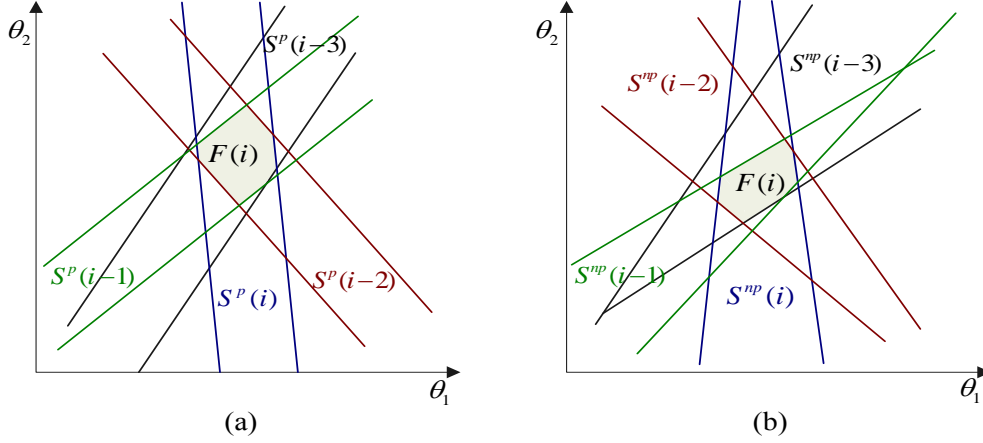


**Figure 2.9:** Feasible parameter set generated by a) data-hyperstrips, b) data-hypersectors (n=2)

The modification that should be made in the implementation of the SMI under the assumption of time invariant parameter vector is

$$\hat{\Theta}(i) = \Theta(i-1), \quad (2.91)$$

$$\hat{\Omega}(i) = \Omega(i-1). \quad (2.92)$$

Consequently, the data-hyperstrips are computed using the most recently parameter bounds arisen from the projection of  $\Theta(i-1)$  and  $\Omega(i-1)$ . In addition, the time invariant case entails that the sign of the components of the nominal parameter vector will not change with time,  $\text{sgn}(\theta_u^\circ(i)) = \text{sgn}(\theta_u^\circ(i-1)) = \text{sgn}(\theta_u^\circ)$ ,  $\forall i, u$ . Hence, the data-hypersectors can be determined under the a priori knowledge of  $\text{sgn}(\theta_u^\circ)$ ,  $\forall u$ .

For the orthotope-based SMI, it can be inferred from (2.62) and (2.63) that the computed upper (lower) parameter bound  $\theta_{\Omega_u}^+$ , ( $\theta_{\Omega_u}^-$ ) is monotonically decreasing (increasing) in time,  $\theta_{\Omega_u}^+(i) \leq \theta_{\Omega_u}^+(i-1)$  and  $\theta_{\Omega_u}^-(i) \geq \theta_{\Omega_u}^-(i-1)$ ,  $\forall i, u$ . Thus, the volume of the computed orthotope is monotonically decreasing, since:

$$\text{vol}(\Omega(i)) = \prod_{u=1}^n |\theta_{\Omega_u}^+(i) - \theta_{\Omega_u}^-(i)| \leq \prod_{u=1}^n |\theta_{\Omega_u}^+(i-1) - \theta_{\Omega_u}^-(i-1)| = \text{vol}(\Omega(i-1)). \quad (2.93)$$

It has to be highlighted that  $\text{vol}(\Theta(i)) \leq \text{vol}(\Theta(i-1))$ , while  $\Theta(i) \not\subseteq \Theta(i-1)$ . On the other hand,  $\text{vol}(\Omega(i)) \leq \text{vol}(\Omega(i-1))$  and  $\Omega(i) \subseteq \Omega(i-1)$ .

### 2.6.2 Equation Error

When the components of the regression vector are assumed to be perfectly known, implying that  $e_{\phi_u}(i) = 0, \forall i, u$ , and the noise term is introduced in the linearly parametrizable model as an equation error:

$$y^m(i) = \phi(i)^T \theta^\circ(i) + e'_y(i) \quad (2.94)$$

The equation error is also assumed to be unknown but bounded

$$|e'_y(i)| \leq e'^{\max}_y, \quad (2.95)$$

with  $e'^{\max}_y$  to be known a priori. Introducing (2.94) into (2.95) yields that the nominal parameter vector resides within a data-hyperstrip, defined as:

$$S'(i) = \{ \theta : y^m(i) - e'^{\max}_y \leq \phi(i)^T \theta \leq \tilde{y}^m(i) + e'^{\max}_y \}. \quad (2.96)$$

## 2.7 Conclusions

In this chapter, the orthotopic and an ellipsoidal SMI method is presented. In the general case, the linearly parametrizable system is assumed to be time-varying due to unknown but bounded parameter perturbations, while unknown but bounded measurement noise is assumed to corrupt both the output and the regression vector. Two formulations of the data-hyperspace are provided: a) the data-hyperstrip, whose computation is realized based on estimated parameter bounds, and b) the data-hypersector, which presupposes the knowledge of parameters' signs. In addition, an augmented orthotope (ellipsoid) is defined, incorporating the bounded parameter perturbations. The orthotopic SMI is encountered as a  $2n$  linear programming problem with  $2(n+1)$  constraints arisen from the augmented orthotope and the configuration of the data-hyperspace. The optimal solutions of this problem correspond to the vertices' coordinates of the estimated orthotope. The ellipsoidal SMI under the assumption of a data-hyperstrip is performed using the Optimal Volume Ellipsoid, which is properly customized so as to handle data-hypersectors. Further on, the appropriate modifications of the SMI methods under the assumption of time-invariant parameters and equation error.

## 2. SET MEMBERSHIP IDENTIFICATION

---

## Chapter 3

# Fault Detection and Diagnosis

### 3.1 Introduction

In this chapter, the Fault Detection and Diagnosis (FDD) procedure is analyzed based on orthotopic and ellipsoidal Set Membership Identification (SMI), aiming at capturing multiple abrupt parametric faults. The linearly parametrizable model is reformulated, so as to efficiently embed the abrupt parameter variations. Regardless of the type of the SMI procedure, a fault is detected when the existence of the parameter set is affected by the abrupt transition (jump) of the nominal parameter vector. In order to proceed to the fault diagnosis, a seamless update of the SMI procedure is realized by resetting the parametric set to a new one that contains the ‘jump’ parameter vector. The resetting procedure is followed by the fault isolation and identification mechanisms; the determination of the faulty parameters is the result of the consistency test based on the projections of the parametric sets, whose centers are used for estimating the size and the type of faults. Moreover, the modifications of the FDD procedure, considering a time invariant parameter vector are provided. The chapter is completed with a discussion concerning the fault detectability, the possibility of a better estimation of the time instant of fault occurrence applying a backward-in-time fault detection algorithm and the characterization of the algorithm sensitivity.

### 3.2 Fault Detection and Diagnosis Assumptions

Consider the jump linearly parametrizable model given as:

$$y(i) = \phi(i)^T \theta^\circ(i), \quad (3.1)$$

$$\theta^\circ(i) = \theta^\circ(i-1) + w(i) + (\Delta\theta(i) - \Delta\theta(i^{f_j})), \quad i^{f_j} < i \leq i^{f_{j+1}}, \quad (3.2)$$

### 3. FAULT DETECTION AND DIAGNOSIS

---

where  $y(i) \in \mathbb{R}$  is the noise-free model output,  $\phi(i) \in \mathbb{R}^n$  is the noise-free regression vector,  $\theta^\circ(i) \in \mathbb{R}^n$  is the unknown nominal parameter vector,  $\Delta\theta(i) \in \mathbb{R}^n$  are the parameter variation vectors,  $i^{f_j}$  is the time instant of fault occurrence,  $f_j$  is the fault-index, with  $i^{f_0} = 0$ ,  $\Delta\theta(i^{f_0}) = 0$ . Moreover, the observed output and components of regression vector are given in (2.3) and (2.4), while the unknown but bounded noise and parameter perturbations are described through (2.7), (2.8) and (2.9).

The jump-parameter case implies that after every fault occurrence the parameter variation vector remains constant for a time window with length

$$L_{f_j}^\circ = \arg \left\{ L_{f_j}^\circ = i^{f_{j+1}} - i^{f_j} : \|\Delta\theta(i^{f_j+i}) - \Delta\theta(i^{f_j})\| = 0, i \in \{0, \dots, L_{f_j}^\circ - 1\} \right\}. \quad (3.3)$$

Rather than demanding the knowledge of  $L_{f_j}^\circ$ , it is assumed that the parameter variation vector  $\Delta\theta(i^{f_j})$ ,  $\forall i^{f_j}$ , remains constant within a time window with length  $L \leq \min_{f_j} L_{f_j}^\circ$ . The jump-parameter case is graphically represented in Fig.3.1 for  $n = 2$ .

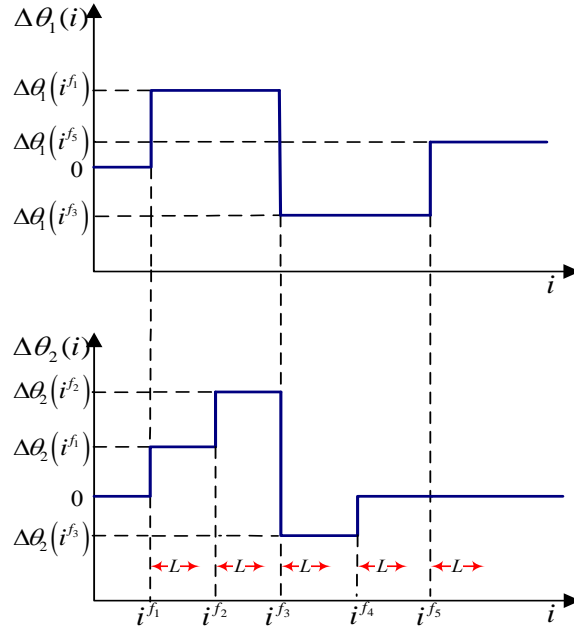


**Figure 3.1:** Graphical representation of the jump-parameter case ( $n = 2$ ).

The safe operation parameter bounds are assumed to be known a priori:

$$\theta_u^\circ(i) \in [\theta_u^{\min}, \theta_u^{\max}], \forall i, u = 1, \dots, n. \quad (3.4)$$

This condition implies that if the parameter perturbations and/or the abrupt parametric faults lead to a value of  $\theta_u^\circ(i)$  beyond this interval, the system halts its operation



and the fault diagnosis may be unattainable. Using (3.4), the following condition arises  $\forall u \in 1, \dots, n$

$$\Delta\theta_u(i) - \Delta\theta_u(i^{f_j}) = \theta^\circ(i) - \theta^\circ(i-1) - w(i) \in [\gamma_u^{\min}, \gamma_u^{\max}], \forall i^{f_j} \quad (3.5)$$

$$\gamma_u^{\min} = \theta_u^{\min} - \theta_u^{\max} - w_u^{\max}, \quad (3.6)$$

$$\gamma_u^{\max} = \theta_u^{\max} - \theta_u^{\min} - w_u^{\min}. \quad (3.7)$$

Under the a priori knowledge of: a) the structure of a jump linearly parametrizable model, b) the worst-case noise-bounds  $e_y^{\max}$ ,  $e_{\phi_u}^{\max}$ , c) the worst-case parameter perturbation bounds  $w_u^{\min}$ ,  $w_u^{\max}$ , the objective of the fault detection mechanism is to identify the time instants of detection  $i^{d_j}$  ( $i^{d_j} \geq i^{f_j}$ ) at which a fault has occurred. Ideally, these time instants should be identical to the fault-occurrence instants ( $i^{d_j} = i^{f_j}$ ) or close to them.

The fault diagnosis problem includes the fault isolation and fault identification mechanisms. The fault isolation procedure amounts to the localization of the source of the fault, indicating the component(s) of the parameter vector, influenced by abrupt variations. The task of fault identification is the estimation of the magnitude and time behavior of parameter variation.

### 3.3 Fault Detection Procedure

A fault is said to have occurred when an inconsistency between the measurement data and the inherent assumptions appears;

**Fault Detection Criterion 1** Given the data  $y^m(i^{d_j})$ ,  $\phi^m(i^{d_j})$ , a fault is detected when

$$\mathcal{Z}(i^{d_j}) \cap \mathcal{S}(i^{d_j}) = \emptyset, \quad (3.8)$$

where  $i^{d_j}$  denotes the time instant of fault detection,  $d_j$  is the detection-index and the fault is said to have occurred before the time instant  $i^{d_j}$ , and more specifically  $i^{d_{j-1}} < i^{f_j} \leq i^{d_j}$ .

If the FD procedure relies on:

- the **orthotope-based SMI**,  $\mathcal{Z}(i^{d_j})$  corresponds to the augmented orthotope  $\hat{\Omega}(i^{d_j})$ , which does not intersect with a data-hyperstrip (Fig. 3.2a) or a data-hypersector (Fig. 3.2b). The empty intersection implies that the linear programming problem stated in Section 2.5.1 has no feasible solution.
- the **ellipsoid-based SMI**,  $\mathcal{Z}(i^{d_j})$  corresponds to the augmented ellipsoid  $\hat{\Theta}(i^{d_j})$ . If the augmented ellipsoid does not intersect with a data-hyperstrip (Fig. 3.3a), the Algorithm 1 (OVE) in Appendix B.1 halts its operation at Step 3, while in case of a data-hypersector (Fig. 3.3b), the Algorithm 2 (customized OVE) in Appendix B.1 halts its operation at Step 3 or 18.

### 3. FAULT DETECTION AND DIAGNOSIS

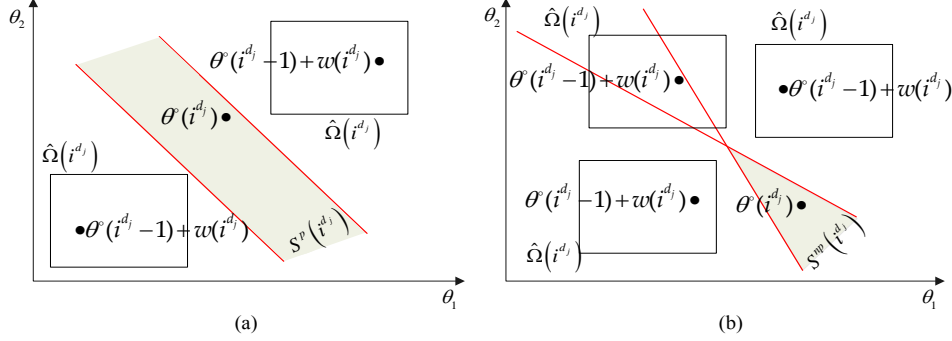


**Figure 3.2:** Graphical representation of fault detection based on the empty intersection between an orthotope and: a) a data-hyperstrip, b) a data-hypeselector ( $n = 2$ ).

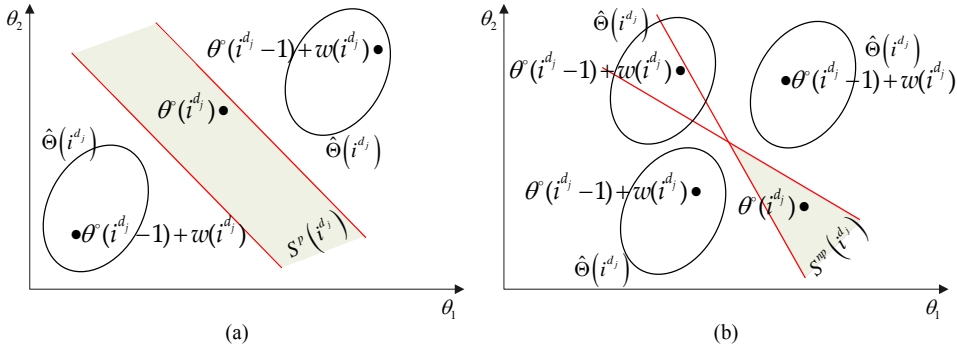


**Figure 3.3:** Graphical representation of fault detection based on the empty intersection between an ellipsoid and: a) a data-hyperstrip, b) a data-hypersector ( $n = 2$ ).

### 3.4 Fault Diagnosis Procedure

After the fault detection, the fault diagnosis mechanism is applied presupposing that no catastrophic damage has occurred and the condition given in (3.5) is not violated. Hence, using the measurement data after the fault detection, the FDs-strategy aims at isolating and identifying the faults, after a seamless updating of the parameter set and the data-hyperspace.

**Resetting Procedure** When a fault is detected, the SMI procedure is interrupted. In order to proceed with the fault isolation and identification, the parametric set  $\mathcal{Z}(i^{d_j})$

and the data-hyperspace  $S(i^{d_j})$  should be reset

$$Z(i^{d_j}) \longrightarrow Z^r(i^{d_j}), \quad (3.9)$$

$$S(i^{d_j}) \longrightarrow S^r(i^{d_j}), \quad (3.10)$$

in order to guarantee that

$$\left. \begin{array}{l} \theta^\circ(i^{d_j}) \in Z^r(i^{d_j}) \\ \text{and} \\ \theta^\circ(i^{d_j}) \in S^r(i^{d_j}) \end{array} \right\} \Rightarrow Z^r(i^{d_j}) \cap S^r(i^{d_j}) \neq \emptyset. \quad (3.11)$$

where  $\theta^\circ(i^{d_j})$  is the new nominal parameter vector.

**A. Orthotope-based Resetting Procedure** In the case that the FDD procedure is based on the orthotopic SMI, the resetting of the augmented orthotope at the time instant of fault detection is accomplished according to the following theorem [87].

**Theorem 3.4.1** If  $\theta^\circ(i^{d_j-1}) + w(i^{d_j}) \in \hat{\Omega}(i^{d_j})$ , then  $\theta^\circ(i^{d_j}) \in \Omega^r(i^{d_j})$ , where

$$\Omega^r(i^{d_j}) = \left\{ \theta : \begin{bmatrix} \theta_{\Omega_1}^{r-}(i^{d_j}) \\ \vdots \\ \theta_{\Omega_n}^{r-}(i^{d_j}) \end{bmatrix} \preceq \theta \preceq \begin{bmatrix} \theta_{\Omega_1}^{r+}(i^{d_j}) \\ \vdots \\ \theta_{\Omega_n}^{r+}(i^{d_j}) \end{bmatrix} \right\} \quad (3.12)$$

and

$$\theta_{\Omega_u}^{r-}(i^{d_j}) = \hat{\theta}_{\Omega_u}^-(i^{d_j}) + \gamma_u^{\min}, \quad (3.13)$$

$$\theta_{\Omega_u}^{r+}(i^{d_j}) = \hat{\theta}_{\Omega_u}^+(i^{d_j}) + \gamma_u^{\max}, \quad (3.14)$$

where  $\hat{\theta}_{\Omega_u}^-(i^{d_j})$ ,  $\hat{\theta}_{\Omega_u}^+(i^{d_j})$  are given in (2.52) and (2.53), respectively.

**Proof** The condition (3.5) implies that  $\Delta\theta(i) - \Delta\theta(i^{f_{j-1}})$  resides within an orthotope defined as:

$$\Omega_{\Delta\theta} = \left\{ \theta : \begin{bmatrix} \gamma_1^{\min} \\ \vdots \\ \gamma_n^{\min} \end{bmatrix} \preceq \theta \preceq \begin{bmatrix} \gamma_1^{\max} \\ \vdots \\ \gamma_n^{\max} \end{bmatrix} \right\}. \quad (3.15)$$

Assuming that  $\theta^\circ(i^{d_j-1}) + w(i^{d_j}) \in \hat{\Omega}(i^{d_j})$  and  $\theta^\circ(i^{d_j}) = \theta^\circ(i^{d_j-1}) + w(i^{d_j}) + \Delta(i^{d_j}) - \Delta(i^{f_{j-1}})$ , it yields that  $\theta^\circ(i^{d_j}) \in \Omega^r(i^{d_j})$  with:

$$\Omega^r(i^{d_j}) = \arg \left\{ \Omega : \Omega = \hat{\Omega}(i^{d_j}) \oplus \Omega_{\Delta\theta} \right\}, \quad (3.16)$$

whose vertices' coordinates are defined through (3.13)-(3.14).

### 3. FAULT DETECTION AND DIAGNOSIS

---

**B. Ellipsoid-based Resetting Procedure** The resetting procedure when the FDD procedure relies on the ellipsoidal SMI is realized according to the following theorem.

**Theorem 3.4.2** If  $\theta^\circ(i^{d_j} - 1) + w(i^{d_j}) \in \hat{\Theta}(i^{d_j})$ , then  $\theta^\circ(i^{d_j}) \in \Theta^r(i^{d_j})$ , with the centroid and the shape matrix of  $\Theta^r(i^{d_j})$  given as:

$$\theta_r^c(i^{d_j}) = \hat{\theta}^c(i^{d_j}) \quad (3.17)$$

$$P^r(i^{d_j}) = U(i^{d_j}) \Sigma^r(i^{d_j}) U^T(i^{d_j}), \quad (3.18)$$

$$\Sigma^r(i^{d_j}) = \Sigma(i^{d_j}) + 2\gamma \Sigma(i^{d_j})^{1/2} + \gamma^2 I, \quad (3.19)$$

$$\hat{P}(i^{d_j}) = U(i^{d_j}) \Sigma(i^{d_j}) U^T(i^{d_j}). \quad (3.20)$$

**Proof** The worst case scenario amounts to the location of  $\theta^\circ(i^{d_j} - 1) + w(i^{d_j})$  almost on the closure of  $\hat{\Theta}(\hat{\theta}^c(i^{d_j}), \hat{P}(i^{d_j}))$ . The closure of this ellipsoid should be enlarged by the maximum possible parameter deviation given as

$$\|\Delta\theta(i) - \Delta\theta(i^{f_{j-1}})\| = \sqrt{\sum_{u=1}^n (\Delta\theta_u(i) - \Delta\theta_u(i^{f_{j-1}}))^2} \leq \sqrt{\sum_{u=1}^n \max(|\gamma_u^{\min}|, |\gamma_u^{\max}|)} = \gamma.$$

Based on the singular value decomposition of the shape matrix  $\hat{P}(i^{d_j})$  given in (3.20), the  $\Sigma(i^{d_j})$ -diagonal matrix contains the squared elements of the semiaxes' lengths. Let these elements be  $\lambda_u$ ,  $u = 1, \dots, n$ ; then to ensure the presence of  $\theta^\circ(i^{d_j})$  inside an ellipsoid  $\Theta^r(i^{d_j})$  with the same centroid as in  $\hat{\Theta}(i^{d_j})$ , these elements must be set to  $(\sqrt{\lambda_u} + \gamma)^2 = \lambda_u + 2\gamma\sqrt{\lambda_u} + \gamma^2$ . In a more compact form,  $\Sigma^r(i^{d_j}) = \Sigma(i^{d_j}) + 2\gamma \Sigma(i^{d_j})^{1/2} + \gamma^2 I$ .

**C. Data-hyperstrip Resetting Procedure** If  $S(i^{d_j})$  is a data-hyperstrip, it has been generated according to (2.29) with the worst-case noise bound  $\tilde{e}^{\max}(i^{d_j}) = e_y^{\max} + \sum_{u=1}^n e_{\phi_u}^{\max} \max(|\theta_{z_u}^-(i^{d_j})|, |\theta_{z_u}^+(i^{d_j})|)$ , where  $\theta_{z_u}^-(i^{d_j}), \theta_{z_u}^+(i^{d_j})$  are the parameter bounds computed using the projection of the augmented orthotope  $\hat{\Omega}(i^{d_j})$  or the augmented ellipsoid  $\hat{\Theta}(i^{d_j})$ . Since these parametric sets have been reset according to Theorem 3.4.1 or Theorem 3.4.2, the data-hyperstrip  $S(i^{d_j})$  should also be reset. Hence, the resetting data-hyperspace  $S^p(i^{d_j})$  is a data-hyperstrip  $S_r^p(i^{d_j})$  defined by (2.29). The bound of the noise  $\tilde{e}^{\max}(i^{d_j})$  is computed as:

- in the orthotopic SMI-based resetting procedure,

$$\tilde{e}^{\max}(i^{d_j}) = e_y^{\max} + \sum_{u=1}^n e_{\phi_u}^{\max} \max(|\theta_{\Omega_u}^{r-}(i^{d_j})|, |\theta_{\Omega_u}^{r+}(i^{d_j})|) \quad (3.24)$$

where  $\theta_{\Omega_u}^{r-}(i^{d_j}), \theta_{\Omega_u}^{r+}(i^{d_j})$  are given in (3.13) and (3.14), respectively,

- in the ellipsoidal SMI-based resetting procedure,

$$\tilde{e}^{\max}(i^{d_j}) = e_y^{\max} + \sum_{u=1}^n e_{\phi_u}^{\max} \max\left(\left|\theta_{\Omega_u^\ominus}^{r-}(i^{d_j})\right|, \left|\theta_{\Omega_u^\ominus}^{r+}(i^{d_j})\right|\right) \quad (3.22)$$

with

$$\theta_{\Omega_u^\ominus}^{r-}(i^{d_j}) = -\rho\left(q_{u+n}^o \left| \Theta^r(i^{d_j}) \right.\right) \quad (3.23)$$

$$\theta_{\Omega_u^\ominus}^{r+}(i^{d_j}) = \rho\left(q_u^o \left| \Theta^r(i^{d_j}) \right.\right) \quad (3.24)$$

with  $q_u^o$ ,  $q_{u+n}^o$  given in (2.19).

If  $S(i^{d_j})$  is a data-hypersector, three distinct resetting procedures can be applied:

- if  $\theta_u^{\min} \geq 0$  or  $\theta_u^{\max} \leq 0$ ,  $\forall u$ , then the data-hypersector will not be reset.
- if  $\theta_u^{\min} < 0 < \theta_u^{\max}$  and

$$\operatorname{sgn}\left(\theta_{\Omega_u^\ominus}^{r-}(i^{d_j})\right) = \operatorname{sgn}\left(\theta_{\Omega_u^\ominus}^{r+}(i^{d_j})\right), \quad (3.25)$$

or

$$\operatorname{sgn}\left(\theta_{\Omega_u^\ominus}^{r-}(i^{d_j})\right) = -\operatorname{sgn}\left(\theta_{\Omega_u^\ominus}^{r+}(i^{d_j})\right), \quad (3.26)$$

then the resetting data-hyperspace  $S^r(i^{d_j})$  is a data-hypersector  $S_r^{np}(i^{d_j})$ , which is defined through (2.41)–(2.43), using the sign presented in (3.25) or (3.26) instead of  $\operatorname{sgn}(\theta^\circ(i^{d_j}))$ .

- if  $\theta_u^{\min} < 0 < \theta_u^{\max}$  and (3.25) or (3.26) is invalid, then the resetting data-hyperspace  $S^r(i^{d_j})$  is a data-hyperstrip  $S_r^p(i^{d_j})$  defined by (2.29) and (3.21) or (3.22).

**Remark 3.4.3** In case that the noise-errors are induced as an equation error in the jump linearly parametrizable model, as described in Section 2.6.2, the data-hyperstrip resetting procedure is omitted.

The orthotope or ellipsoid at the time instant of fault detection is generated as:

$$\Omega(i^{d_j}) = \arg\left\{\Omega : \Omega \supseteq \left(\Omega^r(i^{d_j}) \cap S^r(i^{d_j})\right)\right\}, \quad (3.27)$$

or

$$\Theta(i^{d_j}) = \arg\left[\min\left\{\operatorname{vol}(\Theta) : \Theta \supset \left[\Theta^r(i^{d_j}) \cap S^r(i^{d_j})\right]\right\}\right], \quad (3.28)$$

### 3. FAULT DETECTION AND DIAGNOSIS

---

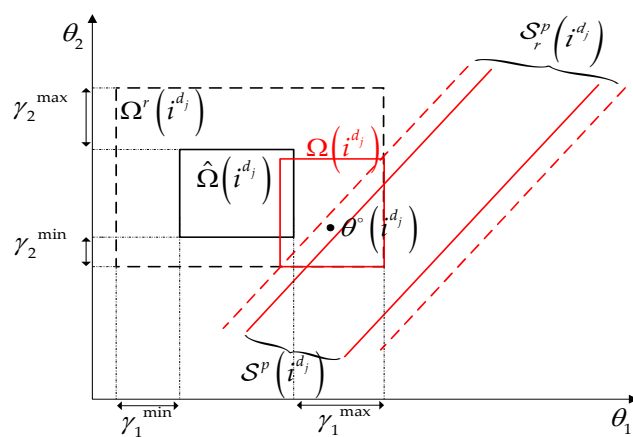


Figure 3.4: Detected fault case and orthotope-based resetting procedure ( $n = 2$ ).

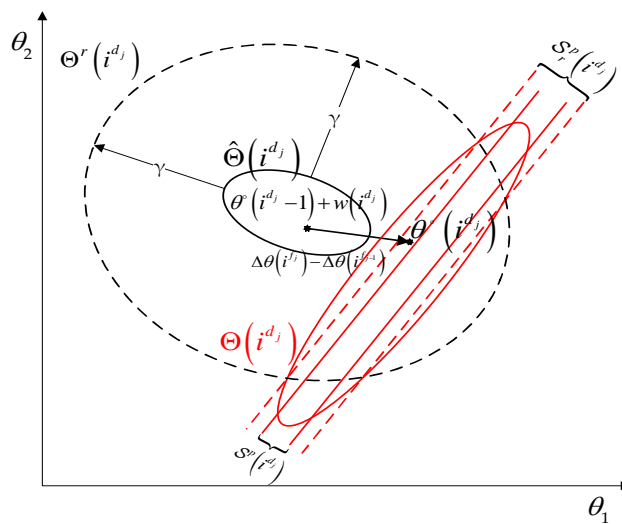


Figure 3.5: Detected fault case and ellipsoid-based resetting procedure ( $n = 2$ ).

### 3.4.1 Fault Isolation Procedure

After the fault detection at  $i^{d_j}$ , the orthotopes  $\Omega(i^{d_j} + i)$  or the ellipsoids  $\Theta(i^{d_j} + i)$  for  $1 \leq i < i^{d_{j+1}} - i^{d_j}$  will be computed according to the SMI procedure presented in Section 2.5.1 or 2.5.2, respectively, containing the varied nominal parameter vector

$$\theta^\circ(i^{d_j} + i) \in \Omega(i^{d_j} + i) \left( \Theta(i^{d_j} + i) \right), \quad (3.29)$$

$$\theta_u^\circ(i^{d_j} + i) \in \Omega_u(i^{d_j} + i) \left( \Omega_u^\ominus(i^{d_j} + i) \right), \quad \forall u, \quad (3.30)$$

where  $\Omega_u(i)$ ,  $(\Omega_u^\ominus(i^{d_j} + i))$  is defined in (2.11)((2.22)).

In order to determine the component(s) of parameter vector subject to abrupt variations, denoted as faulty component(s), the worst-case parametric sets (orthotopes or ellipsoids) within which the nominal parameter vector would have resided if no fault had occurred should first be computed [87].

#### 3.4.1.1 Fault Isolation based on Orthotopic SMI

**Lemma 3.4.4** Due to parameter perturbations and under faultless conditions, the deviation vector  $\theta^\circ(i_1) - \theta^\circ(i_0)$  with  $i_0 < i_1$  resides within the orthotope  $\Omega_{\delta i}$ , defined as

$$\Omega_{\delta i} = \left\{ \theta : \begin{bmatrix} \delta i \cdot w_1^{\min} \\ \vdots \\ \delta i \cdot w_n^{\min} \end{bmatrix} \preceq \theta \preceq \begin{bmatrix} \delta i \cdot w_1^{\max} \\ \vdots \\ \delta i \cdot w_n^{\max} \end{bmatrix} \right\} \quad (3.31)$$

where  $\delta i = i_1 - i_0$ ,  $\delta i \geq 1$ .

**Proof** Based on (2.2) and for  $\delta i \geq 1$ , it yields:

$$\begin{aligned} \theta^\circ(i_0 + 1) &= \theta^\circ(i_0) + w(i_0 + 1), \\ \theta^\circ(i_0 + 2) &= \theta^\circ(i_0 + 1) + w(i_0 + 2) \\ &= \theta^\circ(i_0) + \sum_{t=i_0+1}^{i_0+2} w(t) \\ &\vdots \\ \theta^\circ(i_0 + \delta i) &= \theta^\circ(i_0) + \sum_{t=i_0+1}^{i_0+\delta i} w(t), \end{aligned}$$

or else,

$$\theta^\circ(i_1) = \theta^\circ(i_0) + \sum_{t=i_0+1}^{i_1} w(t). \quad (3.32)$$

### 3. FAULT DETECTION AND DIAGNOSIS

---

Taking into account that  $w(i) \in \Omega^w$ ,  $\forall i$ , then

$$\sum_{t=i_0+1}^{i_1} w(t) \in \underbrace{\Omega^w \oplus \Omega^w \oplus \dots \oplus \Omega^w}_{\delta i} = \Omega_{\delta i} \quad (3.33)$$

with  $\Omega_{\delta i}$  defined in (3.31). From (3.32) and (3.33), it yields that  $\theta^\circ(i_1) - \theta^\circ(i_0) \in \Omega_{\delta i}$ .

**Proposition 3.4.5** If  $\theta^\circ(i_0) \in \Omega(i_0)$ , then under faultless conditions

$$\theta^\circ(i_1) \in \hat{\Omega}(i_1|i_0) \Leftrightarrow \theta_u^\circ(i_1) \in \hat{\Omega}_u(i_1|i_0), \forall u, \quad (3.34)$$

with

$$\hat{\Omega}(i_1|i_0) = \arg \left\{ \Omega : \Omega = \Omega_{\delta i}^* \oplus \Omega(i_0) \right\}, \quad (3.35)$$

$$\hat{\Omega}_u(i_1|i_0) = \{ \theta_u : \theta_u \in [\delta i \cdot w_u^{\min} + \theta_u^-(i_0), \delta i \cdot w_{\Omega_u}^{\max} + \theta_{\Omega_u}^+(i_0)] \}, \quad (3.36)$$

where  $\hat{\Omega}(i_1|i_0)$  is the worst-case orthotope and the minimum and maximum value of  $\hat{\Omega}_u^\circ(i_1|i_0)$  are the worst-case lower and upper parameter bound, respectively.

An example of the worst case orthotopes,  $\hat{\Omega}(i_1|i_0)$ , and the orthotopes arisen from the normal operation of the SMI (Section 2.5.1),  $\Omega(i_1)$ , using the data-hypersector  $S^{np}(i_1)$  is presented in Fig. 3.6, for  $n=2$ ,  $i_1 = i_0 + 1, i_0 + 2$  and  $w_u^{\min} > 0$ ,  $\forall u$ .

After the fault detection, the following lemmas can be offered for fault isolation, relying on the conditions (3.30) and (3.34) with  $i_0 = i^{d_j} - 1$ ,  $i_1 = i^{d_j} + i$  and  $0 \leq i < i^{d_{j+1}} - i^{d_j}$ .

**Lemma 3.4.6** The  $u$ th component of parameter vector is characterized as faulty at the time instances  $i^{u*}$  at which

$$\hat{\Omega}_u(i^{u*}|i^{d_j} - 1) \cap \Omega_u(i^{u*}) = \emptyset, \quad (3.37)$$

with  $i^{d_j} \leq i^{u*} < i^{d_{j+1}}$ .

**Proof** Since  $\theta_u^\circ(i^{u*}) \in \Omega_u(i^{u*})$  and (3.37) is valid, then  $\theta_u^\circ(i^{u*}) \notin \hat{\Omega}_u(i^{u*}|i^{d_j} - 1)$ . This is in contrast with the condition (3.34) and the  $u$ th component of parameter vector is defined as faulty at the time instant  $i^{u*}$ .

**Lemma 3.4.7** The  $u$ th component of parameter vector is characterized as non-faulty at the earliest time instant  $i^{u*}$  if

$$\hat{\Omega}_u(i^{u*}|i^{d_j} - 1) \cap \Omega_u(i^{u*}) = \Omega_u(i^{u*}), \quad (3.38)$$

with  $i^{d_j} \leq i^{u*} < i^{d_{j+1}}$ .



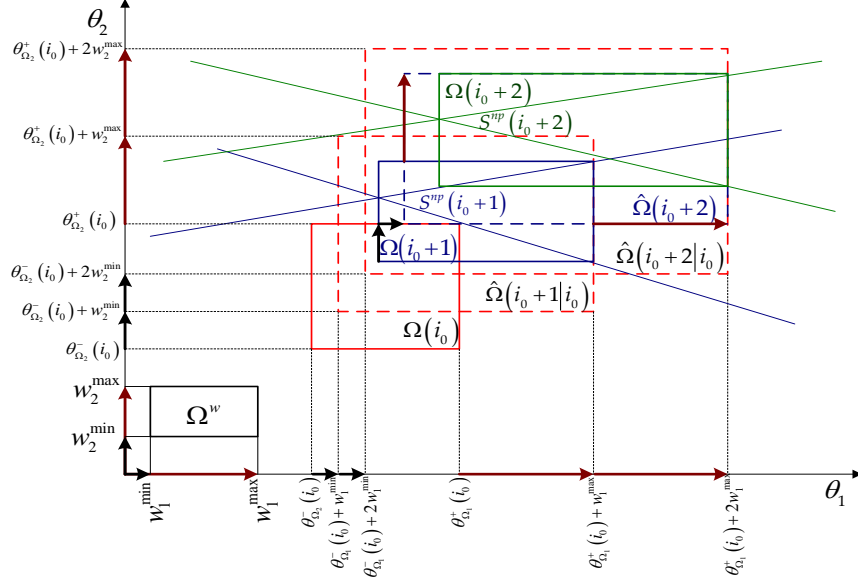


**Figure 3.6:** Graphical representation of the worst case orthotopes,  $\hat{\Omega}(i_1|i_0)$ , and the orthotopes arisen from the normal operation of the SMI (Section 2.5.1),  $\Omega(i_1)$

**Proof** Since  $\theta_u^\circ(i^{u*}) \in \Omega_u(i^{u*})$  and (3.38) is valid, then  $\theta_u^\circ(i^{u*}) \in \hat{\Omega}_u(i^{u*}|i^{d_j} - 1)$ . Hence, based on the condition (3.34), the  $u$ th component of parameter vector is characterized as non-faulty at the time instant  $i^{u*}$ . It can be proven that the  $u$ th component will be characterized as non-faulty at future time instances  $i^{u*} + i$  with  $1 \leq i < i^{d_{j+1}} - i^*$ . In particular, Equation (3.38) implies that  $\hat{\Omega}_u(i^{u*}|i^{d_j} - 1) \supseteq \Omega_u(i^{u*})$  and

$$\delta i \cdot w_u^{\min} + \theta_{\Omega_u}^-(i^{d_j} - 1) \leq \theta_{\Omega_u}^-(i^{u*}), \quad (3.39)$$

$$\delta i \cdot w_u^{\max} + \theta_{\Omega_u}^+(i^{d_j} - 1) \geq \theta_{\Omega_u}^+(i^{u*}) \quad (3.40)$$

with  $\delta i = i^{u*} - (i^{d_j} - 1)$ . Adding  $w_u^{\min}$ ,  $w_u^{\max}$  in both sides of (3.39) and (3.40), respectively, yields:

$$\begin{aligned} (i^{u*} - (i^{d_j} - 1)) \cdot w_u^{\min} + \theta_{\Omega_u}^-(i^{d_j} - 1) + w_u^{\min} &\leq \theta_{\Omega_u}^-(i^{u*}) + w_u^{\min} \iff \\ ((i^{u*} + 1) - (i^{d_j} - 1)) \cdot w_u^{\min} + \theta_{\Omega_u}^-(i^{d_j} - 1) &\leq \hat{\theta}_{\Omega_u}^-(i^{u*} + 1) \end{aligned} \quad (3.41)$$

$$\begin{aligned} (i^{u*} - (i^{d_j} - 1)) \cdot w_u^{\max} + \theta_{\Omega_u}^+(i^{d_j} - 1) + w_u^{\min} &\geq \theta_{\Omega_u}^+(i^{u*}) + w_u^{\max} \iff \\ ((i^{u*} + 1) - (i^{d_j} - 1)) \cdot w_u^{\max} + \theta_{\Omega_u}^+(i^{d_j} - 1) &\geq \hat{\theta}_{\Omega_u}^+(i^{u*} + 1). \end{aligned} \quad (3.42)$$

Combining (2.62) and (2.63) with (3.41) and (3.42), the following inequalities are obtained:

### 3. FAULT DETECTION AND DIAGNOSIS

---

$$\begin{aligned} \left( (i^{u^*} + 1) - (i^{d_j} - 1) \right) \cdot w_u^{\min} + \theta_{\Omega_u}^- (i^{d_j} - 1) &\leq \theta_{\Omega_u}^- (i^{u^*} + 1), \\ \left( (i^{u^*} + 1) - (i^{d_j} - 1) \right) \cdot w_u^{\max} + \theta_{\Omega_u}^+ (i^{d_j} - 1) &\geq \theta_{\Omega_u}^+ (i^{u^*} + 1) \end{aligned}$$

or else

$$\hat{\Omega}_u \left( i^{u^*} + 1 | i^{d_j} - 1 \right) \cap \Omega_u (i^{u^*} + 1) = \Omega_u (i^{u^*} + 1). \quad (3.43)$$

Following the same procedure iteratively, it yields

$$\hat{\Omega}_u \left( i^{u^*} + i | i^{d_j} - 1 \right) \cap \Omega_u (i^{u^*} + i) = \Omega_u (i^{u^*} + i) \quad (3.44)$$

with  $0 \leq i < i^{d_{j+1}} - i^*$  and the  $u$ th component is characterized as non-faulty for the time window  $[i^{u^*}, i^{d_{j+1}})$ .

If there is no time instant  $i \in [i^{d_j}, \dots, i^{d_{j+1}})$  for which Equations (3.37), or (3.38) are not valid, then there can be no inference for the status of the  $u$ th component of the parameter vector.

#### 3.4.1.2 Fault Isolation based on ellipsoidal SMI

**Lemma 3.4.8** Due to parameter perturbations and under faultless conditions, the deviation vector  $\theta^\circ(i_1) - \theta^\circ(i_0)$  with  $i_0 < i_1$  resides within the ellipsoid  $\Theta_{\delta i}(\theta_{\delta i}^c, P_{\delta i})$ , defined as

$$\theta_{\delta i}^c = \delta i \cdot w^c, \quad (3.45)$$

$$P_{\delta i} = \delta i^2 \cdot P^w \quad (3.46)$$

where  $\delta i = i_1 - i_0$ ,  $\delta i \geq 1$ .

**Proof** According to [84], the sum of two ellipsoids  $\Theta_1(c_1, P_1)$  and  $\Theta_1(c_2, P_2)$  with  $P_1 = \nu_P P_2$  is an ellipsoid  $\Theta_{12}(c_{12}, P_{12})$ , where

$$c_{12} = c_1 + c_2, \quad (3.47)$$

$$P_{12} = (\sqrt{\nu_P} + 1)^2 P_2 \quad (3.48)$$

Taking into account that  $w(i) \in \Theta^w(w^c, P^w)$ ,  $\forall i$ , ( $\Theta^w$  is defined in Appendix A.1) then

$$\begin{aligned} w(i_0 + 1) &\in \Theta^w(w^c, P^w) \\ w(i_0 + 1) + w(i_0 + 2) &\in \Theta^w(2w^c, 4P^w) \\ (w(i_0 + 1) + w(i_0 + 2)) + w(i_0 + 3) &\in \Theta^w(3w^c, 9P^w) \\ &\vdots \\ \sum_{t=i_0+1}^{i_1} w(t) &\in \Theta^w(\delta i \cdot w^c, \delta i^2 \cdot P^w) \end{aligned} \quad (3.49)$$

Defining  $\Theta_{\delta i} = \Theta^w(\delta i \cdot w^c, \delta i^2 \cdot P^w)$  and combining (3.32) with (3.49) implies that  $\theta^\circ(i_1) - \theta^\circ(i_0) \in \Theta_{\delta i}(\theta_{\delta i}^c, P_{\delta i})$ .

**Proposition 3.4.9** If  $\theta^\circ(i_0) \in \Theta(\theta^c(i_0), P(i_0))$ , then under faultless conditions

$$\theta^\circ(i_1) \in \hat{\Theta}(i_1|i_0) \Leftrightarrow \theta_u^\circ(i_1) \in \hat{\Omega}_u^\Theta(i_1|i_0), \forall u \quad (3.50)$$

where

- $\hat{\Theta}(i_1|i_0)$  is the worst-case ellipsoid and its centroid and the shape matrix are computed as:

$$\hat{\theta}^c(i_1|i_0) = \theta^c(i_0) + \theta_{\delta i}^c, \quad (3.51)$$

$$\hat{P}(i_1|i_0) = (\zeta_{\delta i} + 1)P(i_0) + \left(\frac{1}{\zeta_{\delta i} + 1}\right)P_{\delta i}. \quad (3.52)$$

where the variable  $\zeta_{\delta i}$  is the unique positive solution of  $\sum_{u=1}^n \frac{1}{\lambda_u^{\delta i} + \zeta_{\delta i}} = \frac{n}{\zeta_{\delta i}(\zeta_{\delta i} + 1)}$  and  $\lambda_u^{\delta i}$  are the solutions of the generalized eigenvalue problem  $P_{\delta i}\chi_u = \lambda_u^{\delta i}P(i-1)\chi_u$ , where  $\delta i = i_1 - i_0$ ,  $\delta i \geq 1$ .

- $\Omega_u^\Theta(i^{d_j} + i) = \text{proj}_u(\hat{\Omega}_u^\Theta(i_1|i_0))$ , or else

$$\hat{\Omega}_u^\Theta(i_1|i_0) = \{\theta_u : \theta_u \in [-\rho(q_{u+n}^o | \hat{\Theta}(i_1|i_0)), \rho(q_u^o | \hat{\Theta}(i_1|i_0))]\}, \quad (3.53)$$

and the minimum and maximum value of  $\hat{\Omega}_u^\Theta(i_1|i_0)$  are the worst-case upper and lower parameter bound, respectively.

After the fault detection, the following lemmas can be offered for fault isolation, relying on the conditions (3.30) and (3.50) with  $i_0 = i^{d_j} - 1$ ,  $i_1 = i^{d_j} + i$  and  $0 \leq i < i^{d_{j+1}} - i^{d_j}$ .

**Lemma 3.4.10** The  $u$ th component of parameter vector is characterized as faulty at the time instances  $i^{u*}$  at which

$$\hat{\Omega}_u^\Theta(i^{u*}|i^{d_j} - 1) \cap \Omega_u^\Theta(i^{u*}) = \emptyset, \quad (3.54)$$

with  $i^{d_j} \leq i^{u*} < i^{d_{j+1}}$ .

**Proof** Since  $\theta_u^\circ(i^{u*}) \in \Omega_u^\Theta(i^{u*})$  and (3.54) is valid, then  $\theta_u^\circ(i^{u*}) \notin \hat{\Omega}_u^\Theta(i^{u*}|i^{d_j} - 1)$ . This is in contrast with the condition 3.50 and the  $u$ th component of parameter vector is defined as ‘faulty’ at the time instant  $i^{u*}$ .

### 3. FAULT DETECTION AND DIAGNOSIS

---

**Lemma 3.4.11** The  $u$ th component of parameter vector is characterized as non-faulty at the earliest time instant  $i^{u*}$  if

$$\hat{\Omega}_u^\Theta(i^{u*}|i^{d_j}-1) \cap \Omega_u^\Theta(i^{u*}) = \Omega_u^\Theta(i^{u*}), \quad (3.55)$$

with  $i^{d_j} \leq i^{u*} < i^{d_{j+1}}$ .

**Proof** Since  $\theta_u^\circ(i^{u*}) \in \Omega_u^\Theta(i^{u*})$  and (3.55) is valid, then  $\theta_u^\circ(i^{u*}) \in \hat{\Omega}_u^\Theta(i^{u*}|i^{d_j}-1)$ . Hence, based on the condition 3.50, the  $u$ th component of parameter vector is defined as ‘non-faulty’ at the time instant  $i^{u*}$ .

If there is no time instant  $i \in [i^{d_j}, \dots, i^{d_{j+1}}]$  for which Equations (3.54), or (3.55) are not valid, then there can be no inference for the status of the  $u$ th component of the parameter vector.

#### 3.4.2 Fault Identification Procedure

##### 3.4.2.1 Fault Identification based on Orthotopic SMI

After the fault isolation event in which the faulty  $u$ th components of the parameter vector were isolated as the ones for which (3.37) is satisfied, the most likely size of  $\Delta\theta_u(i^{f_j}) - \Delta\theta_u(i^{f_{j-1}})$  can be estimated based on the distance of the centers of  $\hat{\Omega}_u(i^{u*}|i^{d_j}-1)$  and  $\Omega_u(i^{u*})$  [87]. Particularly,

$$\tilde{d}_{\theta_u}(i^{u*}) = \theta_{\Omega_u}^c(i^{u*}) - \left( \theta_{\hat{\Omega}_u}^c(i^{d_j}-1) + \delta i \frac{w_u^{\max} + w_u^{\min}}{2} \right), \quad (3.56)$$

where  $\theta_u^c(i)$  is computed via (2.12) and  $\delta i = i^{u*} - (i^{d_j} - 1)$ .

##### 3.4.2.2 Fault Identification based on ellipsoidal SMI

After the fault isolation event in which the faulty  $u$ th components of the parameter vector were isolated as the ones for which (3.54) is satisfied, the most likely size of  $\Delta\theta_u(i^{f_j}) - \Delta\theta_u(i^{f_{j-1}})$  can be estimated based on the distance of the centers of  $\hat{\Omega}_u^\Theta(i^{u*}|i^{d_j}-1)$  and  $\Omega_u^\Theta(i^{u*})$ . Particularly,,

$$\tilde{d}_{\theta_u}(i^{u*}) = \theta_u^c(i^{u*}) - \hat{\theta}_u^c(i^{u*}|i^{d_j}-1). \quad (3.57)$$

### 3.5 Special Case: Time Invariant Parameters

Under the assumption of a time invariant parameters after a fault occurrence, the jump linearly parametrizable model described through (3.1)-(3.2) is transformed to:

$$y(i) = \phi(i)^T (\theta^\circ + \Delta\theta(i^{f_{j-1}})), \text{ for } i^{f_{j-1}} \leq i < i^{f_j}. \quad (3.58)$$

The details of the transformation are provided in Appendix A.2.

The components of the nominal parameter vectors are restricted by the safe operation bounds, implying that:

$$\theta_u^\circ + \Delta\theta(i^{f_j}) \in [\theta_u^{\min}, \theta_u^{\max}], \quad \forall i^{f_j}, u = 1, \dots, n \quad (3.59)$$

and consequently

$$\Delta\theta(i^{f_j}) \in [\tilde{\gamma}_u^{\min}, \tilde{\gamma}_u^{\max}], \quad \forall i^{f_j}, \quad (3.60)$$

$$\tilde{\gamma}_u^{\min} = \theta_u^{\min} - \theta_u^{\max}, \quad (3.61)$$

$$\tilde{\gamma}_u^{\max} = \theta_u^{\max} - \theta_u^{\min} = -\tilde{\gamma}_u^{\min}. \quad (3.62)$$

### 3.5.1 Fault Detection Procedure

In case of time-invariant parameters, the fault detection criterion defined by (1) is modified as:

$$\mathcal{Z}(i^{d_j} - 1) \cap \mathcal{S}(i^{d_j}) = \emptyset, \quad (3.63)$$

where  $\mathcal{Z}(i^{d_j} - 1)$  corresponds to  $\Omega(i^{d_j} - 1)$  or  $\Theta(i^{d_j} - 1)$ , depending on the type of the SMI based on which the FDD procedure is performed.

However, in the ellipsoidal SMI-based FDD technique, another consistency test can be applied for fault detection. Specifically, rather than relying solely on the ellipsoidal SMI method in which  $\text{vol}(\Theta(i)) \leq \text{vol}(\Theta(i-1))$ , while  $\Theta(i) \not\subseteq \Theta(i-1)$ , the intersection of the support orthotopes is used as another fault detection criterion, defined as [88]:

$$\mathcal{X}(i) = \bigcap_{t=1}^i \Omega^\Theta(t), \quad (3.64)$$

or equivalently,

$$\mathcal{X}(i) = \mathcal{X}(i-1) \cap \Omega^\Theta(i). \quad (3.65)$$

It should be noted that unlike the ellipsoidal methods  $\mathcal{X}(i) \subseteq \mathcal{X}(i-1)$  and  $\text{vol}(\mathcal{X}(i)) \leq \text{vol}(\mathcal{X}(i-1))$ .

In addition, the projection of the  $\mathcal{X}(i)$  on each axis is denoted as:

$$\mathcal{X}_u(i) = \text{proj}_u(\mathcal{X}) = \left\{ \theta_u : \theta_u \in [\theta_{x_u}^-(i), \theta_{x_u}^+(i)] \right\} \quad (3.66)$$

and its center computed as:

$$\theta_{x_u}^c(i) = \frac{\theta_{x_u}^+(i) + \theta_{x_u}^-(i)}{2}, \quad u = 1, \dots, n. \quad (3.67)$$

### 3. FAULT DETECTION AND DIAGNOSIS

---

The centroid of the  $\mathcal{X}(i)$  is defined as:

$$\theta_{\mathcal{X}}^c(i) = [\theta_{x_1}^c(i), \dots, \theta_{x_n}^c(i)]^T. \quad (3.68)$$

It has to be mentioned that  $\forall u$ ,  $\mathcal{X}_u(i)$ , is monotonically converging to the nominal parameter values  $\theta_u^o$ , in contrast with the projection of the support orthotope,  $\Omega_u^\Theta(i)$ . Therefore, in the ellipsoidal SMI using data-hyperstrips,  $S^p(i)$  can be defined through (2.29) with  $\tilde{e}^{\max}(i)$  computed as:

$$\tilde{e}^{\max}(i) = e_y^{\max} + \sum_{u=1}^n e_{\phi_u}^{\max} \max\left(\left|\theta_{x_u}^-(i)\right|, \left|\theta_{x_u}^+(i)\right|\right), \quad (3.69)$$

The aforementioned sequence of orthotopes can be used for the fault detection:

**Fault Detection Criterion 2** Given the data  $y^m(i^{d_j})$ ,  $\phi^m(i^{d_j})$ , a fault is detected when

$$\mathcal{X}(i^{d_j}) = \mathcal{X}(i^{d_j} - 1) \cap \Omega^\Theta(i^{d_j}) = \emptyset. \quad (3.70)$$

where  $i^{d_j}$  denotes the time instant of fault detection,  $d_j$  is the detection-index and the fault is said to have occurred before the time instant  $i^{d_j}$ , and more specifically  $i^{d_{j-1}} \leq i^{f_j} \leq i^{d_j}$ .

This criterion should be used in conjunction with

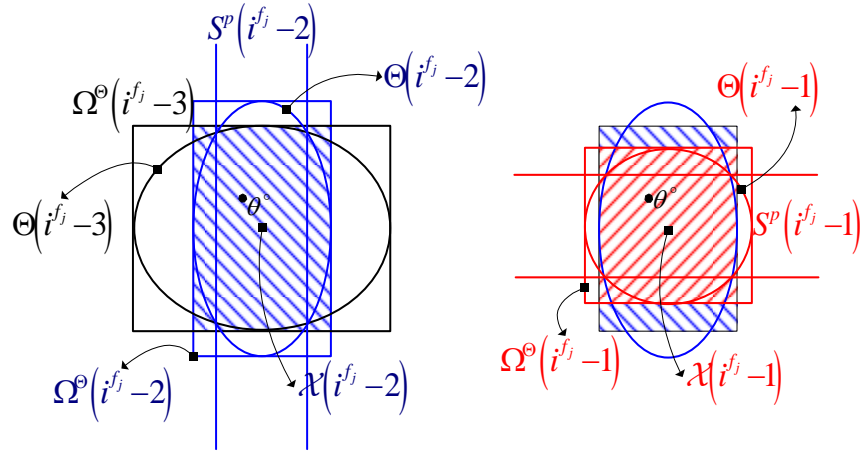
$$\Theta(i^{d_j} - 1) \cap S(i^{d_j}) = \emptyset. \quad (3.71)$$

Figure 3.7 indicates the application of the OVE-method over a four sample time-window  $i \in \{i^{f_j} - 3, \dots, i^{f_j} - 1\}$ . The computed ellipsoids, orthotopes and hyperstrips in ascending chronological order are shown with black, blue and red color-lines respectively. The intersections  $\mathcal{X}(i)$  are shown by the similarly colored hashed-areas.

$\mathcal{X}(i^{f_j} - 1)$  and the  $\Theta(i^{f_j} - 1)$  sets are also presented in Fig. 3.8, from which it is apparent that neither set contains the other. When the fault occurs at  $i^{d_j} = i^{f_j}$ , the OVE-method cannot capture it, since  $\Theta(i^{f_j}) \neq \emptyset$ , in contrast with the FD-criterion 2 in which  $\mathcal{X}(i^{f_j} - 1) \cap \Omega^\Theta(i^{f_j}) = \emptyset$ .

#### 3.5.2 Fault Diagnosis Procedure

The fault diagnosis procedure presented in Section 3.4 is properly customized assuming a nominal parameter vector that is time invariant after each fault occurrence.



**Figure 3.7:** Graphical representation of the computation of the intersection of support orthotopes ( $n = 2$ ).

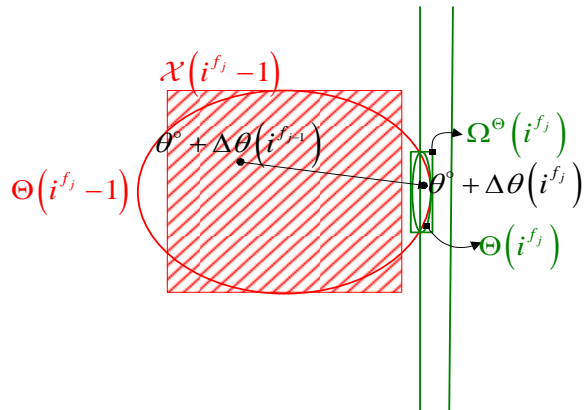


**Figure 3.8:** Activation of the FD-criterion using orthotopes with  $i^{d_j} = i^{f_j}$  ( $n = 2$ ).

### 3. FAULT DETECTION AND DIAGNOSIS

---

**Resetting Procedure** When a fault is detected at the time instant  $i^{d_j}$ , the resetting of the parametric set ( $\mathcal{Z}(i^{d_j-1}) \rightarrow \mathcal{Z}^r(i^{d_j-1})$ ) and the data hyperspace ( $S(i^{d_j-1}) \rightarrow S^r(i^{d_j-1})$ ) is performed so as

$$\left. \begin{array}{l} \theta^\circ + \Delta\theta(i^{f_j}) \in \mathcal{Z}^r(i^{d_j}) \\ \text{and} \\ \theta^\circ + \Delta\theta(i^{f_j}) \in S^r(i^{d_j}) \end{array} \right\} \Rightarrow \mathcal{Z}^r(i^{d_j}) \cap S^r(i^{d_j}) \neq \emptyset. \quad (3.72)$$

**A. Orthotope-based Resetting Procedure** In case that the FDD procedure is based on orthotopic SMI, the resetting of  $\Omega(i^{d_j-1})$  is accomplished according to the following theorem.

**Theorem 3.5.1** If  $\theta^\circ + \Delta\theta(i^{f_{j-1}}) \in \Omega(i^{d_j-1})$ , then  $\theta^\circ + \Delta\theta(i^{f_j}) \in \Omega^r(i^{d_j-1})$ , where

$$\Omega^r(i^{d_j-1}) = \left\{ \theta : \begin{bmatrix} \theta_{\Omega_1}^{r-}(i^{d_j-1}) \\ \vdots \\ \theta_{\Omega_n}^{r-}(i^{d_j-1}) \end{bmatrix} \preceq \theta \preceq \begin{bmatrix} \theta_{\Omega_1}^{r+}(i^{d_j-1}) \\ \vdots \\ \theta_{\Omega_n}^{r+}(i^{d_j-1}) \end{bmatrix} \right\} \quad (3.73)$$

with

$$\theta_{\Omega_u}^{r-}(i^{d_j-1}) = \theta_{\Omega_u}^-(i^{d_j-1}) - 2\tilde{\gamma}_u^{\max}, \quad (3.74)$$

$$\theta_{\Omega_u}^{r+}(i^{d_j-1}) = \theta_{\Omega_u}^+(i^{d_j-1}) + 2\tilde{\gamma}_u^{\max}. \quad (3.75)$$

**Proof** From (3.60)-(3.62), it yields that  $\Delta\theta_u(i^{f_j}), -\Delta\theta_u(i^{f_{j-1}}) \in [-\tilde{\gamma}_u^{\max}, \tilde{\gamma}_u^{\max}]$ ,  $\forall u$ , implying that  $\Delta\theta_u(i^{f_j}) - \Delta\theta_u(i^{f_{j-1}}) \in [-2\tilde{\gamma}_u^{\max}, 2\tilde{\gamma}_u^{\max}]$ ,  $\forall u$ . Subsequently,  $\Delta\theta(i^{f_j}) - \Delta\theta(i^{f_{j-1}})$  resides within an orthotope defined as:

$$\Omega_{\Delta\theta} = \left\{ \theta : \begin{bmatrix} -2\tilde{\gamma}_1^{\max} \\ \vdots \\ -2\tilde{\gamma}_n^{\max} \end{bmatrix} \preceq \theta \preceq \begin{bmatrix} 2\tilde{\gamma}_1^{\max} \\ \vdots \\ 2\tilde{\gamma}_n^{\max} \end{bmatrix} \right\}. \quad (3.76)$$

Assuming that  $\theta^\circ + \Delta\theta(i^{f_{j-1}}) \in \Omega(i^{d_j-1})$ , and taking into account that  $\theta^\circ + \Delta\theta(i^{f_j}) = \theta^\circ + \Delta\theta(i^{f_{j-1}}) + (\Delta\theta(i^{f_j}) - \Delta\theta(i^{f_{j-1}}))$  it yields that  $\theta^\circ + \Delta\theta(i^{f_j}) \in \Omega^r(i^{d_j-1})$  with:

$$\Omega^r(i^{d_j-1}) = \arg_{\Omega} \left\{ \Omega : \Omega = \Omega(i^{d_j-1}) \oplus \Omega_{\Delta\theta} \right\} \quad (3.77)$$

whose vertices' coordinates are defined through (3.74)-(3.75).



**B. Ellipsoid-based Resetting Procedure** The resetting procedure when the FDD procedure relies on the ellipsoidal SMI is realized according to the following theorem.

**Theorem 3.5.2** If  $\theta^\circ + \Delta\theta(i^{f_{j-1}}) \in \Theta(i^{d_j - 1})$ , then  $\theta^\circ + \Delta\theta(i^{f_j}) \in \Theta^r(i^{d_j - 1})$ , with the centroid and the shape matrix of  $\Theta^r(i^{d_j - 1})$  given as:

$$\theta_r^c(i^{d_j - 1}) = \theta^c(i^{d_j - 1}), \quad (3.78)$$

$$P^r(i^{d_j - 1}) = U(i^{d_j - 1})\Sigma^r(i^{d_j - 1})U^T(i^{d_j - 1}), \quad (3.79)$$

$$\Sigma^r(i^{d_j - 1}) = \Sigma(i^{d_j - 1}) + 4\tilde{\gamma}\Sigma(i^{d_j - 1})^{1/2} + 4\tilde{\gamma}^2I, \quad (3.80)$$

$$P(i^{d_j - 1}) = U(i^{d_j - 1})\Sigma(i^{d_j - 1})U^T(i^{d_j - 1}). \quad (3.81)$$

**Proof** The worst case scenario amounts to the location of  $\theta^\circ(i^{d_j - 1})$  almost on the closure of  $\Theta(\theta^c(i^{d_j - 1}), P(i^{d_j - 1}))$ . The closure of this ellipsoid should be enlarged by the maximum possible parameter deviation given as

$$\begin{aligned} \|\Delta\theta(i^{f_j})\| &\leq \sqrt{\sum_{u=1}^n |\tilde{\gamma}_u^{\max}|} = \tilde{\gamma}, \quad \forall i^{f_j}, \\ \|\Delta\theta(i^{f_j}) - \Delta\theta(i^{f_{j-1}})\| &\leq \|\Delta\theta(i^{f_j})\| + \|\Delta\theta(i^{f_{j-1}})\| \leq 2\tilde{\gamma}. \end{aligned}$$

Based on the singular value decomposition of the shape matrix  $P(i^{d_j - 1}) = U(i^{d_j - 1})\Sigma(i^{d_j - 1})U^T(i^{d_j - 1})$ , the  $\Sigma(i^{d_j - 1})$ -diagonal matrix contains the squared elements of the semiaxes' lengths. Let these elements be  $\lambda_u$ ,  $u = 1, \dots, n$ ; then to ensure the presence of  $\theta^\circ + \Delta\theta(i^{f_j})$  inside an ellipsoid  $\Theta^r(i^{d_j - 1})$  with the same centroid as in  $\Theta(i^{d_j - 1})$ , these elements must be set to  $(\sqrt{\lambda_u} + 2\tilde{\gamma})^2 = \lambda_u + 4\tilde{\gamma}\sqrt{\lambda_u} + 4\tilde{\gamma}^2$ . In a more compact form,  $\Sigma^r(i^{d_j - 1}) = \Sigma(i^{d_j - 1}) + 4\tilde{\gamma}\Sigma(i^{d_j - 1})^{1/2} + 4\tilde{\gamma}^2I$ .

An alternative procedure for calculating the resetting ellipsoid  $\Theta^r(i^{d_j - 1})$  based on the intersection of the support orthotopes is provided in the next theorem [89].

**Theorem 3.5.3** If  $\theta^\circ + \Delta\theta(i^{f_{j-1}})$  resides within the sets  $\mathcal{X}(i^{d_j - 1})$  and  $\Theta(i^{d_j - 1})$ , then  $\theta^\circ + \Delta\theta(i^{f_j})$  will reside within the sets  $\mathcal{X}^r(i^{d_j - 1})$  and  $\Theta^r(i^{d_j - 1})$ , where

$$\mathcal{X}^r(i^{d_j - 1}) = \left\{ \theta : \begin{bmatrix} \theta_{x_1}^{r-}(i^{d_j - 1}) \\ \vdots \\ \theta_{x_n}^{r-}(i^{d_j - 1}) \end{bmatrix} \preceq \theta \preceq \begin{bmatrix} \theta_{x_1}^{r+}(i^{d_j - 1}) \\ \vdots \\ \theta_{x_n}^{r+}(i^{d_j - 1}) \end{bmatrix} \right\} \quad (3.82)$$

with

$$\theta_{x_u}^{r-}(i^{d_j - 1}) = \theta_{x_u}^-(i^{d_j - 1}) - 2\tilde{\gamma}_u^{\max}, \quad (3.83)$$

$$\theta_{x_u}^{r+}(i^{d_j - 1}) = \theta_{x_u}^+(i^{d_j - 1}) + 2\tilde{\gamma}_u^{\max} \quad (3.84)$$

### 3. FAULT DETECTION AND DIAGNOSIS

---

and

$$\Theta^r(i^{d_j} - 1) = \arg \left[ \min_{\Theta} \left\{ \text{vol}(\Theta) : \Theta \supset \mathcal{X}^r(i^{d_j} - 1) \right\} \right]. \quad (3.85)$$

**Proof** It is reminded that  $\Delta\theta(i^{f_j}) - \Delta\theta(i^{f_{j-1}}) \in \Omega_{\Delta\theta}$  with  $\Omega_{\Delta\theta}$  given in (3.76). Assuming that  $\theta^\circ + \Delta\theta(i^{f_{j-1}}) \in \mathcal{X}(i^{d_j} - 1)$ , then  $\theta^\circ + \Delta\theta(i^{f_j}) = \theta^\circ + \Delta\theta(i^{f_{j-1}}) + (\Delta\theta(i^{f_j}) - \Delta\theta(i^{f_{j-1}})) \in \mathcal{X}^r(i^{d_j} - 1)$  with:

$$\mathcal{X}^r(i^{d_j} - 1) = \arg \left\{ \mathcal{X} : \mathcal{X} = \mathcal{X}(i^{d_j} - 1) \oplus \Omega_{\Delta\theta} \right\} \quad (3.86)$$

whose vertices' coordinates are defined through (3.83)-(3.84). The ellipsoid  $\Theta^r(i^{d_j} - 1)$  is the Löwner-John ellipsoid of  $\mathcal{X}^r(i^{d_j} - 1)$ , whose centroid  $\theta_r^c(i^{d_j} - 1)$  and shape matrix  $P^r(i^{d_j} - 1)$  are the solutions of the optimization problem [90]:

$$\begin{aligned} \min & \quad \log(\det(Q^{-1})) \\ \text{s.t.} & \quad \|Q(V_{\mathcal{X}^r}^p(i^{d_j} - 1) - \theta_r^c(i^{d_j} - 1))\| \leq 1, \end{aligned} \quad (3.87)$$

$\forall p = 0, \dots, 2^n - 1$ , where  $Q \in \mathbb{R}^{n \times n} \succ 0$ ,  $V_{\mathcal{X}^r}^p(i^{d_j} - 1)$  corresponds to the coordinates of the  $p$ th vertex of  $\mathcal{X}^r(i^{d_j} - 1)$  and  $P^r(i^{d_j} - 1) = (Q^T Q)^{-1}$ .

**C. Data-hyperstrip Resetting Procedure** The data-hyperspace is reset following the procedure described in Section 3.4. The only modification that should be made for the time invariant parameters case is that the parameter bounds arisen from the projection of  $\Omega^r(i^{d_j} - 1)$ ,  $(\Theta^r(i^{d_j} - 1), \mathcal{X}^r(i^{d_j} - 1))$  are used for the computation of  $S_r^p(i^{d_j})$  or  $S_r^{np}(i^{d_j})$ .

An example of the resetting procedure of the intersection of support orthotopes and the data-hyperstrip is presented in Fig. 3.9.

**Remark 3.5.4** In case that the noise-errors are induced as an equation error in the jump linearly parametrizable model, as described in Section 2.6.2, the data-hyperstrip resetting procedure is omitted.

After the orthotope-based resetting procedure, the computation of  $\Omega(i^{d_j})$  is realized according to:

$$\Omega(i^{d_j}) = \arg \left\{ \Omega : \Omega \supseteq \left( \Omega^r(i^{d_j} - 1) \cap S^r(i^{d_j}) \right) \right\} \quad (3.88)$$

and the orthotopic-SMI continues its operation, as described in Section 2.5.1. Similarly, the ellipsoid-based resetting procedure is followed by the computation of  $\Theta(i^{d_j})$  and  $\mathcal{X}(i^{d_j})$  as

$$\Theta(i^{d_j}) = \arg \left[ \min_{\Theta} \left\{ \text{vol}(\Theta) : \Theta \supset \left[ \Theta^r(i^{d_j} - 1) \cap S^r(i^{d_j}) \right] \right\} \right], \quad (3.89)$$

$$\mathcal{X}(i^{d_j}) = \Omega^\Theta(i^{d_j}), \quad (3.90)$$

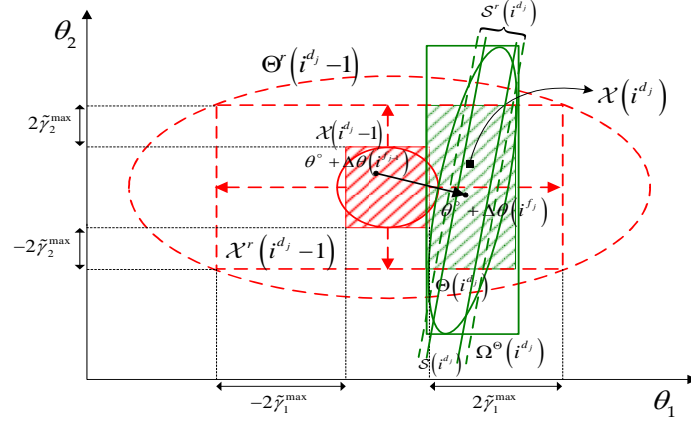


**Figure 3.9:** Resetting procedure based on the intersection of support orthotopes ( $n = 2$ )

while in the resetting procedure based on the intersection of support orthotopes the ellipsoid  $\Theta(i^{d_j})$  is computed via (3.89) and

$$\mathcal{X}(i^{d_j}) = \mathcal{X}^r(i^{d_j-1}) \cap \Omega^\Theta(i^{d_j}), \quad (3.91)$$

For  $i^{d_j} < i < i^{d_{j+1}}$ , the ellipsoid SMI procedure continues its operation according to Section 2.5.2.

### 3.5.2.1 Fault Isolation Procedure

The fault isolation and identification procedure is realized taking into account that [88]:

- $\theta^\circ \in \mathcal{X}(i^{d_1-1}) \cap \Omega(i^{d_1-1})$ ,
- $\theta^\circ + \Delta\theta(i^{f_j}) \in \mathcal{X}(i^{d_j+i}) \cap \Omega(i^{d_j+i})$ ,  $\forall i \in [0, i^{d_{j+1}} - i^{d_j}]$
- $\mathcal{X}(i-1) \subseteq \mathcal{X}(i)$ ,  $\Omega(i-1) \subseteq \Omega(i) \forall i$ .

**Lemma 3.5.5** A fault can be isolated for the  $u$ th component of the parameter vector at the earliest time instant  $i^{u*}$  for which

$$\mathcal{Z}_u(i^{d_1-1}) \cap \mathcal{Z}_u(i^{u*}) = \emptyset, \quad (i^{u*} \geq i^{d_j}), \quad (3.92)$$

where  $\mathcal{Z}_u(i) = \mathcal{X}_u(i)$  for the ellipsoidal SMI-based FDD and  $\mathcal{Z}_u(i) = \Omega_u(i)$  for the orthotopic SMI-based FDD.

**Proof** Since  $\mathcal{Z}_u(i^{u*+i}) \subseteq \mathcal{Z}_u(i^{u*})$ ,  $i^{u*+i} < i^{d_{j+1}}$  then  $\mathcal{Z}_u(i^{d_1-1}) \cap \mathcal{Z}_u(i) = \emptyset \forall i \in [i^{u*}, \dots, i^{d_{j+1}}]$ , and the  $u$ th component of the parameter vector is defined as faulty.

### 3. FAULT DETECTION AND DIAGNOSIS

**Lemma 3.5.6** The  $u$ th component of the parameter vector is termed non-faulty at the earliest time instant  $i^{u*}$  for which

$$\mathcal{Z}_u(i^{d_1} - 1) \cap \mathcal{Z}_u(i^{u*}) = \mathcal{Z}_u(i^{u*}), \quad (i^{u*} \geq i^{d_j}), \quad (3.93)$$

where  $\mathcal{Z}_u(i) = \mathcal{X}_u(i)$  for the ellipsoidal SMI-based FDD and  $\mathcal{Z}_u(i) = \Omega_u(i)$  for the orthotopic SMI-based FDD.

**Proof** Since  $\mathcal{Z}_u(i^{u*} + i) \subseteq \mathcal{Z}_u(i^{u*})$ ,  $i^{u*} + i < i^{d_{j+1}}$  then  $\mathcal{Z}_u(i^{d_1} - 1) \cap \mathcal{Z}_u(i) = \mathcal{Z}_u(i) \quad \forall i \in [i^{u*}, \dots, i^{d_{j+1}}]$ , and the the  $u$ th component of the parameter vector is defined as a non-faulty one.

If there is no time instant  $i \in [i^{d_j}, \dots, i^{d_{j+1}}]$  for which Equations (3.92), or (3.93) are not valid, then there can be no inference for the status of the  $u$ th component of the parameter vector.

An example, clarifying the fault isolation procedure with  $u = 2$  is presented in Figure 3.10, where for the left, middle, and right case, the status of the  $\theta_2$  component is termed as non-faulty, faulty, and unspecified, respectively. In all cases, the  $\theta_1$  component is termed as a faulty one.

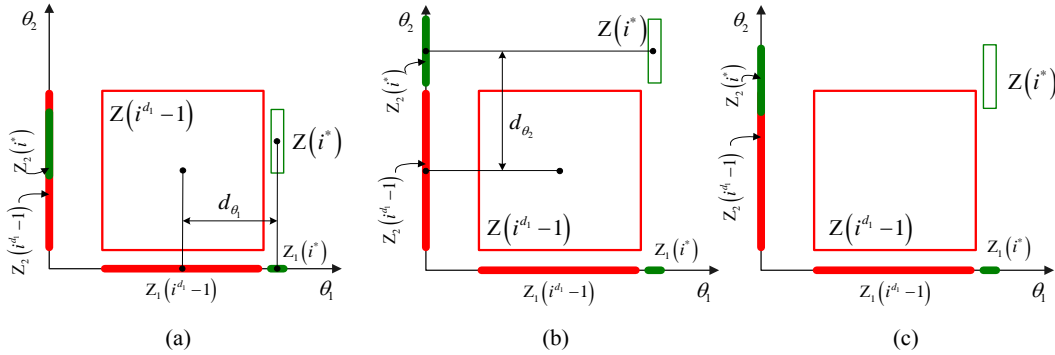


Figure 3.10: Fault isolation example ( $n = 2$ )

#### 3.5.2.2 Fault Identification Procedure

After the fault isolation event in which the ‘faulty’  $u^*$ th components of the parameter vector were isolated as the ones for which (3.92) is satisfied, the most likely size of these faults can be estimated by the distance of the centers of the sets  $\mathcal{Z}_u(i^{d_1} - 1)$  and  $\mathcal{Z}_u(i^{u*} + i)$  with  $0 \leq i < i^{d_{j+1}} - i^{u*}$ . In this case, using (3.67), the estimation of fault is:

$$d_{\theta_u}(i) = \theta_{z_u^c}^c(i^{u*} + i) - \theta_{z_u^c}^c(i^{d_1} - 1), \quad (3.94)$$

where  $\theta_{z_u}^c(i) = \theta_{x_u}^c(i)$  in the ellipsoidal SMI-based FDD and  $\theta_{z_u}^c(i) = \theta_{\Omega_u}^c(i)$  for the orthotopic SMI-based FDD.  $\theta_{x_u}^c(i)$ ,  $\theta_{\Omega_u}^c(i)$  are computed through (3.67) and 2.12), respectively.

## 3.6 Fault Detection and Diagnosis Issues

This section provides a discussion about the detectability of the faults, the possibility of a more accurate estimation of the time of fault occurrence and the sensitivity of the algorithm in relation to the SMI and FDD assumptions. For sake of simplicity, the discussion is realized taking into account time invariant parameters, but it can be extended to the time-varying parameter case.

### 3.6.1 Undetected Faults

We should note that a fault may never be observed despite its occurrence. This depends on whether  $\theta^\circ + \Delta\theta(i^{f_j}) \in \mathcal{Z}(i^{f_j} + \ell)$ ,  $\ell \in [0, \dots, i^{f_{j+1}} - i^{f_j}]$ , where  $\mathcal{Z}(i)$  corresponds to either an orthotope or an ellipsoid.

#### 3.6.1.1 Undetected faults in the Orthotope-based Fault Detection Procedure

**Lemma 3.6.1** A sufficient condition for  $\theta^\circ + \Delta\theta(i^{f_j}) \in \Omega(i^{f_j} + \ell)$ ,  $\ell \in [0, \dots, i^{f_{j+1}} - i^{f_j}]$  is  $\theta^\circ + \Delta\theta(i^{f_j}) \in \Omega(i^{f_j} - 1)$  [91].

**Proof** At the time instant  $i^{f_j}$ ,  $\theta^\circ + \Delta\theta(i^{f_j}) \in S(i^{f_j})$ . If  $\theta^\circ + \Delta\theta(i^{f_j}) \in \Omega(i^{f_j} - 1)$ , then  $\Omega(i^{f_j} - 1) \cap S(i^{f_j}) \neq \emptyset$  and the fault is not detected. Consequently,  $\theta^\circ + \Delta\theta(i^{f_j}) \in \Omega(i^{f_j})$ , with  $\Omega(i^{f_j}) \supseteq \Omega(i^{f_j} - 1) \cap S(i^{f_j})$ . This situation will be repeated in future time, resulting in  $\theta^\circ + \Delta\theta(i^{f_j}) \in \Omega(i^{f_j} + \ell)$  with  $\Omega(i^{f_j} + \ell) \supseteq \Omega(i^{f_j} + \ell - 1) \cap S(i^{f_j} + \ell)$  for  $\ell \in [0, \dots, i^{f_{j+1}} - i^{f_j}]$ .

#### 3.6.1.2 Undetected faults in Ellipsoid-based Fault Detection Procedure

In the ellipsoid-based FDD procedure, it is possible that  $\theta^\circ + \Delta\theta(i^{f_j}) \in \Theta(i^{f_j} + \ell)$ ,  $\ell \in [0, \dots, i^{f_{j+1}} - i^{f_j}]$ , without  $\theta^\circ + \Delta\theta(i^{f_j}) \in \Theta(i^{f_j} - 1)$ , as shown in Fig. 3.11.

**Theorem 3.6.2** A sufficient condition for  $\theta^\circ + \Delta\theta(i^{f_j}) \in \Theta(i^{f_j})$  (undetected case) is

$$\begin{aligned} \theta^\circ + \Delta\theta(i^{f_{j-1}}) &\in \Theta(i^{f_j} - 1), \text{ and} \\ \|\Delta\theta(i^{f_j}) - \Delta\theta(i^{f_{j-1}})\| &\leq \frac{-\alpha_2 + \sqrt{\alpha_2^2 - 4\alpha_1\alpha_3}}{2\alpha_1}, \text{ and} \\ \alpha_3 &< 0, \end{aligned}$$

### 3. FAULT DETECTION AND DIAGNOSIS

---

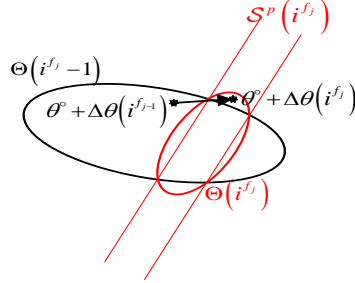


Figure 3.11: Undetected fault case ( $n = 2$ ).

where  $\alpha_2 = 2 \left| \frac{\sigma(i^{f_j}) - \delta(i^{f_j})}{\sigma(i^{f_j}) \sqrt{G(i^{f_j})}} \left( \frac{\phi^T(i^{f_j}) \tilde{\theta}_1}{\sqrt{G(i^{f_j})}} \right) + \frac{\delta(i^{f_j}) \tau(i^{f_j})}{\sigma(i^{f_j}) \sqrt{G(i^{f_j})}} \right| \|\phi(i^{f_j})\| + 2 \frac{\sqrt{\lambda_{\max}[P(i^{f_j-1})]}}{\lambda_{\min}[P(i^{f_j-1})]}$ ,

$\alpha_3 = 1 + \frac{\delta(i^{f_j})}{\sigma(i^{f_j})} \left( \frac{\phi(i^{f_j})^T \tilde{\theta}_1}{\sqrt{G(i^{f_j})}} - \tau(i^{f_j}) \right)^2 - \delta(i^{f_j})$ ,  $\tilde{\theta}_1 = \theta^\circ + \Delta\theta(i^{f_{j-1}}) - \theta_c(i^{f_j-1})$ , and  $\alpha_1 = \frac{\delta(i^{f_j})}{\lambda_{\min}[P(i^{f_j})]}$ .

**Proof** See Appendix A.3

#### 3.6.2 Backward-in-time fault detection procedure

It should be noted that the instant of detection  $i^{d_j}$  can be different than the time of occurrence  $i^{f_j}$  of the fault. This may lead into a possible successive incorrect time instant of fault detection  $i^{d_{j+1}}$ . If  $i^{d_{j+1}} - i^{d_j} < L$ , then our assumption of a jump system for which the parameter vector remains constant for at least  $L$ -samples after the occurrence of a fault contradicts our findings. In this case, the instant  $i^{d_j}$  needs to be revised and a ‘backward-in-time fault detection’ algorithm is sought.

##### 3.6.2.1 Orthotope-based Backward-in-Time Fault Detection

The following scenario is provided so as to justify the previous allegation. Consider that  $\theta^\circ + \Delta\theta(i^{f_{j-1}}) \in \Omega(i^{f_{j-1}})$  (black color) and a fault occurs at the time instant  $i^{f_j}$  such that  $\Delta\theta(i^{f_j}) - \Delta\theta(i^{f_{j-1}}) = [d_1, 0]^T$ , (Fig.(3.12)) and let  $L = 3$  [91]. Although there is a deviation of parameter vector that leads to the placement of the new parameter vector  $\theta^\circ + \Delta\theta(i^{f_j})$  outside  $\Omega(i^{f_{j-1}})$ , the measurement data generate such a hypersector  $S^{np}(i^{f_j})$  (red color) that intersects with  $\Omega(i^{f_{j-1}})$ . Hence, the fault is not detected and a new orthotope  $\Omega(i^{f_j})$  (red color) is computed, which contains neither  $\theta^\circ + \Delta\theta(i^{f_j})$  nor  $\theta^\circ + \Delta\theta(i^{f_{j-1}})$ . The fault is detected at the time instant  $i^{d_j} = i^{f_j} + 1$ , since  $S^{np}(i^{f_j+1}) \cap \Omega(i^{f_j}) \neq \emptyset$ , where  $S^{np}(i^{f_j+1})$  is green colored. The algorithm continues with the computation of the resetting orthotope  $\Omega^r(i^{f_j})$  (red dashed), using Theorem (3.5.1), and in the sequel with the computation of  $\Omega(i^{f_j+1})$ . At the next

time instant, the generated data-hypersector  $S^{np}(i^{f_j} + 2)$  (blue color) does not intersect with  $\Omega(i^{f_j} + 1)$  and a fault is detected again at  $i^{d_{j+1}} = i^{f_j} + 2 < i^{f_j} + 1 + L = i^{d_j} + L$ . In this case, our assumptions that the fault occurred at  $i^{d_j} = i^{f_j} + 1$  is incorrect. To cope with this situation, the ‘backward-in-time fault detection’ modification is proposed.

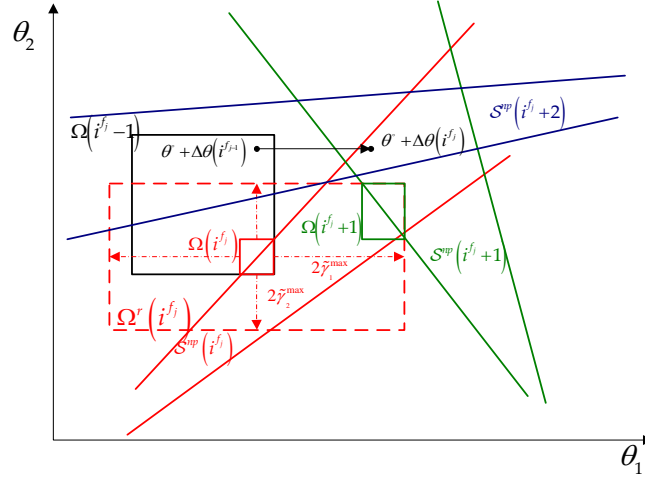


**Figure 3.12:** Incorrect time instant of fault detection in case of orthotopic FDD ( $n = 2$ ).

Rather than assuming that the detection of the fault is at the time  $i^{d_j}$ , we roll-back the detection instant at  $i^{d_{j^*}} = i^{d_j} - 1$  and proceed by substituting  $\Omega^r(i^{d_{j^*}} - 1)$  in place of  $\Omega(i^{d_{j^*}} - 1)$ . The fault detection algorithm is repeated, computing the orthotopes for  $\{i^{d_{j^*}}, \dots, i^{d_{j+1}}\}$ , aiming at a non-empty intersection between  $S^{np}(i^{d_{j+1}})$  and  $\Omega(i^{d_{j+1}} - 1)$ . If this roll-back fails (empty intersection), we continue in a recursive manner with  $i^{d_{j^*}} = \{i^{d_j} - 2, \dots, i^{d_j} - L\}$ , until the previous issue cannot be encountered. Figure (3.13) shows the application of the ‘backward-in-time’ procedure in the previous fault scenario. As it can be observed, rolling-back to  $i^{d_{j^*}} = i^{d_j} - 1$  was enough, so as  $S(i^{d_{j+1}}) \cap \Omega(i^{d_{j+1}} - 1) \neq \emptyset$ .

### 3.6.2.2 Ellipsoid-based Backward-in-Time Fault Detection

In the case of the ellipsoid based FDD procedure, the need for applying the backward-in-time procedure is exemplified in the following scenario. Assume that  $\Theta(i^{f_j} - 1) = \Theta(0, RI_2)$  (circle), where  $R$  is the circle’s radius and  $\theta^\circ + \Delta\theta(i^{f_j} - 1)$  located on the perimeter of the circle. Let the fault  $\theta^\circ + \Delta\theta(i^{f_j})$  be located at a distance  $\|\Delta\theta(i^{f_j}) - \Delta\theta(i^{f_j} - 1)\| = 2\tilde{\gamma} - \varepsilon$  (where  $\varepsilon$  is a positive constant), as shown in Fig. 3.14. In addition, assume a regression vector  $\phi(i^{f_j})$  and a model output  $y(i^{f_j})$ , such that the  $S^p(i^{f_j}) \cap \Theta(i^{f_j} - 1)$  corresponds to a single point. In this case,  $\Theta(i^{f_j})$  corresponds to this point and the fault is not detected. Assume that at time instant  $i^{f_j} + 1$  the measurement data leads to  $S^p(i^{f_j} + 1) \cap \Theta(i^{f_j}) = \emptyset$ , then the resetting ellipsoid  $\Theta^r(i^{f_j})$  (circle centered at the intersection point and radius being equal to  $2\tilde{\gamma}$ ) will not capture

### 3. FAULT DETECTION AND DIAGNOSIS

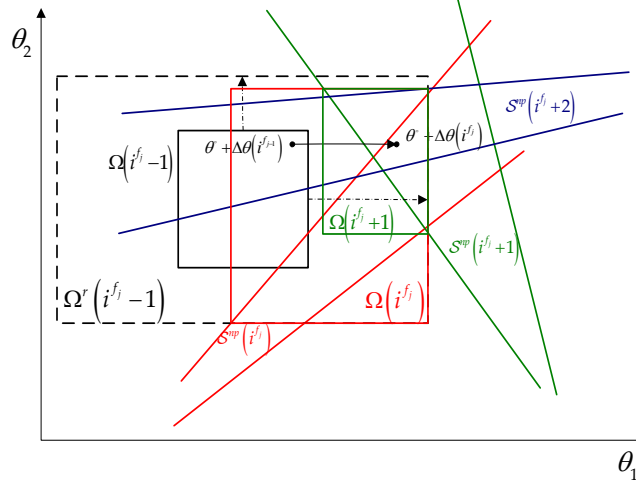


**Figure 3.13:** ‘Backward-in-time’ fault detection procedure in case of orthotopic FDD ( $n = 2$ ).

the fault for  $2\tilde{\gamma} + R - \sqrt{4\tilde{\gamma}^2 + R^2} < \varepsilon < 2\tilde{\gamma} + R + \sqrt{4\tilde{\gamma}^2 + R^2}$ . In this case (depending on the  $S^p(i^{f_j+1})$ ), the  $S^p(i^{f_j+1}) \cap \Theta^r(i^{f_j}) = \emptyset$  and our assumptions that the fault occurred at  $i^{d_j} = i^{f_j+1}$  is not valid. To cope with this situation, the ‘backward-in-time fault detection’ modification is proposed.

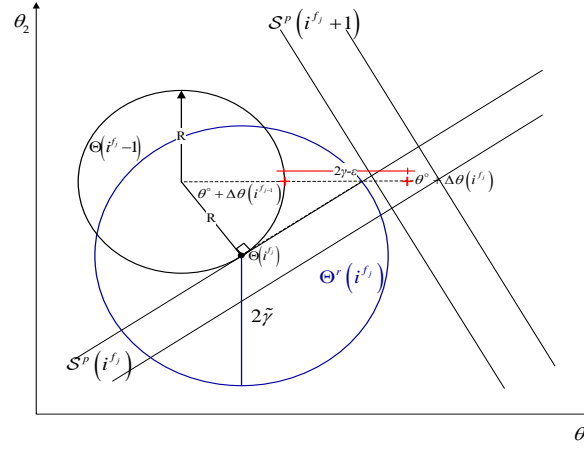


**Figure 3.14:** Incorrect time instant of fault detection in case of ellipsoidal FDD ( $n = 2$ )

Rather than assuming that the detection of the fault is at the time  $i^{d_j}$ , we roll-back the detection instant at  $i^{d_j} - 1$  and restart the fault detection algorithm by substituting  $\Theta^r(i^{d_j} - 2)$  in place of  $\Theta(i^{d_j} - 2)$  and checking its intersection with the  $S^p(i^{d_j} - 1)$ . If this roll-back fails, we continue in a recursive manner at  $i^{d_j} - 2, \dots, i^{d_j} - L$ , until the previous issue cannot be encountered.



It has to be mentioned that the goal of the ‘backward-in-time’ procedure is the better estimation of the time of fault occurrence and the guaranteed capturing of the ‘new’ parameter vector  $\theta^\circ + \Delta\theta(i^{f_i})$  within the computed orthotopes or ellipsoids after the fault occurrence. The latter issue is proven to be necessary for the correct fault isolation and identification mechanisms. The backward-in-time fault detection is provided in algorithmic form in Appendix B.2.

#### Fault Detection Example

The following ‘fault detection case’ exemplifies the detection and update mechanisms. Consider  $y(i) = [\phi_1(i), \phi_2(i)] [\theta_1^\circ, \theta_2^\circ]^T + e(i)$  where the corrupting noise  $|e(i)| \leq 1.3$  and the nominal parameter vector,  $\theta^\circ = [-0.35, 0.5]^T$ . The maximum sustainable variation is equal to  $\tilde{\gamma} = 0.825$ , the dwell time  $L = 3$ , and at the fifth time instant  $\theta^\circ + \Delta\theta(0)$  jumps to  $\theta^\circ + \Delta\theta(5) = [-2, 0.5]^T$ . The OVE algorithm is initialized using  $P(1) = I_2$ , and  $\theta^c(1) = [0, 0]^T$ . Assume the following output and regression vector measurements in an ascending chronological order:

$i$	1	2	3	4	5	6	7	8	9	10
$y(i)$	0.5	1	0.73	-0.31	-7.45	-0.89	-4.225	-5.4	-19	-22.78
$\phi_1(i)$	1.5	2	0.2	0.6	2	0.8	1.6	2.5	8	10
$\phi_2(i)$	0	1	0.5	0.9	-5	0.12	-4.55	1.7	-4	-3

In the ensuing Figure 3.15, where each graph is marked by its  $i$ th sample instant, the suggested algorithm is exemplified in order to highlight the issues of fault detection. The computed ellipsoid at the  $(i-1), [i]$  instant is shown in (black)[grey] color. The centroids of these ellipsoids correspond to the (black)[grey] drawn dots. The nominal parameter vector  $\theta^\circ$  ( $\theta^\circ + \Delta\theta(5)$ ) is shown by the black ‘+’ (‘\*’) symbol in the noted plots. The hyperplanes (lines in  $\mathbb{R}^2$ )  $h_1(i)$  and  $h_2(i)$  are shown with grey lines; the hyperstrip  $S^p(i)$  corresponds to the space bounded by these lines.

During the time instants  $i \in \{2, 3, 4\}$  the hyperstrip  $S^p(i)$  intersects the ellipsoid  $\Theta(i-1)$ . At the fifth sample, despite the jump of parameter-vector,  $\Theta(4) \cap S^p(5) \neq \emptyset$  and the fault is not captured. The OVE-algorithm computes  $\Theta(5)$  (see zoomed-in portion at bottom-left part of this plot). Similarly,  $\Theta(5) \cap S^p(6) = \Theta(5) \neq \emptyset$  and  $\Theta(6) \cap S^p(7) \neq \emptyset$ . At the eighth sample, the fault is captured since  $\Theta(7) \cap S^p(8) = \emptyset$  ( $\Theta(7)$  is the ‘tiny’-black ellipsoid). In this case, the resetting (dashed black) ellipsoid is formed for which  $\Theta^r(7) \cap S^p(8) \neq \emptyset$ . The  $i^{d_1} = 8$  time-instant is marked as the possible fault detection instant and differs from the  $i^{f_1} = 5$  fault occurrence instant. The OVE-algorithm continues its normal execution at the ninth instant since  $\Theta(8) \cap S^p(9) \neq \emptyset$  and at the tenth sample another fault is detected ( $i^{d_2} = 10$ ) since  $\Theta(9) \cap S^p(10) = \emptyset$ . The time separation between the adjacent faults is  $i^{d_2} - i^{d_1} = 2$ .

Since  $i^{d_2} - i^{d_1} < L$  the FDD algorithm rather than assuming that the first detection of the fault is at  $i^{d_1} = 8$ , it will backtrack-in-time and will assume that the fault occurred at  $i^{d_1} = 7$ . This is highlighted in Figure 3.16, where at the seventh time

### 3. FAULT DETECTION AND DIAGNOSIS

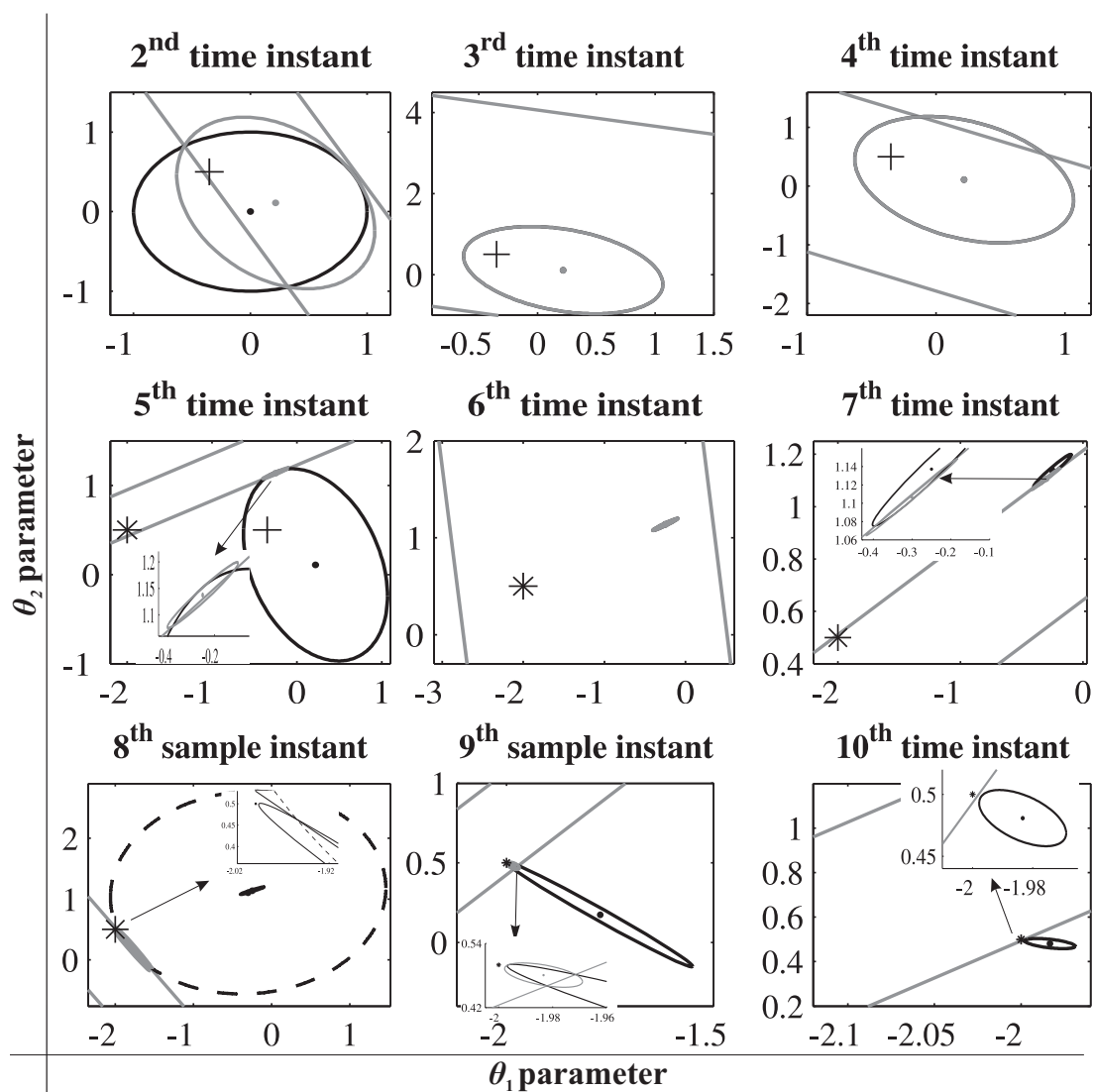


Figure 3.15: Fault detection example ( $n = 2$ ).

instant  $\Theta(6)$  ('tiny' black ellipsoid) is resetting  $\Theta(6) \leftarrow \Theta^r(6)$  and the OVE-algorithm continues its normal operation until the tenth instant. It should be noted that although  $i^{d1} = 7 \neq i^{f1} = 5$ , the varied parameter vector  $\theta^\circ + \Delta\theta(5)$  is captured by  $\Theta(10)$ , computed during the backward-in-time procedure.

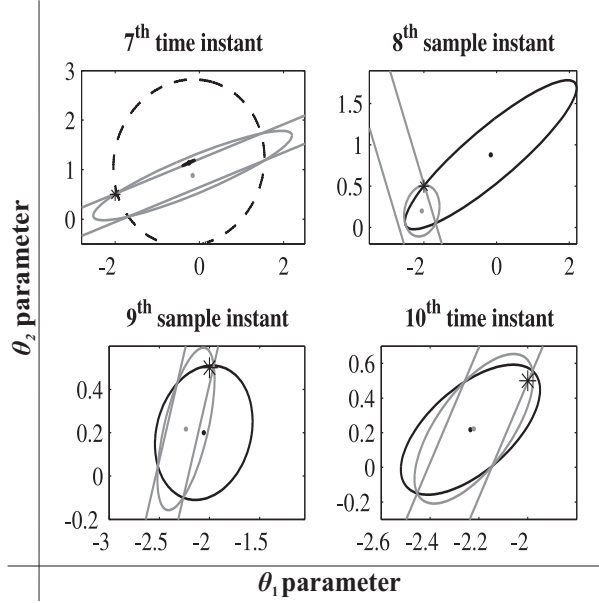


Figure 3.16: Backward-in-time fault detection example ( $n = 2$ ).

### 3.6.3 Characterization of Algorithm Sensitivity

The proposed FDD method based on parameter estimation is designed in a set membership framework, presupposing the knowledge of: a) a linearly parametrizable model, b) the noise error bounds, c) the parameter perturbation bounds, d) the safe operation parameter bounds, and e) the minimum length of time window  $L$  related to the jump parameter case.

The proper structure of the linearly parametrizable model is necessary for the initialization of the algorithm. However, there are cases in which system dynamics is not captured by the utilized linearly parametrizable model (i.e. some non-linearities are linearised to simplify the model). Then, a model error representing the system dynamics can be incorporated in the model, whose bounds should be estimated under faultless operating conditions [92], [93]. Moreover, the linearly parametrizable model should be formed so as its output and the components of regression vector to be functions of measurable signals. In addition, the components of regression vector should be linearly independent and must span the parametric space. Failure to do so, because of linear dependence, may leave the nominal parameter vector unbounded in at least one direction [94].

### 3. FAULT DETECTION AND DIAGNOSIS

---

The capability of knowing the measurement noise bounds is related to its source. Measurement noise may stem from: a) errors of sensing instruments, b) quantization errors due to analog-to-digital conversion and c) thermal noise. In regard to the first type of noise, most sensor manufacturers provide rules for computing the maximum and minimum possible instrumentation errors, while the bounds of quantization errors are computed from the full-scale analogue range of the converter. Any information about the latter type can be collected experimentally, recording its distribution either in time or frequency domain. Based on the time-domain distribution, the bounds can be determined directly, while using the frequency-domain distribution, there are cases in which its statistical properties can be associated with the deterministic bounds. Particularly, under the assumption of a zero-mean uniform distribution on  $[-\varepsilon, \varepsilon]$  with variance  $\sigma^2$ ,  $\varepsilon = \sqrt{3\sigma^2}$  can be used. Under the assumption of a zero-mean Gaussian process with variance  $\sigma^2$ , the choice of  $\varepsilon = \alpha\sigma$ , with  $\alpha > 1$  will yield to a probability of noise bound violation equal to  $2Q(\alpha)$ , where  $Q$  is the Q-function. Hence, if  $\alpha = 3$ , the probability of noise bound violation is 0.3% of the time [95]. If there is inadequate knowledge of the noise bounds, then a selection of a larger value

$$e_{y(\phi_u)}^{\max} = \beta \max_i \frac{1}{\sqrt{\mu_{y(\phi_u)}(i)}}, \quad \beta \gg 1$$

can be used; however in this case, certain faults may not be captured.

The bounds of parameter perturbations can be arisen from material characterization, where parameter variation due to environmental changes, ageing, life cycle can be estimated [38]. Also in this case, larger values can be used, which may affect the detectability of the faults.

In a single fault detection (no isolation), there is no need to a priori know the safe operation bounds. In general larger values of the safe operation bounds can be selected to ensure that the resetting parametric set will capture the new nominal parameter vector after each fault detection. However this may lead to slow convergence of the volume of ellipsoids or orthotopes and may result in a delayed isolation.

For a jump-system with a small dwell-time  $L$ , if the fault is not detected fast enough, this will affect the fault diagnosis component. For the case where  $i^{d_j} - i^{f_j} > L$ , another fault can occur prior to the  $i^{d_j}$  instant ( $i^{f_{j+1}} < i^{d_j}$ ) leading to incorrect fault isolation.

Even in the case where  $L$  is large enough, in pathological cases, regression vectors  $\phi(i)$ ,  $i > i^{f_j}$  can be selected leading to a very late  $i^{d_j}$  ( $i^{d_j} \gg i^{f_j}$ ). In this case, the fault isolation module will compute the intersection of the support orthotopes or orthotopes over a window-span where outputs from the neighbouring ‘faulty’ systems ((3.1)-(3.2) or (3.58)) will contribute. In these pathological cases, the fault isolation module may provide an incorrect event.

### 3.7 Conclusions

In this chapter, the design of the Fault Detection and Diagnosis (FDD) technique in a set membership framework, relying on parameter orthotopic or ellipsoidal set estimation is presented. The objective of the proposed FDD method is to capture and diagnose abrupt parametric faults of a jump linearly parametrizable, time-varying system. The fault detection is accomplished when the normal operation of the SMI is violated, due to an empty intersection between the data-hyperspace and the estimated parametric set. The fault isolation procedure relies on the projection of the parametric sets (orthotopes or ellipsoids) computed by the normal operation of SMI, after the fault detection, and the worst-case parametric sets, while the distance of the centers of projections is utilized for fault identification. Moreover, under the assumption of a time invariant parameter vector and in case of the ellipsoidal SMI, the consistency test based on the intersection of support orthotopes is used for fault detection. The analysis of the FDD procedure is concluded by discussing the detectability of the faults, the possibility of a better estimation of the time instant of fault occurrence by applying a backward-in-time fault detection algorithm and the characterization of the algorithm sensitivity in relation to the inherent assumptions.

### **3. FAULT DETECTION AND DIANGOSIS**

---

## Chapter 4

# Fault Detection and Diagnosis applied in Microelectromechanical Systems

### 4.1 Introduction

The objective of this chapter is the application of the fault detection and diagnosis (FDD) methods based on orthotopic and ellipsoidal set membership identification (SMI) in order to capture and diagnose failure modes typically appeared in two distinct MEMS-technology examples; an electrostatic parallel plate micro-actuator [96], [97] and a torsionally-resonant atomic force microscope (TR-AFM) [98], [99]. These failure modes are treated as system parameters variations causing abnormal systems performance [38], [100].

Electrostatic microactuators are usually embedded in other MEMS devices due to their simplicity of operation and ease of fabrication. The parallel-plate electrostatic actuation works on the principle of Coulomb attraction between the opposite charged suspended mass and a substrate, generating an electrostatic force. This force is inversely proportional to the square of the distance between the plates. Between the plate and the substrate, there is a film of viscous air, which is the dominant dissipation mechanism. In open-to-air applications, there is a chance that dust and other particles enter at the interior of the device and cause a change of mass. The silicon-made structures absorb humidity of air that results in change of mechanical properties of suspension springs. For devices operating in vacuum conditions, any damage in the container might result in the loss of hermeticity and consequently change of viscosity.

The TR-AFM is the device that utilized for investigating the tribological phenomena of materials such as surface roughness, adhesion, friction e.t.c and generating

## 4. FAULT DETECTION AND DIAGNOSIS APPLIED IN MICROELECTROMECHANICAL SYSTEMS

---

high resolutions 3D images of the samples. The TR-AFM consists of a rectangular cantilever with a conical tip attached at its far end and interacts with the sample, while two piezoelectric elements are used as a support torsion of the cantilever. During measurements, the tip remains close to the sample surface, ensuring more intensive tip-sample interaction and more surface material properties-related information. However, this intensive tip-sample interaction may result in the growth of failure mechanisms such as the particle contamination of its tip, the adhesion and friction leading to tip's wear and fatigue resulted in tip's fracture.

In the simulation studies illustrated in this chapter, a simplified mass-spring-damper model [101], [102], [103] is utilized in to describe the dynamics of the electrostatic parallel-plate microactuator under the assumption of time-invariant parameters. The fault scenario addresses that the microactuator is subject to multiple abrupt variations in its mass, spring stiffness and damping coefficient. In the TR-AFM example, the initial goal is to obtain the lumped parameter model taking into account the Euler-Bernoulli partial differential equation describing the torsional vibration and a Kelvin-Voigt model describing the tip-sample interaction. The Kelvin-Voigt model is a combination of a spring (a function of the tip's radius), in parallel with a Newtonian dashpot that corresponds to the dissipative forces. According to the fault scenario, tip's fractures occur when the TR-AFM is operating in the repulsive regime scanning a rough surface. These fractures are going to be detected as abrupt variations of tip's radius under the assumption of a time-varying linearly parametrizable model [104].

### 4.2 Parallel-Plate Electrostatic Micro-Actuator

A simplified testbed layout of a typical electrostatic micro-actuator is shown in Figure 4.1a, which consists of a plate suspended from the substrate by four serpentine springs. The movable plate is controlled by the application of the voltage  $V$  between the plates. Maintaining only the primary mode of motion results in a simplified mass-spring-damper model of this micro-actuator as shown in Fig. 4.1b.

If  $z$  is the vertical displacement of the movable plate,  $z_{\max}$  is its maximum unactuated displacement,  $m^\circ$  is the plate's mass,  $k^\circ$  is the spring stiffness,  $c^\circ$  is the damping coefficient,  $A$  is the plate's area and  $\epsilon_a$  is the air's dielectric constant, and  $F_{el}$  is the generated electrostatic force, then the dynamics of the aforementioned faultless nominal microactuator is:

$$m^\circ \ddot{z} + c^\circ \dot{z} + k^\circ z = \frac{\epsilon_a A V^2}{2(z - z_{\max})^2} = F_{el} . \quad (4.1)$$

The parameters used in the simulation studies are:  $m^\circ = 7.0496 \cdot 10^{-10}$  Kgr,  $c^\circ = 1e-5$  Nsec/m,  $k^\circ = 0.8$  N/m,  $A = 400 \cdot 10^{-6} \times 400 \cdot 10^{-6}$  m<sup>2</sup>,  $\epsilon_a = 8.85 \cdot 10^{-12}$  F/m and  $z_{\max} = 4 \cdot 10^{-6}$  m.



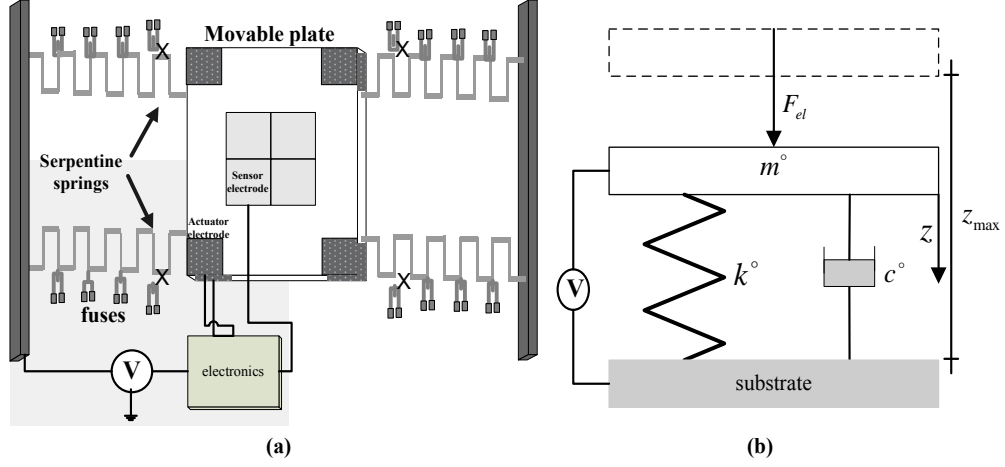


**Figure 4.1:** a) Simplified testbed layout and b) mass-spring-damper model of a parallel-plate electrostatic micro-actuator.

Let the linearly parametrizable system at the  $i$ th instant be defined as:

$$F_{el}(i) = [\ddot{z}(i), \dot{z}(i), z(i)] \begin{bmatrix} m^\circ \\ c^\circ \\ k^\circ \end{bmatrix} \Rightarrow y(i) = \phi^T(i) \theta^\circ. \quad (4.2)$$

The nominal parameter vector  $\theta^\circ = [\theta_1^\circ, \theta_2^\circ, \theta_3^\circ]^T = [704.96 \frac{\mu\text{N}\mu\text{sec}^2}{\mu\text{m}}, 10 \frac{\mu\text{N}\mu\text{sec}}{\mu\text{m}}, 0.8 \frac{\mu\text{N}}{\mu\text{m}}]$  is assumed to be time-invariant. Moreover, the observed data  $z^m(i)$  ( $\mu\text{m}$ ),  $\ddot{z}^m(i)$  ( $\frac{\mu\text{m}}{\mu\text{sec}^2}$ ) are typically collected from the displacement and acceleration signals provided by the off-chip electronics,  $F_{el}^m(i)$  ( $\mu\text{N}$ ) is extracted by the actuator force signals [96], and  $\dot{z}^m(i)$  ( $\frac{\mu\text{m}}{\mu\text{sec}}$ ) is assumed to be measured using a laser vibrometer [105] and  $i \in [1, 10000]$ . The system operates in open-loop within its stable region ( $0 < z < \frac{z_{max}}{3}$ ).

The observed data  $y^m(i), \phi_1^m(i), \phi_2^m(i), \phi_3^m(i)$  are given as:

$$\begin{aligned} y^m(i) &= F_{el}^m(i) = F_{el}(i) + e_y(i), & |e_y(i)| &\leq e_y^{\max} \\ \phi_1^m(i) &= \ddot{z}^m(i) = \ddot{z}(i) + e_{\phi_1}(i), & |e_{\phi_1}(i)| &\leq e_{\phi_1}^{\max} \\ \phi_2^m(i) &= \dot{z}^m(i) = \dot{z}(i) + e_{\phi_2}(i), & |e_{\phi_2}(i)| &\leq e_{\phi_2}^{\max} \\ \phi_3^m(i) &= z^m(i) = z(i) + e_{\phi_3}(i) & |e_{\phi_3}(i)| &\leq e_{\phi_3}^{\max}, \end{aligned} \quad (4.3)$$

where  $e_y(i), e_{\phi_u}(i), u = 1, 2, 3$  correspond to noises that stem from the sensor instruments and electronics with the worst case bounds  $e_y^{\max}, e_{\phi_u}^{\max}$  computed taking into account SNR=55dB.

It is regarded that multiple abrupt parameter variations in its mass, spring stiffness, and damping coefficient of the microactuator occur following the fault scenario

#### 4. FAULT DETECTION AND DIAGNOSIS APPLIED IN MICROELECTROMECHANICAL SYSTEMS

---

**Table 4.1:** Electrostatic Micro-actuator Fault Instances

$if_j$	2001	3001	4001	5001	6001	7001
$j$	1	2	3	4	5	6
$\frac{\Delta m}{m^\circ}$	0.05	0.10	0	0	0	0
$\frac{\Delta k}{k^\circ}$	0	0	0.05	0.1	0	0
$\frac{\Delta c}{c^\circ}$	0	0	0	0	0.3	0

presented in [53], which are provided in Table 4.1. The maximum allowable bounds are of  $\tilde{\gamma}_1^{\max} = 30\%\theta_1^\circ$ ,  $\tilde{\gamma}_2^{\max} = 40\%\theta_2^\circ$  and  $\tilde{\gamma}_3^{\max} = 30\%\theta_3^\circ$  respectively, while  $L = 500$ .

The objective of this study is to capture and diagnose the faults presented in Table 4.1, applying the following FDD schemes:

- (A) FDD based on Orthotopic SMI using data-hyperstrips,
- (B) FDD based on Orthotopic SMI using data-hypersectors,
- (C) FDD based on Ellipsoidal SMI using data-hyperstrips,
- (D) FDD based on Ellipsoidal SMI using data-hypersectors,

where the **data-hyperstrips** are generated according to

$$S^P(i) = \{ \theta : y^m(i) - \tilde{e}^{\max}(i) \leq \phi^m(i)^T \theta \leq y^m(i) + \tilde{e}^{\max}(i) \}, \quad (4.4)$$

$$\tilde{e}^{\max}(i) = e_y^{\max} + \sum_{u=1}^3 e_{\phi_u}^{\max} \max \left( \left| \theta_{z_u}^-(i-1) \right|, \left| \theta_{z_u}^+(i-1) \right| \right). \quad (4.5)$$

with  $Z_u = \Omega_u$  in case of orthotopic SMI-based FDD or  $Z_u = \mathcal{X}_u$  in case of ellipsoidal SMI-based FDD, and the **data-hypersectors** are generated according to

$$S^{np}(i) = \left\{ \theta : y^m(i) - e_y^{\max} \leq \phi^A(i)^T \theta \text{ and } \phi^B(i)^T \theta \leq y^m(i) + e_y^{\max} \right\}, \quad (4.6)$$

where  $\phi^A(i)$ ,  $\phi^B(i)$  are described by (2.42) and (2.43) with  $\text{sgn}(\theta_1^\circ) = \text{sgn}(\theta_2^\circ) = \text{sgn}(\theta_3^\circ) = 1$ , resulting in

$$\phi^A(i) = \begin{bmatrix} \phi_1^m(i) + e_{\phi_1}^{\max} & \phi_2^m(i) + e_{\phi_2}^{\max} & \phi_3^m(i) + e_{\phi_3}^{\max} \end{bmatrix}^T, \quad (4.7)$$

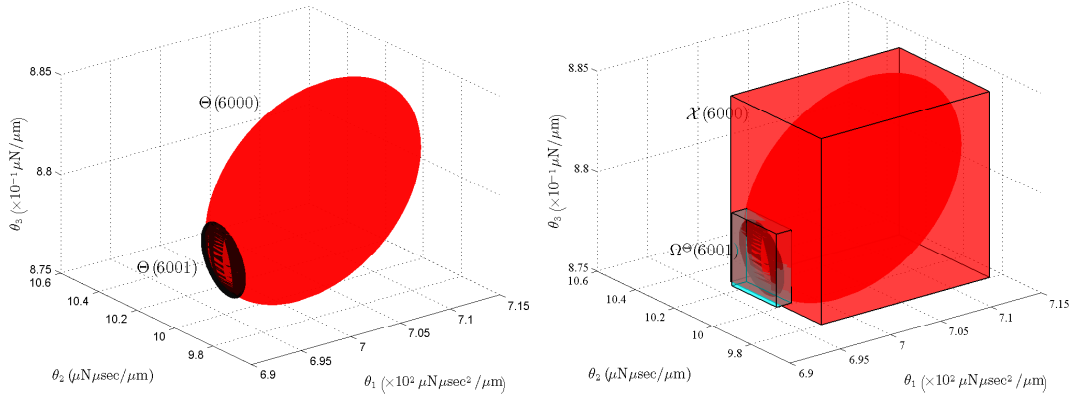
$$\phi^B(i) = \begin{bmatrix} \phi_1^m(i) - e_{\phi_1}^{\max} & \phi_2^m(i) - e_{\phi_2}^{\max} & \phi_3^m(i) - e_{\phi_3}^{\max} \end{bmatrix}^T. \quad (4.8)$$

The abrupt parameter variations of  $\theta^\circ + \Delta\theta(i^j)$ , for  $j = 1, \dots, 6$  are detected by the aforementioned FDD schemes at the same time instances  $i^{d_j}$   $j = 1, \dots, 6$ , as shown in the Table 4.2. It is observed that there is a delay between the fault occurrence

**Table 4.2:** Electrostatic Micro-actuator–Time Instances of Fault Occurrence and Detection

$j$	1	2	3	4	5	6
$i^j$	2001	3001	4001	5001	6001	7001
$((A) - (D)) - i^{d_j}$	2001	3001	4001	5004	6001	7003

$i^{f_j}$  and the detection instances  $i^{d_j}$  for  $j = 4, 6$ . Applying the (A) and (B) schemes, the fault is detected when  $\Omega(i^{d_j} - 1) \cap S(i^{d_j}) = \emptyset \forall i^{d_j}$ . In the case of (C) and (D) schemes the fault is detected when  $\Theta(i^{d_j} - 1) \cap S(i^{d_j}) = \emptyset$  for  $i^{d_j}$ ,  $j = 1, 2, 3, 4, 6$  and  $\mathcal{X}(i^{d_s} - 1) \cap \Omega^\ominus(i^{d_s}) = \emptyset$ . The fault detection applying the (D) scheme at  $i^{d_s} = 6001$  is presented in the following figures. Particularly, Fig. 4.2(a) presents the generated ellipsoids  $\Theta(i^{d_s})$ ,  $\Theta(i^{d_s} - 1)$ , which along with the generated intersection of support orthotopes  $\mathcal{X}(i^{d_s} - 1)$  and support orthotope  $\Omega^\ominus(i^{d_s})$  are depicted in Fig. 4.2(b).



(a) Ellipsoids  $\Theta(6000)$  and  $\Theta(6001)$  computed via (b) Ellipsoids  $\Theta(6000)$  and  $\Theta(6001)$  and intersections of orthotopes (6000) and (6001) computed via (D) scheme

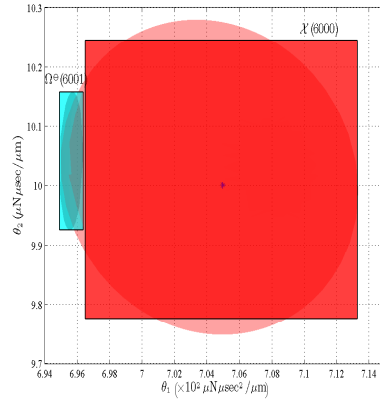
**Figure 4.2:** Fault detection case via the (D) scheme at  $i^{d_s} = 6001$ 

Fig. 4.3 shows the 2D projection of the parametric sets presented in Fig. 4.2(b), in which the empty intersection between the  $\mathcal{X}(i^{d_s} - 1)$  and  $\Omega^\ominus(i^{d_s})$  is observed.

In the (A) and (B) schemes, the resetting procedure is implemented according to Theorem 3.5.1, while in the (C) and (D) schemes, the resetting procedure presented in Theorem 3.5.3 is applied.

Figures 4.4, 4.5 and 4.6 present the upper bounds [lower bounds] (A)–  $\theta_{\Omega_u}^+(i)$  [ $\theta_{\Omega_u}^-(i)$ ] ((black)–dashed [solid] line), (B)– $\theta_{\Omega_u}^+(i)$  [ $\theta_{\Omega_u}^-(i)$ ] ((red)–dashed [solid] line),

#### 4. FAULT DETECTION AND DIAGNOSIS APPLIED IN MICROELECTROMECHANICAL SYSTEMS



**Figure 4.3:** Empty intersection case between  $\mathcal{X}(6000)$  and  $\Omega^{\circ}(6001)$

(C)– $\theta_{\mathcal{X}_u}^+(i)$  [ $\theta_{\mathcal{X}_u}^-(i)$ ] ((blue)–dashed [solid] line), (D)– $\theta_{\mathcal{X}_u}^+(i)$  [ $\theta_{\mathcal{X}_u}^-(i)$ ] ((green)–dashed [solid] line),  $u = 1, 2, 3$ . The nominal values of  $\theta_u^{\circ} + \Delta\theta_u(i^{f_j})$  are indicated on the vertical axis and the time instances of fault detection  $i^{d_j}$  are shown on the horizontal axis of these figures.

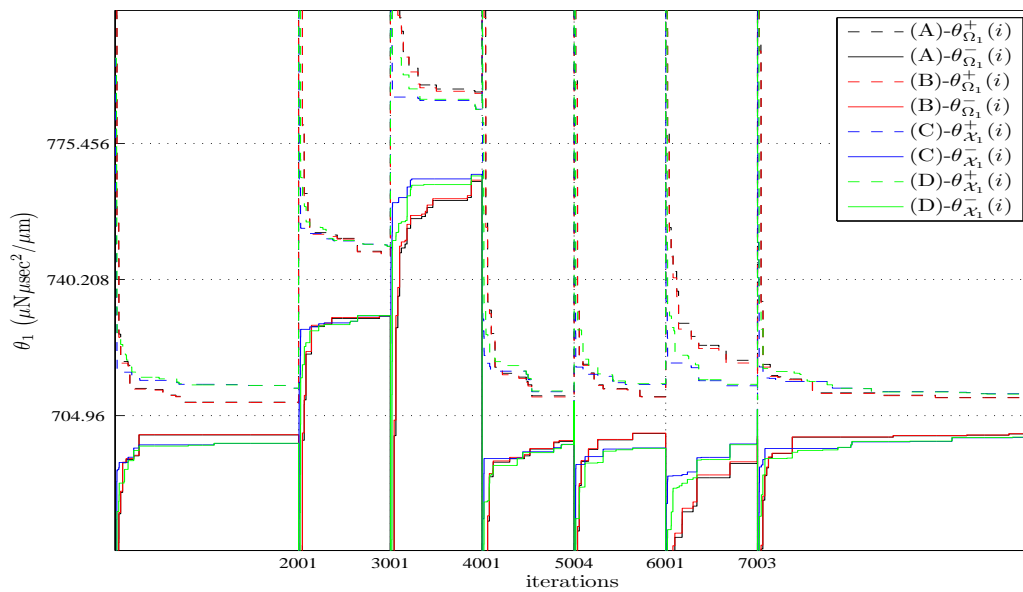


**Figure 4.4:** Electrostatic microactuator–Time evolution of upper and lower bounds of  $\theta_1^{\circ}$  generated by the FDD schemes.

## 4.2 Parallel-Plate Electrostatic Micro-Actuator

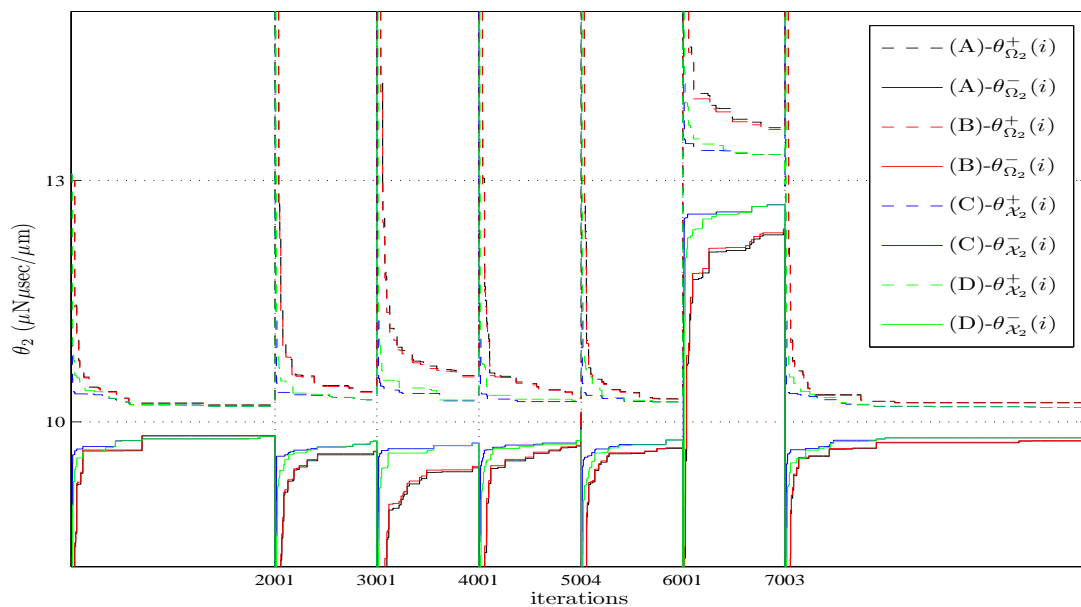


**Figure 4.5:** Electrostatic microactuator–Time evolution of upper and lower bounds of  $\theta_2^\circ$  generated by the FDD schemes.

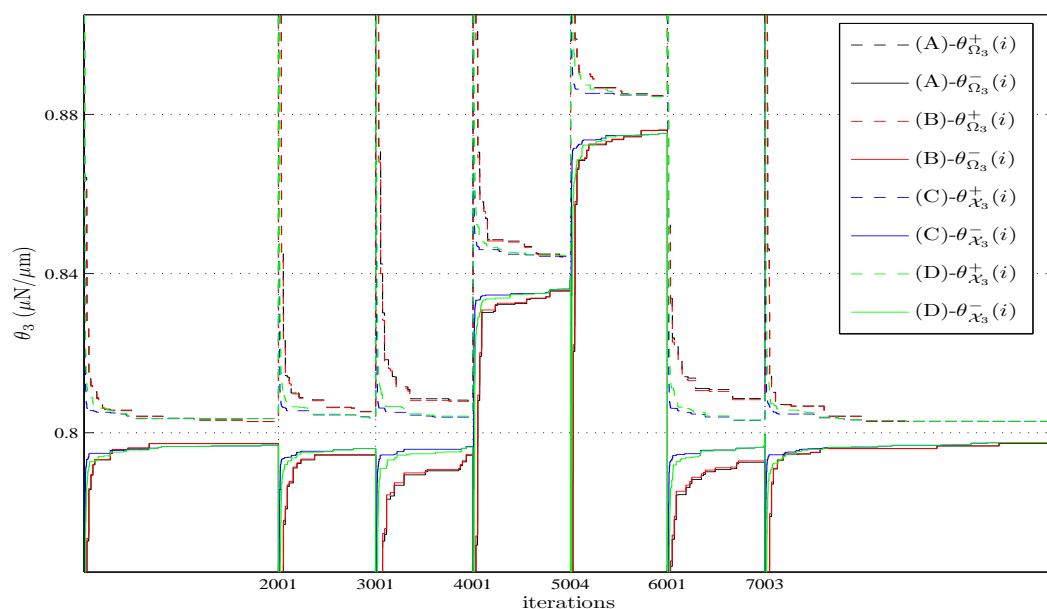


**Figure 4.6:** Electrostatic microactuator–Time evolution of upper and lower bounds of  $\theta_3^\circ$  generated by the FDD schemes.

#### 4. FAULT DETECTION AND DIAGNOSIS APPLIED IN MICROELECTROMECHANICAL SYSTEMS

---

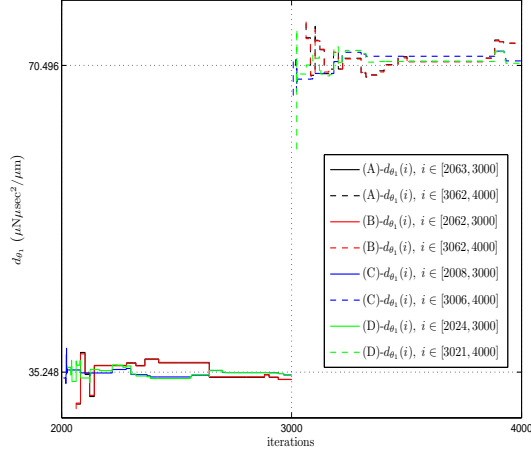
Based on the these diagrams, the fault isolation instances for each component of the parameter vector are summarized in Table 4.3, with the type of isolation denoted as F/NF/U for the "Faulty/Non Faulty/Undetermined" cases. The faulty status of  $\theta_u, u = 1, 2, 3$  is inferred by all FDD schemes, while the undetermined status is due to the small size of  $\Omega_u(i^{d_1} - 1)$  in (A),(B) and  $\mathcal{X}(i^{d_1} - 1)$  in (C), (D) schemes which cannot satisfy the conditions described in (3.92) and (3.93). In addition, the fault isolation in (C) and (D) schemes is realized earlier than in (A) and (B) schemes, because of the fact that the volume of orthotope is decreasing slower than the volume of ellipsoid.

**Table 4.3:** Electrostatic Micro-actuator Parameter Vector Isolation Instants

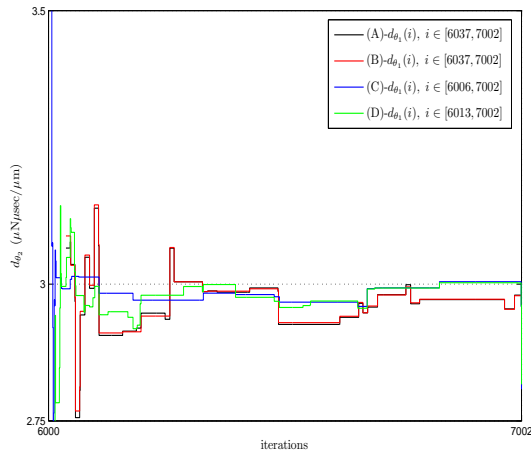
<b>(A)</b>						
$i^1*(F/NF/U)$	2063(F)	3062(F)	(U)	(U)	(U)	(U)
$i^2*(F/NF/U)$	(U)	(U)	(U)	(U)	6037(F)	(U)
$i^3*(F/NF/U)$	(U)	(U)	4051(F)	5031(F)	(U)	(U)
<b>(B)</b>						
$i^1*(F/NF/U)$	2062(F)	3062(F)	(U)	(U)	(U)	(U)
$i^2*(F/NF/U)$	(U)	(U)	(U)	(U)	6037(F)	(U)
$i^3*(F/NF/U)$	(U)	(U)	4051(F)	5031(F)	(U)	(U)
<b>(C)</b>						
$i^1*(F/NF/U)$	2008(F)	3006(F)	(U)	(U)	(U)	8153(NF)
$i^2*(F/NF/U)$	(U)	(U)	(U)	(U)	6006(F)	(U)
$i^3*(F/NF/U)$	(U)	(U)	4008(F)	5009(F)	(U)	8814(NF)
<b>(D)</b>						
$i^1*(F/NF/U)$	2024(F)	3021(F)	(U)	(U)	(U)	8032(NF)
$i^2*(F/NF/U)$	(U)	(U)	(U)	(U)	6013(F)	(U)
$i^3*(F/NF/U)$	(U)	(U)	4020(F)	5016(F)	(U)	8814(NF)

The fault isolation is followed by the estimation of the parameter variation  $\Delta\theta_u(i^{f_j}), u = 1, 2, 3$  of the faulty components for the time window starting at the time instant of fault isolation up to the next time instant of fault detection, as shown in Fig. 4.7(a), 4.7(b) and 4.7(c).

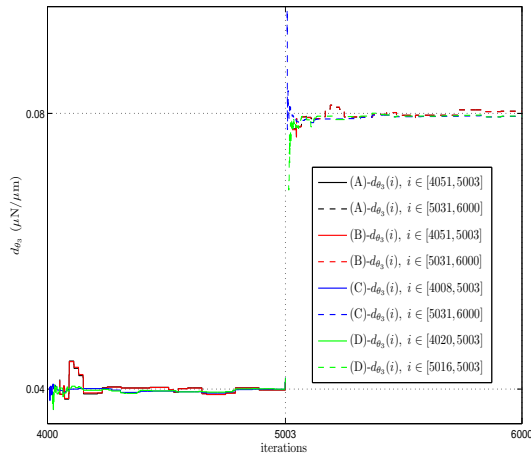
## 4.2 Parallel-Plate Electrostatic Micro-Actuator



(a)  $d_{\theta_1}$ -estimation of  $\Delta\theta_1(i^{f_j})$ ,  $j = 1, 2$



(b)  $d_{\theta_2}$ -estimation of  $\Delta\theta_2(i^{f_j})$ ,  $j = 5$ .



(c)  $d_{\theta_3}$ -estimation of  $\Delta\theta_2(i^{f_j})$ ,  $j = 3, 4$ .

Figure 4.7: Fault Identification of microactuator parameter vector

## 4. FAULT DETECTION AND DIAGNOSIS APPLIED IN MICROELECTROMECHANICAL SYSTEMS

### 4.3 Torsional Resonant Atomic Force Microscope

#### 4.3.1 Lumped-Parameter Modelling

The schematic diagram of the torsional resonant AFM is presented in Fig 4.8. In particular, an AFM consists of a rectangular cantilever ( $L_c$ : length,  $b_c$ : width,  $h_c$ : thickness) with a conical tip ( $R_t$ : radius of tip's apex,  $l_t$ : tip's length) attached at its far end, at its longitudinal axis. Two piezoelectric elements are located at the base of the cantilever and oscillate in opposite directions, resulting in a support torsion of the cantilever. The sample surface lays on a PZT tube scanner, while the optical lever method is used to measure the deflection of the cantilever. A laser beam is projected on the upper surface of the cantilever close to the tip and then is led by a mirror into a four-segment photodiode.

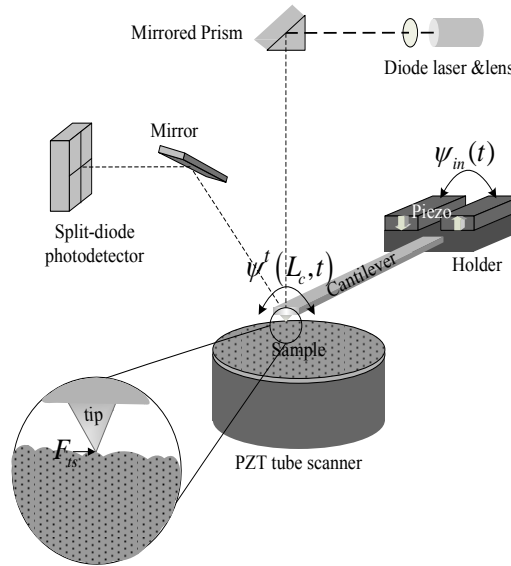


**Figure 4.8:** Schematic diagram of a torsionally resonant AFM interacting with a sample surface

The torsional vibration of the cantilever taking into account the moment,  $M_{ts}$ , generated by the tip-sample interaction force is described via the Euler-Bernoulli equation:

$$GJ \frac{\partial^2 \psi^t(x, t)}{\partial x^2} = \rho I_\rho \frac{\partial^2 \psi^t(x, t)}{\partial t^2} + c \frac{\partial \psi^t(x, t)}{\partial t} - M_{ts}, \quad (4.9)$$

where  $\psi^t(x, t)$ ,  $x \in [0, L_c]$  is the total torsion (rad),  $G$  is the shear modulus,  $J$  is the torsional constant,  $\rho$  is the mass density,  $I_\rho$  is the polar area moment of in-



### 4.3 Torsional Resonant Atomic Force Microscope

ertia and  $c$  is the coefficient of viscous damping. For a rectangular cantilever,  $J \approx \frac{1}{3}b_c h_c^3 \left[ 1 - 0.63 \left( \frac{h_c}{b_c} \right) + 0.052 \left( \frac{h_c}{b_c} \right)^5 \right]$  and  $I_\rho = \frac{1}{12} (h_c b_c^3 + b_c h_c^3)$ .

In pure torsional analysis, the moment  $M_{ts}$  is given as:

$$M_{ts} = l_t F_{ts} \quad (4.10)$$

and the tip-sample interaction  $F_{ts}$  is represented by the Kelvin-Voigt model, which is a combination of a spring in parallel with a Newtonian dashpot:

$$F_{ts} = -k_l \Delta_l - c_l \dot{\Delta}_l, \quad (4.11)$$

where  $\Delta_l$  is the displacement in lateral direction,  $k_l$  and  $c_l$  are the lateral stiffness and damping coefficients, respectively [106]. Based on Hertzian contact theory, the calculation of the lateral contact stiffness is realized via the equation:

$$k_l = \begin{cases} 0, & \delta_0 > \alpha_0 \quad (\text{attractive regime}) \\ 8G^* \sqrt{R_t (\alpha_0 - \delta_0)}, & \delta_0 \leq \alpha_0 \quad (\text{repulsive regime}) \end{cases} \quad (4.12)$$

where  $\delta_0$  is the equilibrium tip-sample separation,  $\alpha_0$  is the intermolecular distance,  $H$  is the Hamacker constant and  $G^*$  is the effective shear modulus. The aforementioned displacement is computed as:

$$\Delta_l = l_t \psi^t(L_c, t) = l_t \psi^t(x, t) \delta(x - L_c), \quad (4.13)$$

where  $\psi^t(L_c, t)$  is the total rotation at the end of the cantilever and  $\delta(\cdot)$  denotes the impulse function. Substituting (4.11) and (4.13) into (4.10) yields:

$$M_{ts} = -k_l l_t^2 \psi^t(x, t) \delta(x - L_c) - c_l l_t^2 \frac{\partial \psi^t(x, t)}{\partial t} \delta(x - L_c). \quad (4.14)$$

Introducing the last equation into (4.9) results in:

$$GJ \frac{\partial^2 \psi^t(x, t)}{\partial x^2} = \rho I_\rho \frac{\partial^2 \psi^t(x, t)}{\partial t^2} + c \frac{\partial \psi^t(x, t)}{\partial t} + \left( k_l \psi^t(x, t) + c_l \frac{\partial \psi^t(x, t)}{\partial t} \right) l_t^2 \delta(x - L_c) \quad (4.15)$$

The total torsion of the cantilever is expressed as the sum of the torsion that is induced by static application of the support motion and equals to the quasi static torsion generated from the dual piezo-elements  $\psi_{in}(t)$ , plus the additional torsion  $\psi(x, t)$  due to dynamic inertia and viscous force effects ([107]):

$$\psi^t(x, t) = \psi(x, t) + \psi_{in}(t), \quad (4.16)$$

with  $\psi_{in}(t) = \psi_0 \sin(\omega_{in} t)$ . Using (4.16), (4.15) is altered to:

$$GJ \frac{\partial^2 \psi(x, t)}{\partial x^2} = \rho I_\rho \frac{\partial^2 \psi(x, t)}{\partial t^2} + c \frac{\partial \psi(x, t)}{\partial t} + \left( k_l \psi(x, t) + c_l \frac{\partial \psi(x, t)}{\partial t} \right) l_t^2 \delta(x - L_c) + \rho I_\rho \ddot{\psi}_{in}(t) + c \dot{\psi}_{in}(t) + (k_l \psi_{in}(t) + c_l \dot{\psi}_{in}(t)) l_t^2 \delta(x - L_c). \quad (4.17)$$

#### 4. FAULT DETECTION AND DIAGNOSIS APPLIED IN MICROELECTROMECHANICAL SYSTEMS

---

In most practical cases, the damping contribution to the effective load is small compared to the inertial contribution and  $c\psi_{in}(t) = 0$ .

The goal of this section is the transformation from the geometric torsional coordinates to the modal-amplitude or normal coordinates and is accomplished following the mode superposition analysis. This transformation is expressed as:

$$\psi(x, t) = \sum_{q=1}^{\infty} \Psi_q(t) \xi_q(x), \quad (4.18)$$

where  $\Psi_q(t)$  is the time-dependent amplitude and  $\xi_q(x)$  is the modal shape, computed by:

$$\frac{d^2 \xi_q(x)}{dx^2} + \frac{\rho I_\rho}{GJ} \omega_q^2 \xi_q(x) = 0. \quad (4.19)$$

The detailed computation of modal shape is presented in Appendix A.4. Introducing (4.18) and (4.19) into (4.17) results in:

$$\begin{aligned} -\rho I_\rho \sum_{q=1}^{\infty} \omega_q^2 \Psi_q(t) \xi_q(x) &= \rho I_\rho \sum_{q=1}^{\infty} \ddot{\Psi}_q(t) \xi_q(x) + c \sum_{q=1}^{\infty} \dot{\Psi}_q(t) \xi_q(x) + \\ &k_l \sum_{q=1}^{\infty} \Psi_q(t) \xi_q(x) l_t^2 \delta(x - L_c) + c_l \sum_{q=1}^{\infty} \dot{\Psi}_q(t) \xi_q(x) l_t^2 \delta(x - L_c) + \\ &\rho I_\rho \ddot{\psi}_{in}(t) + (k_l \psi_{in}(t) + c_l \dot{\psi}_{in}(t)) l_t^2 \delta(x - L_c). \end{aligned} \quad (4.20)$$

Multiplying by  $\xi_q(x)$ , integrating by  $\int_0^{L_c}$  and applying the orthogonality relationship (see Appendix A.4) yields:

$$\begin{aligned} -\omega_q^2 \left( \int_0^{L_c} \rho I_\rho \xi_q(x)^2 dx \right) \Psi_q(t) &= \left( \int_0^{L_c} \rho I_\rho \xi_q(x)^2 dx \right) \ddot{\Psi}_q(t) + \frac{c}{\rho I_\rho} \left( \int_0^{L_c} \rho I_\rho \xi_q(x)^2 dx \right) \dot{\Psi}_q(t) + \\ &k_l l_t^2 \left( \int_0^{L_c} \xi_q(x)^2 \delta(x - L_c) dx \right) \Psi_q(t) + c_l l_t^2 \left( \int_0^{L_c} \xi_q(x)^2 \delta(x - L_c) dx \right) \dot{\Psi}_q(t) + \\ &\left( \int_0^{L_c} \rho I_\rho \xi_q(x) dx \right) \ddot{\psi}_{in}(t) + \\ &k_l l_t^2 \left( \int_0^{L_c} \xi_q(x) \delta(x - L_c) dx \right) \psi_{in}(t) + c_l l_t^2 \left( \int_0^{L_c} \xi_q(x) \delta(x - L_c) dx \right) \dot{\psi}_{in}(t). \end{aligned}$$

Defining the generalized mass  $M_q^* = \int_0^{L_c} \rho I_\rho \xi_q(x)^2 dx$  and the term  $\mathcal{L}^* = \int_0^{L_c} \rho I_\rho \xi_q(x) dx$ , the last equation is transformed in:

$$\begin{aligned} M_q^* \ddot{\Psi}_q(t) + \left( \frac{c}{\rho I_\rho} M_q^* + c_l l_t^2 \xi_q(L_c)^2 \right) \dot{\Psi}_q(t) + \left( \omega_q^2 M_q^* + k_l l_t^2 \xi_q(L_c)^2 \right) \Psi_q(t) = \\ -\mathcal{L}^* \ddot{\psi}_{in}(t) - c_l l_t^2 \xi_q(L_c) \dot{\psi}_{in}(t) - k_l l_t^2 \xi_q(L_c) \psi_{in}(t) \end{aligned} \quad (4.21)$$

or else,

$$\begin{aligned} \ddot{\Psi}_q(t) + \left( \frac{c}{\rho I_\rho} + \frac{c_l l_t^2 \xi_q(L_c)^2}{M_q^*} \right) \dot{\Psi}_q(t) + \left( \omega_q^2 + \frac{k_l l_t^2 \xi_q(L_c)^2}{M_q^*} \right) \Psi_q(t) = -\frac{\mathcal{L}^*}{M_q^*} \ddot{\psi}_{in}(t) - \\ \frac{c_l l_t^2 \xi_q(L_c)}{M_q^*} \dot{\psi}_{in}(t) - \frac{k_l l_t^2 \xi_q(L_c)}{M_q^*} \psi_{in}(t). \end{aligned} \quad (4.22)$$

---

### 4.3 Torsional Resonant Atomic Force Microscope

---

The computation of  $M^*$ ,  $\mathcal{L}^*$ ,  $\xi_q(L_c)$ ,  $\xi_q(L_c)^2$  is provided in the Appendix A.4. The readout of the measuring signal by the photodiode is:

$$\psi^t(L_c, t) = \psi(L_c, t) + \psi_{in}(t). \quad (4.23)$$

Using (4.18), it yields:

$$\psi^t(L_c, t) = \sum_{q=1}^{\infty} \Psi_q(t) \xi_q(L_c) + \psi_{in}(t) = \sum_{q=1}^{\infty} \psi_q(L_c, t) + \psi_{in}(t) \quad (4.24)$$

For the determination of  $\psi_q(L_c, t)$ , both sides of (4.22) are multiplied with  $\xi_q(L_c)$ , implying:

$$\begin{aligned} \ddot{\psi}_q(L_c, t) + \left( \frac{c}{\rho I_p} + \frac{c l_t^2 \xi_q(L_c)^2}{M_q^*} \right) \dot{\psi}_q(L_c, t) + \left( \omega_q^2 + \frac{k l_t^2 \xi_q(L_c)^2}{M_q^*} \right) \psi_q(L_c, t) = \\ - \frac{\xi_q(L_c) \mathcal{L}^*}{M_q^*} \ddot{\psi}_{in}(t) - \frac{c l_t^2 \xi_q(L_c)^2}{M_q^*} \dot{\psi}_{in}(t) - \frac{k l_t^2 \xi_q(L_c)^2}{M_q^*} \psi_{in}(t) \end{aligned} \quad (4.25)$$

Consequently, the transfer function  $H_q(s) = \frac{\psi(L_c, s)}{\psi_{in}(s)}$  equals:

$$H_q(s) = \frac{- \frac{\xi_q(L_c) \mathcal{L}^*}{M_q^*} s^2 - \frac{c l_t^2 \xi_q(L_c)^2}{M_q^*} s - \frac{k l_t^2 \xi_q(L_c)^2}{M_q^*}}{s^2 + \left( \frac{c}{\rho I_p} + \frac{c l_t^2 \xi_q(L_c)^2}{M_q^*} \right) s + \left( \omega_q^2 + \frac{k l_t^2 \xi_q(L_c)^2}{M_q^*} \right)} \quad (4.26)$$

and the measured torsion  $\psi^t(L_c, t)$  is given as:

$$\psi^t(L_c, t) = \left( \sum_{q=1}^{\infty} H_q(s) + 1 \right) \psi_{in}(t). \quad (4.27)$$

In case that the cantilever is driving at its first torsional resonance frequency, ( $q = 1$ ) the transfer function  $H^t(s) = \frac{\psi^t(L_c, s)}{\psi_{in}(s)}$  equals to:

$$H^t(s) = \frac{\left( 1 - \frac{\xi_1(L_c) \mathcal{L}^*}{M_1^*} \right) s^2 + \frac{c}{\rho I_p} s + \omega_1^2}{s^2 + \left( \frac{c}{\rho I_p} + \frac{c l_t^2 \xi_1(L_c)^2}{M_1^*} \right) s + \left( \omega_1^2 + \frac{k l_t^2 \xi_1(L_c)^2}{M_1^*} \right)} \quad (4.28)$$

leading to the ordinary differential equation:

$$\begin{aligned} \ddot{\psi}^t(L_c, t) + \left( \frac{c}{\rho I_p} + \frac{c l_t^2 \xi_1(L_c)^2}{M_1^*} \right) \dot{\psi}^t(L_c, t) + \left( \omega_1^2 + \frac{k l_t^2 \xi_1(L_c)^2}{M_1^*} \right) \psi^t(L_c, t) = \\ \left( 1 - \frac{\xi_1(L_c) \mathcal{L}^*}{M_1^*} \right) \ddot{\psi}_{in}(t) + \frac{c}{\rho I_p} \dot{\psi}_{in}(t) + \omega_1^2 \psi_{in}(t) \end{aligned} \quad (4.29)$$

Introducing (A.27)-(A.30) in (4.29) results in:

$$\begin{aligned} \ddot{\psi}^t(L_c, t) + \left( \frac{c}{\rho I_p} + \frac{2c l_t^2}{\rho I_p L_c} \right) \dot{\psi}^t(L_c, t) + \left( \omega_1^2 + \frac{2k l_t^2}{\rho I_p L_c} \right) \psi^t(L_c, t) = \\ \left( 1 - \frac{2}{\beta_q L_c} \right) \ddot{\psi}_{in}(t) + \frac{c}{\rho I_p} \dot{\psi}_{in}(t) + \omega_1^2 \psi_{in}(t) \end{aligned} \quad (4.30)$$

#### 4. FAULT DETECTION AND DIAGNOSIS APPLIED IN MICROELECTROMECHANICAL SYSTEMS

---

or in a more compact form,

$$\ddot{\psi}^t(L_c, t) + C_\psi \dot{\psi}^t(L_c, t) + K_\psi \psi^t(L_c, t) = \left(1 - \frac{2}{\beta_q L_c}\right) \ddot{\psi}_{in}(t) + \frac{c}{\rho I_\rho} \dot{\psi}_{in}(t) + \omega_1^2 \psi_{in}(t) \quad (4.31)$$

with

$$C_\psi = \frac{c}{\rho I_\rho} + \frac{2c_l l_t^2}{\rho I_\rho L_c}, \quad (4.32)$$

$$K_\psi = \omega_1^2 + \frac{2k_l l_t^2}{\rho I_\rho L_c}. \quad (4.33)$$

##### 4.3.2 Detection and Diagnosis of Tip-Fractures

During the characterization of the tribological phenomena of a rough surface, the damping coefficient of the dissipative shear force (lateral damping coefficient  $c_l$ ) varies slowly with respect to the surface slope [108]. At the same time, it has been observed that the radius of the tip's curvature also changes slowly during the scanning of the rough surface, while sudden tip's fractures may occur [109], [110]. Under the assumption of time varying lateral damping coefficient and tip's radius and taking into account that the TR-AFM is operating in the repulsive regime, the objective of this study is to capture and diagnose abrupt variations of the tip's radius.

The ordinary differential equation given in (4.31) is transformed into a linearly parametrizable model, described as:

$$\ddot{\psi}^t(L_c, i) - U(i) = [-\dot{\psi}^t(L_c, i) \quad -\psi^t(L_c, i)] \begin{bmatrix} C_\psi(i) \\ K_\psi(i) \end{bmatrix} \Rightarrow y(i) = \phi^T(i) \theta^\circ(i), \quad (4.34)$$

where  $U(i) = (1 - \frac{4}{\pi}) \ddot{\psi}_{in}(i) + \frac{\omega_1}{Q_c} \dot{\psi}_{in}(i) + \omega_1^2 \psi_{in}(i)$  and  $i$  denotes the sample instant with  $i \in [1, \dots, 10000]$ . Using (4.32), (4.33) and taking into account that  $k_l = 8G^* \sqrt{R_t} (\alpha_0 - \delta_0)$ , the components of the nominal parameter vector are described as:

$$\theta_1^\circ(i) = \frac{\omega_1}{Q_c} + \frac{2c_l(i) l_t^2}{\rho I_\rho L_c} = b_1^\circ + b_2^\circ c_l(i), \quad (4.35)$$

$$\theta_2^\circ(i) = \omega_1^2 + \frac{16G^* \sqrt{(\alpha_0 - \delta_0)} l_t^2}{\rho I_\rho L_c} \sqrt{R_t(i)} = b_3^\circ + b_4^\circ \sqrt{R_t(i)} \quad (4.36)$$

where  $Q_c$  is the quality factor of cantilever.

The simulation studies are performed with the following dimensional and material parameters:  $L_c = 252 \mu\text{m}$ ,  $b_c = 35 \mu\text{m}$ ,  $h_c = 2.3 \mu\text{m}$ ,  $\rho = 2330 \text{ kg/m}^3$ ,  $G = 50.78 \times \text{GPa}$ ,  $Q_c = 33.3$ . For the tip-sample interaction process, the related parameters are set  $H = 2.96 \times 10^{-19} \text{ J}$ ,  $G^* = 4.2 \text{ GPa}$ ,  $a_0 = 0.38 \text{ nm}$  and  $\delta_0 = 0.375 \text{ nm}$ . The dual piezo-elements are vibrated at cantilever's fundamental resonance frequency  $\omega_1$  and the amplitude of the support torsion of the equals to  $\psi_0 = 5 \mu\text{rad}$ . The tip's length

### 4.3 Torsional Resonant Atomic Force Microscope

is  $l_t = 12.5 \mu\text{m}$ , the initial nominal value of the tip curvature is  $R_t(0) = 10 \text{ nm}$  and the damping coefficient  $c_l(0) = 8 \times 10^{-7} \text{ Kgr/sec}$ .

The observed data records  $\psi^m(i)$  ( $\mu\text{rad}$ ),  $\dot{\psi}^m(i)$  ( $\frac{\mu\text{rad}}{\mu\text{sec}}$ ),  $\ddot{\psi}^m(i)$  ( $\frac{\mu\text{rad}}{\mu\text{sec}^2}$ ) are described as  $\psi^m(i) = \psi^t(L_c, i) + e_1(i)$ ,  $\dot{\psi}^m(i) = \dot{\psi}^t(L_c, i) + e_2(i)$ ,  $\ddot{\psi}^m(i) = \ddot{\psi}^t(L_c, i) + e_3(i)$ , where  $e_q(i)$ ,  $q = 1, 2, 3$  are bounded measurement noises and their bounds  $e_q^{\max}$  are computed taking into account SNR=55dB. The observed model output and regression vector are  $y^m(i) = \ddot{\psi}^m(i) - U(i)$  and  $\phi^m(i) = [-\dot{\psi}^m(i), -\psi^m(i)]^T$ , respectively.

Because of the roughness of the sample surface, it is also assumed that  $c_l$  and  $R_t$  vary as:

$$\begin{aligned} c_l(i) &= c_l(i-1) + w_{c_l}(i), \quad |w_{c_l}(i)| \leq \underbrace{0.0005c_l(0)}_{w_{c_l}^{\max}} \\ R_t(i) &= R_t(i-1) + w_{R_t}(i), \quad 0 \leq w_{R_t}(i) \leq \underbrace{0.0001R_t(0)}_{w_{R_t}^{\max}}. \end{aligned} \quad (4.37)$$

It is also assumed that despite any parameter perturbation or fault, the safe operation bounds of  $c_l(i)$  and  $R_t(i)$  are  $c_l(i) \in [c_l^{\min}, c_l^{\max}] = [4 \times 10^{-7} \text{Nsec/m}, 12 \times 10^{-7} \text{Nsec/m}]$  and  $R_t(i) \in [R_t^{\min}, R_t^{\max}] = [10 \text{nm}, 30 \text{nm}]$ ,  $\forall i$ . The safe operation parameter bounds of  $\theta_1^\circ(i), \theta_2^\circ(i)$  are defined as  $[\theta_1^{\min}, \theta_1^{\max}] = [b_1^\circ + b_2^\circ c_l^{\min}, b_1^\circ + b_2^\circ c_l^{\max}]$  and  $[\theta_2^{\min}, \theta_2^{\max}] = [b_3^\circ + b_4^\circ \sqrt{R_t^{\min}}, b_3^\circ + b_4^\circ \sqrt{R_t^{\max}}]$ , respectively. The parameter perturbations that influences  $c_l(i)$ ,  $R_t(i)$  are reflected to  $\theta_1^\circ(i)$ ,  $\theta_2^\circ(i)$ , so  $\theta_q^\circ(i) = \theta_q^\circ(i-1) + w_{\theta_q}(i)$ ,  $q = 1, 2$  with

$$|w_{\theta_1}(i)| = |b_2^\circ w_{c_l}(i)| \leq b_2^\circ w_{c_l}^{\max} \quad (4.38)$$

$$\begin{aligned} w_{\theta_2}(i) &= b_4^\circ \left( \sqrt{R_t(i)} - \sqrt{R_t(i-1)} \right) = b_4^\circ \left( \frac{R_t(i) - R_t(i-1)}{\sqrt{R_t(i)} + \sqrt{R_t(i-1)}} \right) \\ &\in \left[ 0, \frac{b_4^\circ w_{R_t}^{\max}}{2\sqrt{R_t^{\min}}} \right]. \end{aligned} \quad (4.39)$$

Under the previous assumptions, the objective of this study is to capture tip's fractures at the time instances  $i^{f1} = 3501$  and  $i^{f2} = 6501$ , which are quantified as  $R_t(i^{f1}) = R_t(i^{f1} - 1) + w_{R_t}(i^{f1}) + 0.4R_t(i^{f1} - 1)$  and  $R_t(i^{f2}) = R_t(i^{f2} - 1) + w_{R_t}(i^{f2}) + 0.25R_t(i^{f2} - 1)$ , applying the following FDD schemes:

- (A) FDD based on orthotopic SMI using data-hyperstrips,
- (B) FDD based on orthotopic SMI using data-hypersectors,
- (C) FDD based on ellipsoidal SMI using data-hyperstrips,
- (D) FDD based on ellipsoidal SMI using data-hypersectors,

#### 4. FAULT DETECTION AND DIAGNOSIS APPLIED IN MICROELECTROMECHANICAL SYSTEMS

---

where the **data-hyperstrips** are generated according to

$$S^p(i) = \{ \theta : y^m(i) - \tilde{e}^{\max}(i) \leq \phi^m(i)^T \theta \leq \tilde{y}^m(i) + \tilde{e}^{\max}(i) \}, \quad (4.40)$$

$$\tilde{e}^{\max}(i) = e_3^{\max} + e_2^{\max} \max \left( \left| \hat{\theta}_{z_1}^-(i) \right|, \left| \hat{\theta}_{z_1}^+(i) \right| \right) + e_1^{\max} \max \left( \left| \hat{\theta}_{z_2}^-(i) \right|, \left| \hat{\theta}_{z_2}^+(i) \right| \right) \quad (4.41)$$

with  $Z_u = \Omega_u$  in case of orthotopic SMI-based FDD or  $Z_u = \Omega_u^{\ominus}$  in case of ellipsoidal SMI-based FDD,  $u = 1, 2$ , and the **data-hypersectors** are generated according to

$$S^{np}(i) = \left\{ \theta : y^m(i) - e_3^{\max} \leq \phi^A(i)^T \theta \text{ and } \phi^B(i)^T \theta \leq y^m(i) + e_3^{\max} \right\}, \quad (4.42)$$

where  $\phi^A(i)$ ,  $\phi^B(i)$  are described by (2.42) and (2.43) with  $\text{sgn}(\theta_1^\circ) = \text{sgn}(\theta_2^\circ) = 1$  since  $\theta_1^{\min}, \theta_2^{\min} > 0$ , resulting in

$$\phi^A(i) = \left[ \phi_1^m(i) + e_2^{\max} \quad \phi_2^m(i) + e_1^{\max} \right]^T, \quad (4.43)$$

$$\phi^B(i) = \left[ \phi_1^m(i) - e_2^{\max} \quad \phi_2^m(i) - e_1^{\max} \right]^T. \quad (4.44)$$

The abrupt parameter variations of tip's radius are detected by all FDD schemes, with the time instances of fault detection presented in Table 4.4. As observed, the time instances of fault detection determined by the orthotope-based FDD schemes ((A),(B)) coincide with the time instances of fault occurrence. On the other hand, there is a delay between the time instances of fault detection using the ellipsoid-based FDD schemes ((C),(D)) and the time instances of fault occurrence. The fault

**Table 4.4:** TR-AFM–Time Instances of Fault Occurrence and Detection

$j$	$i^{fj}$	(A)&(B)- $i^{dj}$	(C)&(D)- $i^{dj}$
1	3501	3501	3519
2	6501	6501	6518

detection mechanism is followed by the resetting procedure, which is implemented according to Theorem 3.4.1 in the orthotopic FDD schemes and Theorem 3.4.2 in ellipsoidal FDD schemes. It has to be mentioned that despite the delay in detecting the faults using the ellipsoid-based FDD schemes, the varied parameter vector is captured within the ellipsoid computed by the applied resetting procedure.

Figures 4.9 and 4.10 present the nominal values of  $\theta_u^\circ(i)$  (cyan line) and the upper [lower] bounds (A)– $\theta_{\Omega_u}^+(i)$  [ $\theta_{\Omega_u}^-(i)$ ] ((black)–dashed [solid] line), (B)– $\theta_{\Omega_u}^+(i)$  [ $\theta_{\Omega_u}^-(i)$ ] ((red)–dashed [solid] line), (C)– $\theta_{\Omega_u^\ominus}^+(i)$  [ $\theta_{\Omega_u^\ominus}^-(i)$ ] ((blue)–dashed [solid] line), (D)– $\theta_{\Omega_u^\ominus}^+(i)$  [ $\theta_{\Omega_u^\ominus}^-(i)$ ] ((green)–dashed [solid] line),  $u = 1, 2$ . The time instances of fault occurrence  $i^{fj}$  are shown on the horizontal axis of these figures.

It is apparent from the previous diagrams that there is a very small difference between the upper and lower bounds produced by (A) and (B) (also (C) and

### 4.3 Torsional Resonant Atomic Force Microscope

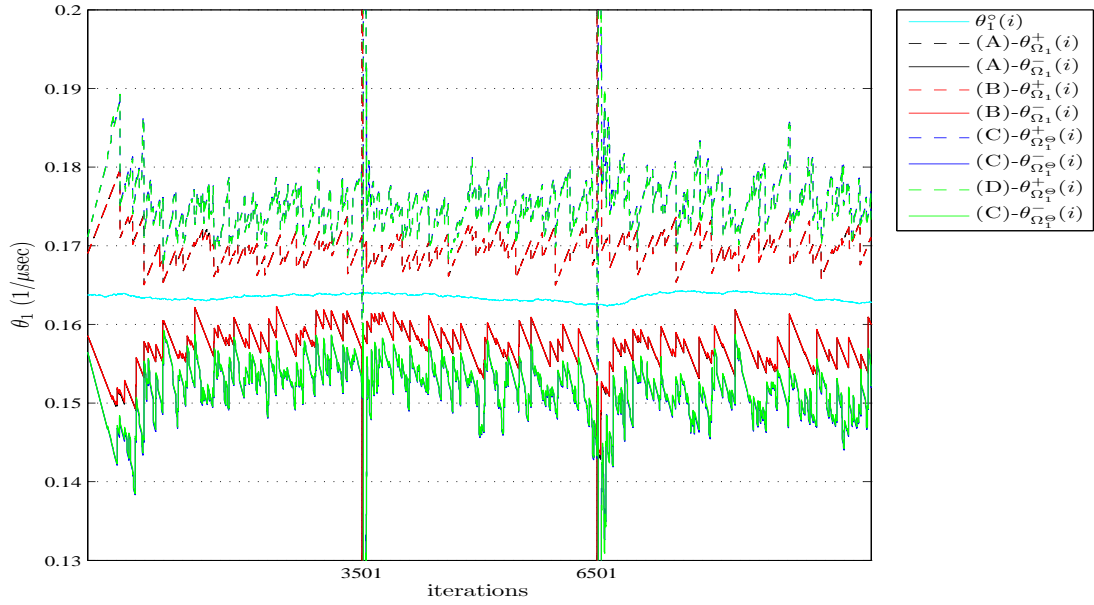


**Figure 4.9:** TR-AFM–Time evolution of upper and lower bounds of  $\theta_1^0$  generated by the FDD schemes.

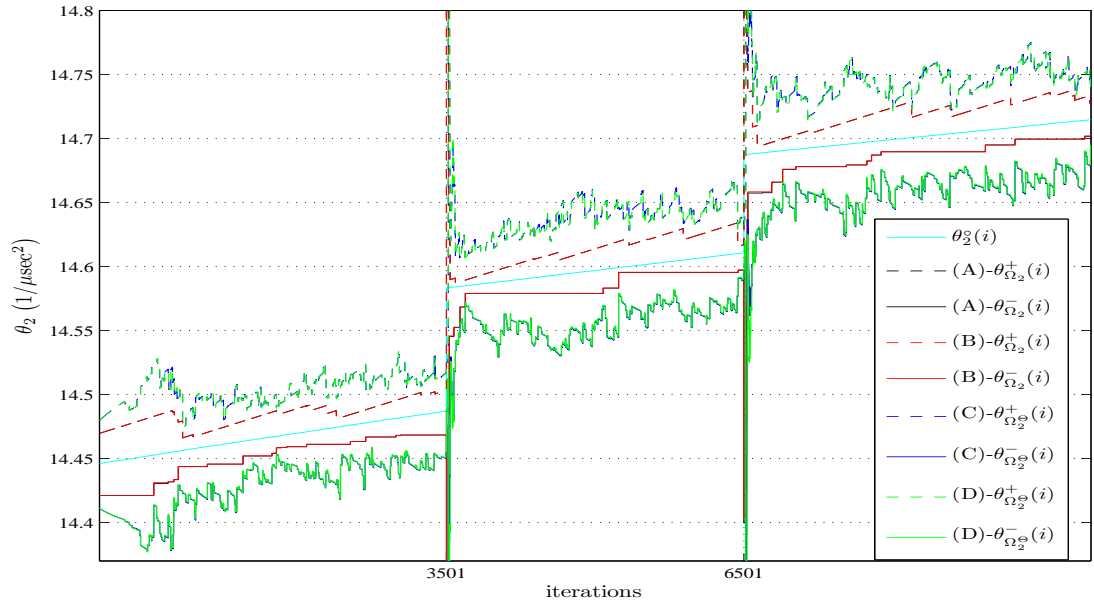


**Figure 4.10:** TR-AFM–Time evolution of upper and lower bounds of  $\theta_2^0$  generated by the FDD schemes.

#### 4. FAULT DETECTION AND DIAGNOSIS APPLIED IN MICROELECTROMECHANICAL SYSTEMS

(D)). Moreover, the upper and lower bounds generated by the orthotope-based FDD schemes are tighter than the ones generated by the ellipsoid-based FDD schemes. This fact in combination with the difference between the fault detection instances inferred by the orthotope and ellipsoid based FDD schemes, as shown in Table 4.4, seems to stem from the fact that the perturbation orthotope  $\Omega^w$  used for computing the augmented orthotope  $\hat{\Omega}(i)$  is smaller than the perturbation ellipsoid  $\Theta^w$  ( $\Theta^w \supset \Omega^w$ ) used for computing the augmented ellipsoid  $\hat{\Theta}(i)$ .

The fault isolation mechanism is implemented as described in Sections 3.4.1.1 and 3.4.1.2. Figures 4.11 and 4.12 present the nominal values of  $\theta_u^\circ(i)$ ,  $u = 1, 2$  and the upper and lower bounds generated by the (B) and (D) FDD schemes (the parameter bounds produced by (A) and (C) schemes are omitted for simplicity) and the worst-case upper and lower bounds corresponding to the maximum and minimum values of the projection  $\hat{\Omega}_u(i|i^{d_j} - 1)$  and  $\hat{\Omega}_u^\Theta(i|i^{d_j} - 1)$ ,  $j = 1, 2$ , defined in (3.34) and (3.36), respectively.

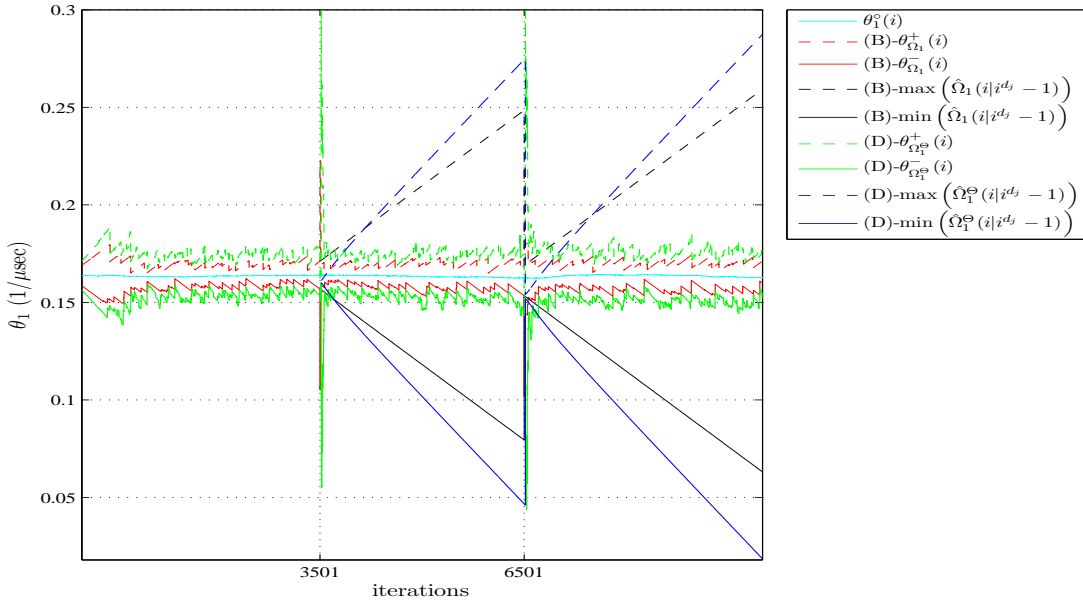


**Figure 4.11:** TR-AFM–Fault detection of  $\theta_1^\circ(i)$  applying (B) and (D) FDD schemes.

Using the (B) FDD scheme, the first component of parameter vector is inferred as non-faulty for the time windows  $[3514, 6500]$  and  $[6559, 10000]$ , while using the (D) FDD scheme, it is inferred as non-faulty for the time windows  $[3759, 3845] \cup [3870, 6517]$  and  $[6924, 10000]$ . Using the (B) FDD scheme, the second component of parameter vector is characterized as faulty for the time windows  $[3529, 6500]$  and  $[6534, 10000]$ , except from the time interval  $[9914, 9937]$ , in which its status is undefined. Using the (D) scheme there are a number of time windows between  $[3518, 6517]$  and  $[6519, 10000]$  for which the second component of parameter vector is inferred as



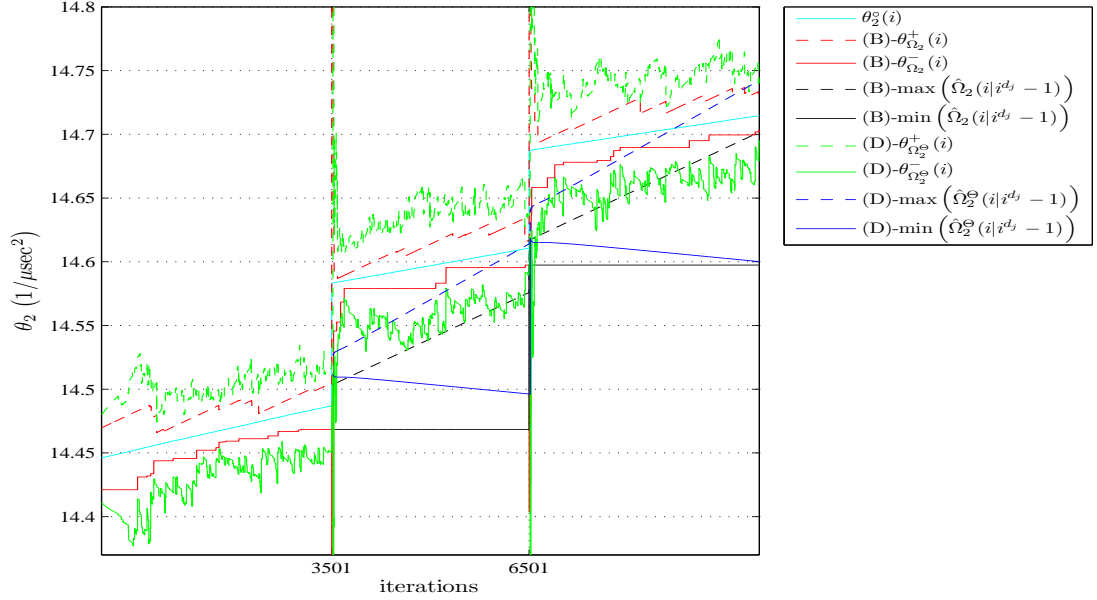


**Figure 4.12:** TR-AFM-Fault detection of  $\theta_2^o(i)$  applying (B) and (D) FDD schemes.

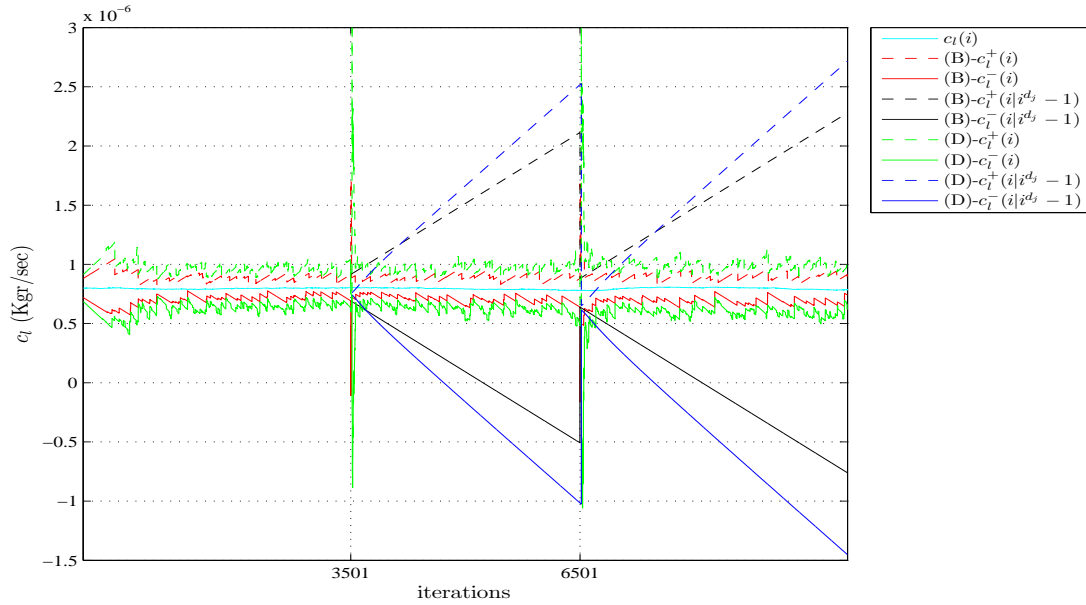
non-faulty. The earliest time instant that  $\theta_2(i)$  is inferred as faulty within the time window  $[3518, 6517]$  is  $i = 3592$ , while within the time window  $[6519, 10000]$  it is  $i = 6795$ .

Figure 4.13 presents the nominal values of  $c_l(i)$  (cyan line), the estimated bounds (B)[(D)]- $c_l^+(i)$ , (B)[(D)]- $c_l^-(i)$  (red [green]-dashed, solid lines) and the worst-case bounds (B)[(D)]- $c_l^+(i|i^{d_j}-1)$ , (B)[(D)]- $c_l^-(i|i^{d_j}-1)$  (black [blue]-dashed, solid lines) computed after the application of interval arithmetic to parameter bounds (B)[(D)]- $\theta_{\Omega_1}^+(i)$ , (B)[(D)]- $\theta_{\Omega_1}^-(i)$  and the projection  $\hat{\Omega}_1(i|i^{d_j}-1)$  [ $\hat{\Omega}_1^o(i|i^{d_j}-1)$ ],  $j = 1, 2$ , respectively, taking into account (4.35).

Similarly, Fig. 4.14 presents the nominal values of  $R_t(i)$  (cyan line), the estimated bounds (B)[(D)]- $R_t^+(i)$ , (B)[(D)]- $R_t^-(i)$  (red [green]-dashed, solid lines) and the worst-case bounds (B)[(D)]- $R_t^+(i|i^{d_j}-1)$ , (B)[(D)]- $R_t^-(i|i^{d_j}-1)$  (black [blue]-dashed, solid lines) computed after the application of interval arithmetic to parameter bounds (B)[(D)]- $\theta_{\Omega_2}^+(i)$ , (B)[(D)]- $\theta_{\Omega_2}^-(i)$  and the projection  $\hat{\Omega}_2(i|i^{d_j}-1)$  [ $\hat{\Omega}_2^o(i|i^{d_j}-1)$ ],  $j = 1, 2$ , respectively, taking into account (4.36).

The lateral damping coefficient  $c_l$  and the tip's radius  $R_t$  are characterized as non-faulty and faulty, respectively within the time intervals that  $\theta_1, \theta_1$  are characterized as non-faulty and faulty, respectively.

#### 4. FAULT DETECTION AND DIAGNOSIS APPLIED IN MICROELECTROMECHANICAL SYSTEMS



**Figure 4.13:** TR-AFM-Fault detection and isolation of  $c_l(i)$  applying (B) and (D) FDD schemes.

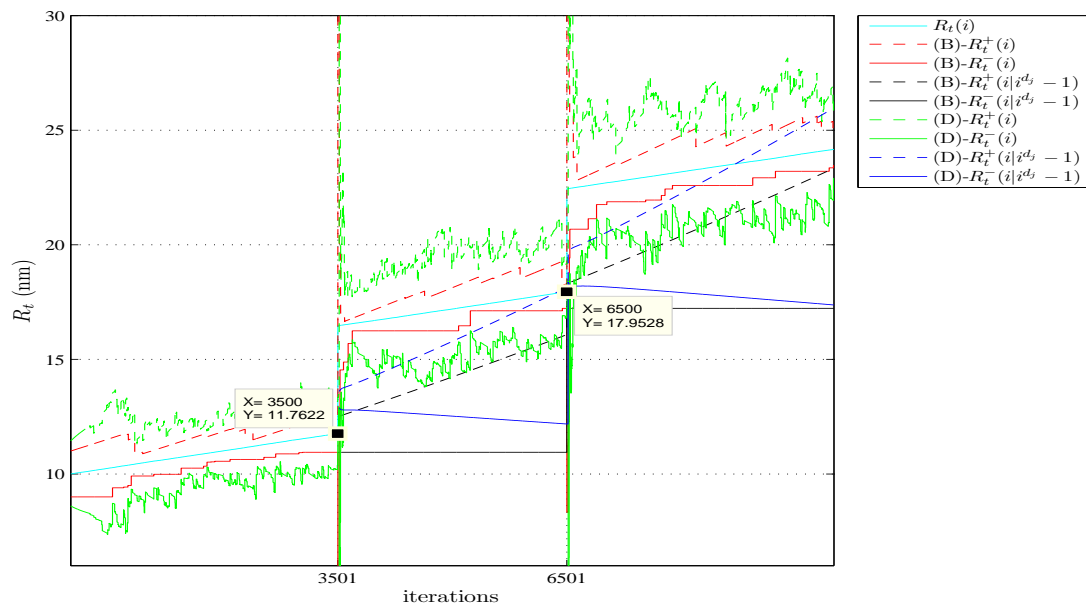


**Figure 4.14:** TR-AFM-Fault detection and isolation of  $R_t(i)$  applying (B) and (D) FDD schemes.

The estimation of the variation of  $R_t$  is shown in Fig. 4.15, computed as

$$\tilde{d}_{R_t}(i) = \frac{R_t^+(i) + R_t^-(i)}{2} - \frac{R_t^+(i|i^{d_j} - 1) + R_t^-(i|i^{d_j} - 1)}{2} \quad (4.45)$$

for  $i \in [3529, 6500]$  and  $[6534, 10000]$  in the (B)-FDD scheme and for  $i \in [3592, 6517]$  and  $[6795, 10000]$  in the (D)-FDD scheme. The nominal values of parameter variation  $0.4R_t(i^{f_1} - 1)$  and  $0.25R_t(i^{f_2} - 1)$  are indicated in the vertical axis, while the time instances of fault occurrence are indicated in the horizontal axis. It is observed that there is a divergence of the the estimated variation of  $R_t$  arisen from the (D)-scheme and its nominal value. This divergence is probably due to the delay in detecting the faults by the (D) scheme, leading to the computation of parametric sets that do not contain the nominal vector  $\theta^\circ(i)$  for  $i \in [3501, 3518]$  and  $[6501, 6517]$ .

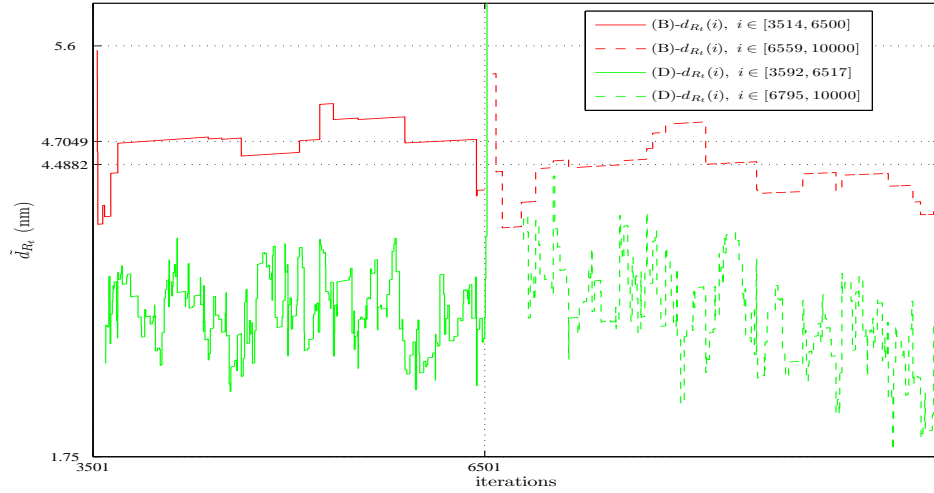


Figure 4.15: TR-AFM–Fault identification of  $R_t(i)$  applying (B) and (D) FDD schemes.

## 4.4 Conclusions

In this chapter, simulation studies are offered for verifying the efficiency of the SMI-based FDD methodology, applied in an electrostatic parallel-plate microactuator and a torsionally resonant atomic force microscope. In both examples, four different schemes are used for the implementation of the FDD procedure, relying on orthotopic and ellipsoidal SMI with data-hyperstrips and data-hypersectors. In the microactuator example, under the assumption of a time-invariant linearly parametrizable model, multiple abrupt variations in its mass, spring stiffness and damping coefficient are detected by the FDD-schemes at the same time instances. The FDD schemes based on ellipsoidal SMI isolate earlier the faulty components than the orthotopic SMI

#### 4. FAULT DETECTION AND DIAGNOSIS APPLIED IN MICROELECTROMECHANICAL SYSTEMS

---

based ones. In the TR-AFM example, under the assumption of a time-varying linearly parametrizable model, the FDD schemes based on orthotopic SMI capture the abrupt tip's fractures earlier than the ones based on ellipsoidal SMI based FDD schemes. The faulty component (tip's radius) is isolated by the FDD schemes, but the delay in fault detection using the ellipsoidal SMI ones seems to affect the fault identification procedure.

## Chapter 5

# Concluding Remarks

### 5.1 Conclusions

The objective of this dissertation is the development of a fault detection and diagnosis (FDD) methodology and its application in microelectromechanical systems (MEMS). The need for utilizing a FDD module in complex systems stems from the fact that faults must be captured and diagnosed before being compensated for ensuring system reliability, maintainability and safe operation. These requirements are very important especially in MEMS, whose improper operation may have a profound impact in production cost and product quality, or even cause severe consequences in human safety, since they are embedded in devices used in medicine, avionics, vehicles e.t.c.

The goal of the proposed FDD methodology is to capture, isolate and identify multiple abrupt parametric faults. Its design relies on parameter estimation in a set membership framework under the assumption of a linearly parametrizable model and the a priori knowledge of the bounds of the noise errors and parameter perturbations. The basic task of the set membership identification (SMI) is the determination of the feasible parameter set within which the nominal parameter vector resides. Due to the difficulty in computing the feasible parameter set, orthotopes and ellipsoids that outer bound it are used. Their mathematical expression is simpler and they can be computed in an optimal way. Consequently, the goal of SMI is reformulated in order to compute the orthotope or ellipsoid that guarantees to contain the nominal parameter vector. This is accomplished given that the nominal parameter vector resides in a hyperspace generated by the measurement data and the a priori known noise bounds, which always intersects with the computed orthotope or ellipsoid under faultless conditions. This data-hyperspace is depicted as: a) a data-hyperstrip, which is the hyperspace between two parallel hyperplanes, and b) a data-hypersector, defined by two non parallel hyperplanes. The former configuration presupposes the utilization of parameter bounds, while the latter one demands

## 5. CONCLUDING REMARKS

---

the a priori known signed parameter vector. In this dissertation, an orthotope-based SMI algorithm is developed handling both data-hyperstrips and hypersectors and is implemented using linear programming techniques. On the other hand, the Optimal Volume Ellipsoid (OVE) algorithm is used for the recursive computation of the ellipsoid taking into account data-hyperstrips and is properly modified in order to handle data-hypersectors.

In this research work, the FDD procedure is performed using a jump linearly parametrizable model, in which the parameter variation vector is incorporated. The jump-nature of the system description implies that the parameter variation vector remains constant for a time window after the fault occurrence. The fault detection is achieved when the normal operation of the SMI is violated, due to an empty intersection between the data-hyperspace and the estimated parametric set. In order to proceed with the fault diagnosis, a seamless update in SMI algorithm is realized by resetting the parametric set and the data-hyperspace ensuring that their intersection is non-empty and contains the new nominal parameter vector. The fault isolation is carried out by checking the intersection between the projection of the estimated parameter set arisen from the normal operation of SMI and the projection of the worst case parameter set within which the nominal parameter vector would have resided, if no fault had occurred. A faulty component is indicated when this intersection is empty, and the size and type of the parameter variation is computed using the distance of the projections' centers. If the FDD procedure is implemented using the ellipsoidal SMI and under the assumption of time-invariant parameter vector, a new fault detection criterion is defined based on the intersection of the support orthotopes of ellipsoids and is activated when this intersection is empty. In this dissertation, a more accurate estimation of the time instant of fault occurrence is proposed, along with a backward-in-time procedure starting from the fault detection instant, while the conditions under which a fault will never be detected by the orthotopic and ellipsoidal SMI based FDD are provided.

Simulation studies are elaborated in order to verify the efficiency of the SMI-based FDD methodology, applied in an electrostatic parallel-plate microactuator and a torsionally resonant atomic force microscope (TR-AFM). Orthotopic and ellipsoidal SMI-based schemes handling data-hypersectors and data-hyperstrips are used for the implementation of the FDD procedure, aiming at detecting failure modes appeared in these systems. In the first example, under the assumption of a time-invariant linearly parametrizable model, abrupt parameter variations in the mass, spring stiffness and damping coefficient of the microactuator are detected and diagnosed by the proposed schemes, while the faulty components are isolated earlier in the ellipsoidal FDD schemes. In the TR-AFM example, the lumped parameter modelling is necessary in order to obtain a linearly parametrizable model. Then, under the assumption of a time-varying linearly parametrizable model, tip's fractures corresponding to abrupt variations of tip's radius are detected and diagnosed by the orthotopic FDD

schemes, while a delay is observed in the ellipsoidal FDD schemes, affecting the fault identification mechanism.

## 5.2 Areas for Further Research

While there are many directions towards which this research could turn, there are a few areas which seem particularly promising. In Chapter 2, the orthotopic and ellipsoidal SMI algorithms are developed using the two configurations of data-hyperspace. These algorithms could be modified taking into account the intersection of the data-hyperstrips and the data-hypersectors. An alternative approach would be the parallel operation of the algorithms using data-hypersectors and data-hyperstrips and the selection of the smallest generated parametric set.

The suggested FDD methodology aims at the detection of multiple parametric faults. Future work could include the customization of the FDD methodology in order to detect additive faults as defined in Chapter 1 [71]. Further on, taking into account that both multiplicative and additive faults may occur in the system under investigation, consistency tests could be defined for identifying the type of the fault. The FDD methodology is developed under the assumption of a linearly parametrizable model with  $y(i) \in \mathbb{R}$  and  $\phi(i) \in \mathbb{R}^n$ . The FDD procedure may be extended in order to encounter a linearly parametrizable model with  $y(i) \in \mathbb{R}^{r \times 1}$  and  $\phi(i) \in \mathbb{R}^{r \times n}$  [111].

At the end of Chapter 3, there is a discussion concerning the detectability of the faults and the characterization of the algorithms in relation to the inherent SMI assumptions. Certainly, a sensitivity analysis of the proposed methods could be conducted, by systematically checking whether or not a fault can be detected after applying a range of input stimuli, noise bounds, parameter perturbation bounds e.t.c. A research work related to sensitivity analysis is presented in [100], in which the output envelope detection of microsprints' cracks in a microelectromechanical system is investigated using a range of input stimuli and generating random perturbations in electronics.

Simulation results presented in [103], [89] indicate the capability of the FDD procedure based on SMI in capturing faults appeared in an electrostatic parallel-plate microactuator operating in a closed-loop configuration. However, the information generated by closed-loop systems could be easily defective and the loss of identifiability may be raised as shown in [112]. Hence, since the FDD procedure relies on an identification technique, it would be worthwhile to explore the detectability of the faults using different types of controllers.

Simulation studies in Chapter 4 indicate a good performance of the proposed FDD methodology in detecting failure modes in an electrostatic parallel-plate microactuator and a torsionally-resonant atomic force microscope. However, the experimental verification of the efficiency of the FDD algorithms applied in a real MEMS setup

## 5. CONCLUDING REMARKS

---

is necessary. The FDD procedure should be customized so as to overcome difficulties arisen from the experimental conditions such as limited or non informative data, unknown disturbances that cannot be modelled and incorporated in a linearly parametrizable model, high-magnitude measurement noise, high sampling rates that lead to information losses e.t.c.

### 5.3 Dissertation Publications

The following articles appeared as a result of the research work in this dissertation.

#### Journal Publications

- J.1 V. Reppa and A. Tzes, *Fault Detection and Diagnosis based on Parameter Set estimation*, to appear in IET Journal of Control Theory and Applications.

#### Conference Publications

- C.1 V. Reppa and A. Tzes, *Fault Detection and Diagnosis relying on Set Membership Identification for Time Varying Systems*, Conference on Control and Fault-Tolerant Systems, Nice, France, 2010 (to appear, Paper FrA1.2).
- C.2 V. Reppa, M. Vagia and A. Tzes, *Fault Detection and Diagnosis enhanced by a Reconfiguration Control Scheme for a Micro-Electrostatic Actuator*, in Proceedings of the 18th Mediterranean Conference on Control and Applications, Marrakech, Morocco, 2010, pp. 477-482.
- C.3 V. Reppa and A. Tzes, *Fault Detection and Diagnosis based on Parameter Set Estimation for Measurements corrupted by Bounded Noise*, in Proceedings of the 18th Mediterranean Conference on Control and Applications, Marrakech, Morocco, 2010, pp. 460-465.
- C.4 V. Reppa and A. Tzes, *Fault Detection relying on Set Membership Techniques for an Atomic Force Microscope*, in Proceedings of the 7th IFAC Symposium on Fault Detection, Supervision and Safety on Technical Processes (SAFEPROCESS), Barcelona, Spain, 2009, pp. 1186-1191
- C.5 V. Reppa and A. Tzes, *Fault Detection based on Orthotopic Set Membership Identification for Robot Manipulators*, in Proceedings of the 17th IFAC World Congress, Seoul, Korea, 2008, pp. 7344-7349
- C.6 V. Reppa, M. Vagia and A. Tzes, *Fault Detection using Set Membership Identification for Micro-Electrostatic Actuators*, in Proceedings of IEEE International Conference on Control Applications, Singapore, 2007, pp. 789-794
- C.7 V. Reppa and A. Tzes, *Synergy between control and electronic simulation models in performance system enhancement*, in Proceedings of IEEE International Conference on Control Applications, Singapore, 2007, pp. 1138-1143



- C.8 V. Reppa and A.Tzes , *Application of Set Membership Identification for Fault Detection of MEMS* in Proceedings of the IEEE International Conference on Robotics and Automation (ICRA 06), Orlando, Florida, 2006, pp. 643-648

## 5. CONCLUDING REMARKS

---

# Bibliography

- [1] R. Isermann, *Fault-diagnosis systems: an introduction from fault detection to fault tolerance*. Springer Verlag, 2006.
- [2] IFAC Technical Committee on Fault Detection, Supervision and Safety for Technical Processes, TC 6.4-Terminology. [Online]. Available: <http://www.safeprocess.es.aau.dk/index.php?id=9033>
- [3] R. Isermann and P. Balle, "Trends in the application of model-based fault detection and diagnosis of technical processes," *Control Eng. Pract.*, vol. 5, no. 5, pp. 709–719, 1997.
- [4] J. Gertler, *Fault detection and diagnosis in engineering systems*. Marcel Dekker, New York, 1998.
- [5] J. Chen and R. Patton, *Robust model-based fault diagnosis for dynamic systems*. Kluwer Academic Publishers Norwell, MA, USA, 1999.
- [6] S. Ding, *Model-based fault diagnosis techniques: design schemes, algorithms, and tools*. Springer Verlag, 2008.
- [7] M. Basseville and I. Nikiforov, *Detection of abrupt changes: Theory and application*. Prentice Hall Inc, 1993.
- [8] C. Jiang and D. Zhou, "Fault detection and identification for uncertain linear time-delay systems," *Computers and Chemical Engineering*, vol. 30, no. 2, pp. 228–242, 2004.
- [9] P. Smith, C. Furse, and J. Gunther, "Analysis of spread spectrum time domain reflectometry for wire fault location," *IEEE Sensors Journal*, vol. 5, no. 6, pp. 1469–1478, 2005.
- [10] I. Izadi, S. Shah, D. Shook, and T. Chen, "An Introduction to Alarm Analysis and Design," in *Proceedings of the 7th IFAC Symposium on Fault Detection, Supervision and Safety of Technical Processes*, Barcelona, Spain, 2009, pp. 645–650.
- [11] K. Huang and N. EvaWu, "Change Detection for the NASA Generic Transport Aircraft Model," in *Proceedings of the 7th IFAC Symposium on Fault Detection, Supervision and Safety of Technical Processes*, Barcelona, Spain, 2009, pp. 277–282.
- [12] Y. Tharrault, G. Mourot, and J. Ragot, "WWTP diagnosis based on robust principal component analysis," in *Proceedings of the 7th IFAC Symposium on Fault Detection, Supervision and Safety of Technical Processes*, Barcelona, Spain, 2009, pp. 1342–1347.
- [13] J. Vanlaer, G. Gins, and J. Van Impe, "Comparison of MPCAV, ARPCA, and BDPCA fault detection performance in a fed-batch penicillin fermentation process," in *Proceedings of the 7th IFAC Symposium on Fault Detection, Supervision and Safety of Technical Processes*, Barcelona, Spain, 2009, pp. 840–845.

## BIBLIOGRAPHY

---

- [14] W. Zanardelli, E. Strangas, and S. Aviyente, "Identification of Intermittent Electrical and Mechanical Faults in Permanent-Magnet AC Drives Based on Time-Frequency Analysis," *IEEE Transactions on Industry Applications*, vol. 43, no. 4, pp. 971–980, 2007.
- [15] F. Previdi and T. Parisini, "Model-free actuator fault detection using a spectral estimation approach: the case of the DAMADICS benchmark problem," *Control Engineering Practice*, vol. 14, no. 6, pp. 635–644, 2006.
- [16] M. Galvez-Carrillo and M. Kinnaert, "Fault detection and isolation in current and voltage sensors of doubly-fed induction generators," in *Proceedings of the 7th IFAC Symposium on Fault Detection, Supervision and Safety of Technical Processes*, Barcelona, Spain, 2009, pp. 1360–1365.
- [17] R. Isermann, "Model-based fault-detection and diagnosis—status and applications," *Annual Reviews in control*, vol. 29, no. 1, pp. 71–85, 2005.
- [18] S. Rajakarunakaran, P. Venkumar, D. Devaraj, and K. Rao, "Artificial neural network approach for fault detection in rotary system," *Applied Soft Computing Journal*, vol. 8, no. 1, pp. 740–748, 2008.
- [19] C. Edwards, S. Spurgeon, and R. Patton, "Sliding mode observers for fault detection and isolation," *AUTOMATICA OXFORD*, vol. 36, pp. 541–553, 2000.
- [20] G. Hendeby and F. Gustafsson, "Fundamental fault detection limitations in linear non-Gaussian systems," in *Proceedings of the 44th IEEE Conference on Decision and Control*, Seville, Spain, 2005, pp. 338–343.
- [21] J. Sakellariou and S. Fassois, "Vibration based fault detection and identification in an aircraft skeleton structure via a stochastic functional model based method," *Mechanical Systems and Signal Processing*, vol. 22, no. 3, pp. 557–573, 2008.
- [22] L. Hartert, M. Sayed Mouchaweh, and P. Billaudel, "Dynamic Fuzzy Pattern Matching for the monitoring of non stationary processes," in *Proceedings of the 7th IFAC Symposium on Fault Detection, Supervision and Safety of Technical Processes*, Barcelona, Spain, 2009, pp. 516–520.
- [23] V. Sugumaran, V. Muralidharan, and K. Ramachandran, "Feature selection using Decision Tree and classification through Proximal Support Vector Machine for fault diagnostics of roller bearing," *Mechanical Systems and Signal Processing*, vol. 21, no. 2, pp. 930–942, 2007.
- [24] S. Pirooz Azad, Bahrampour, B. S., Moshiri, and K. Salahshoor, "New Fusion Architectures for Performance Enhancement of a PCA-Based Fault Diagnosis and Isolation System," in *Proceedings of the 7th IFAC Symposium on Fault Detection, Supervision and Safety of Technical Processes*, Barcelona, Spain, 2009, pp. 852–857.
- [25] C. Isaza, A. Orantes, T. Kempowsky-Hamon, and M.-V. Le Lann, "Contribution of fuzzy classification for the diagnosis of complex systems," in *Proceedings of the 7th IFAC Symposium on Fault Detection, Supervision and Safety of Technical Processes*, Barcelona, Spain, 2009, pp. 1132–1139.
- [26] A. Barner, J. Bredau, and F. Schiller, "Efficient Fault Detection in Safety-related Pneumatic Control by Conceptual Encapsulation," in *Proceedings of the 7th IFAC Symposium on Fault Detection, Supervision and Safety of Technical Processes*, Barcelona, Spain, 2009, pp. 1168–1173.
- [27] E. Nemeth, R. Lakner, I. Cameron, and K. Hangos, "Fault diagnosis based on hazard identification results," in *Proceedings of the 7th IFAC Symposium on Fault Detection, Supervision and Safety of Technical Processes*, Barcelona, Spain, 2009, pp. 1515–1520.

- [28] R. Razavi-Far, H. Davilu, V. Palade, and L. Caro, "Neuro-Fuzzy based Fault Diagnosis of a Steam Generator," in *Proceedings of the 7th IFAC Symposium on Fault Detection, Supervision and Safety of Technical Processes*, Barcelona, Spain, 2009, pp. 1180–1185.
- [29] V. Puig, J. Quevedo, T. Escobet, and B. Pulido, "On the integration of fault detection and isolation in model-based fault diagnosis," in *Proceedings of the 16th International Workshop on Principles of Diagnosis (DX-05)*, Pacific Grove, CA, USA, 2005, pp. 227–232.
- [30] J. Meseguer, V. Puig, and T. Escobet, "Fault Diagnosis using a Timed Discrete Event Approach based on Interval Observers," in *Proceedings of the 17th IFAC World Congress*, Seoul, Korea, 2008, pp. 6914–6919.
- [31] D. Panescu, "Mems in medicine and biology," *IEEE Engineering in Medicine and Biology Magazine*, vol. 25, no. 5, pp. 19–28, 2006.
- [32] J. Leclerc, "Mems for aerospace navigation," *IEEE Aerospace and Electronic Systems Magazine*, vol. 22, no. 10, pp. 31–36, 2007.
- [33] N. de Rooij, S. Gautsch, D. Briand, C. Marxer, G. Mileti, W. Noell, H. Shea, U. Staufer, and B. van der Schoot, "Mems for space," in *Proceedings of the 15th International Conference on Solid-State Sensors, Actuators and Microsystems*, Denver, Colorado, USA, 2009, pp. 17–24.
- [34] J. Hilbert, "Rf-mems for wireless communications," *IEEE Communications Magazine*, vol. 46, no. 8, pp. 68–74, 2008.
- [35] J. Wang, G. Li, Y. Lu, X. Gao, Y. Zhang, and K. Tao, "Vehicle supervision system based on mems geomagnetic sensor," in *Proceedings of the 4th International Conference on Nano/Micro Engineered and Molecular Systems*, Shenzhen, China, 2009, pp. 331–334.
- [36] E. Eleftheriou, T. Antonakopoulos, G. Binnig, G. Cherubini, M. Despont, A. Dholakia, U. Durig, M. Lantz, H. Pozidis, H. Rothuizen, and P. Vettiger, "Millipede - a mems-based scanning-probe data-storage system," *IEEE Transactions on Magnetics*, vol. 39, no. 2, pp. 938–945, 2003.
- [37] D. Sahoo, W. Haberle, A. Sebastian, H. Pozidis, and E. Eleftheriou, "High-throughput intermittent-contact scanning probe microscopy," *Nanotechnology*, vol. 21, pp. 1–7, 2010.
- [38] Spengen, W. and Modlinski, R. and Puers, R. and Jourdain, A., "Failure mechanisms in mems/nems devices," in *Handbook of Nanotechnology*. Springer Verlag, 2007, pp. 1663–1684.
- [39] Y. Li and Z. Jiang, "An Overview of Reliability and Failure Mode Analysis of Microelectromechanical Systems (MEMS)," in *Handbook of Performability Engineering*. Springer London, 2008, pp. 953–966.
- [40] M. Dardalhon, V. Berouille, L. Latorre, P. Nouet, G. Perez, J. Nicot, and C. Oudea, "Reliability analysis of CMOS MEMS structures obtained by Front Side Bulk Micromachining," *Microelectronics reliability*, vol. 42, no. 9-11, pp. 1777–1782, 2002.
- [41] S. Lee, R. Ramadoss, M. Buck, V. Bright, K. Gupta, and Y. Lee, "Reliability testing of flexible printed circuit-based RF MEMS capacitive switches," *Microelectronics Reliability*, vol. 44, no. 2, pp. 245–250, 2004.
- [42] Z. Tao and B. Bhushan, "Surface modification of AFM silicon probes for adhesion and wear reduction," *Tribology Letters*, vol. 21, no. 1, pp. 1–16, 2006.
- [43] S. Mir, "Integrated circuit testing: From microelectronics to microsystems," in *Proceedings of the 5th IFAC Symposium on Fault detection, supervision and safety of technical processes*, Washington, DC, USA, 2003, pp. 13–24.

## BIBLIOGRAPHY

---

- [44] A. Kolpekwar, T. Jiang, and R. Blanton, "CARMEL: Contamination and reliability analysis of MicroElectromechanical layout," *Journal of Microelectromechanical Systems*, vol. 8, no. 3, pp. 309–318, 1999.
- [45] R. Rosing, A. Lechner, A. Richardson, and A. Dorey, "Fault simulation and modelling of micro-electromechanical systems," *Computing & Control Engineering Journal*, vol. 11, no. 5, pp. 242–250, 2000.
- [46] M. Lubaszewski, E. Cota, and B. Courtois, "Microsystems testing: an approach and open problems," in *Proceedings of the Design, Automation and Test in Europe*, Paris, France, 1998, pp. 524–529.
- [47] B. Caillard, Y. Mita, Y. Fukuta, T. Shibata, and H. Fujita, "A highly simple failure detection method for electrostatic microactuators: application to automatic testing and accelerated lifetime estimation," *IEEE Transactions on Semiconductor Manufacturing*, vol. 19, no. 1, pp. 35–42, 2006.
- [48] A. Dhayni, S. Mir, L. Rufer, A. Bounceur, and E. Simeu, "Pseudorandom BIST for test and characterization of linear and nonlinear MEMS," *Microelectronics Journal*, vol. 40, no. 7, pp. 1054–1061, 2009.
- [49] B. Charlot, S. Mir, F. Parrain, and B. Courtois, "Generation of electrically induced stimuli for MEMS self-test," *Journal of Electronic Testing*, vol. 17, no. 6, pp. 459–470, 2001.
- [50] R. Asgary and K. Mohammadi, "Initialized RHPNN for fault detection in MEMS," in *Proceedings of the 8th International Conference on Pattern Recognition and Information Processing*, Minsk, Russia, 2005, pp. 449–453.
- [51] J. Tanha and R. Asgary, "An Intelligent BIST Mechanism for MEMS Fault Detection," in *Proceedings of MEMSTECH 2007 International Conference on the Perspective Technologies and Methods in MEMS Design*, Lviv, Ukraine, 2007, pp. 12–14.
- [52] A. Izadian and P. Famouri, "Fault Diagnosis of MEMS Lateral Comb Resonators Using Multiple-Model Adaptive Estimators," *IEEE Transactions on Control Systems Technology*, vol. PP, no. 99, pp. 1–8, 2010.
- [53] A. Izadian, P. Khayyer, and P. Famouri, "Fault Diagnosis of Time-Varying Parameter Systems With Application in MEMS LCRs," *IEEE Transactions on Industrial Electronics*, vol. 56, no. 4, pp. 973–978, 2009.
- [54] H. Nguyen, C. Berbra, S. Lesecq, S. Gentil, A. Barraud, and C. Godin, "Diagnosis of an Inertial Measurement Unit Based on Set Membership Estimation," in *7th Mediterranean Conference on Control and Automation*, Thessaloniki, Greece, 2009, pp. 211–216.
- [55] O. Adrot, H. Janati-Idrissi, and D. Maquin, "Fault detection based on interval analysis," in *Proceedings of the 15th IFAC World Congress*, Barcelona, Spain, 2002, pp. 61–66.
- [56] C. Combastel and S. Raka, "A Set-Membership Fault Detection Test with Guaranteed Robustness to Parametric Uncertainties in Continuous Time Linear Dynamical Systems," in *Proceedings of the 7th IFAC Symposium on Fault Detection, Supervision and Safety of Technical Processes*, Barcelona, Spain, 2009, pp. 1192–1197.
- [57] G. Videau, T. Raissi, and A. Zolghadri, "Set-observer design for consistency checks of nonlinear systems," in *Proceedings of the 7th IFAC Symposium on Fault Detection, Supervision and Safety of Technical Processes*, Barcelona, Spain, 2009, pp. 1210–1215.

- [58] P. Wolf and V. Krebs, "Nonlinear Set Observation for Consistency-Based Diagnosis Using Implicit Interval Methods," in *Proceedings of the 7th IFAC Symposium on Fault Detection, Supervision and Safety of Technical Processes*, Barcelona, Spain, 2009, pp. 1204–1209.
- [59] J. Korbicz and M. Witczak, "Uncertain soft computing models in robust fault detection," in *Proceedings of the 1st Workshop on Networked Control System and Fault Tolerant Control(NeCST)*, Tsinghua University, P.R. China, 2005, pp. 199–205.
- [60] S. Oblak, I. Škrjanc, and S. Blažič, "Fault detection for nonlinear systems with uncertain parameters based on the interval fuzzy model," *Engineering Applications of Artificial Intelligence*, vol. 20, no. 4, pp. 503–510, 2007.
- [61] J. Quevedo, V. Puig, T. Escobet, R. Sarrate, F. Nejjari, and L. Travé-Massuyès, "The contribution of interval-based models to complex systems fault detection problems," in *Proceedings of the 7th IFAC Symposium on Fault Detection, Supervision and Safety of Technical Processes*, Barcelona, Spain, 2009, pp. 1126–1131.
- [62] J. Watkins and S. Yurkovich, "Fault detection using set-membership identification," in *Proceedings of the 1996 IFAC World Congress*, San Francisco, CA, USA, 1996, pp. 61–66.
- [63] M. Cheung, S. Yurkovich, and K. Passino, "An optimal volume ellipsoid algorithm for parameter set estimation," *IEEE Transactions on Automatic Control*, vol. 38, no. 8, pp. 1292–1296, 1993.
- [64] J. Gassman and S. Yurkovich, "An ellipsoid algorithm for parameter set estimation," in *IEEE Conference on Control Applications*, Dayton, OH, USA, 1992, pp. 835–840.
- [65] J. Watkins, "Parameter Set Estimation for Time Varying Systems," Ph.D. dissertation, Ohio State University, 1995.
- [66] K. Le, Z. Huang, C. Moon, and A. Tzes, "Adaptive thresholding- A robust fault detection approach," in *Proceedings of the 36th IEEE Conference on Decision and Control*, San Diego, CA, USA, 1997, pp. 4490–4495.
- [67] J. Deller, "Set membership identification in digital signal processing," *IEEE ASSP Magazine*, vol. 6, no. 4, pp. 4–20, 1989.
- [68] A. Tzes and K. Le, "Adaptive performance/robust control design using orthotopic set membership identification for low-dimensional systems," *International Journal Adaptive Control and Signal Processing*, vol. 11, no. 8, pp. 649–663, 1997.
- [69] —, "Fault detection for jump discrete systems," in *Proceedings of the IEEE American Control Conference*, San Diego, CA, USA, 1999, pp. 4496–4500.
- [70] A. Ingimundarson, J. Bravo, V. Puig, and T. Alamo, "Robust fault diagnosis using parallelotope-based set-membership consistency tests," in *Proceeding of the 44th IEEE Conference on Decision and Control*, Seville, Spain, 2005, pp. 993–998.
- [71] A. Ingimundarson, J. Bravo, V. Puig, T. Alamo, and P. Guerra, "Robust fault detection using zonotope-based set-membership consistency test," *International Journal of Adaptive Control and Signal Processing*, vol. 23, no. 4, pp. 1099–1115, 2008.
- [72] H. Witsenhausen, "Sets of possible states of linear systems given perturbed observations," *IEEE Transactions on Automatic Control*, vol. 13, no. 5, pp. 556 – 558, 1968.
- [73] F. Schweppe, "Recursive state estimation: Unknown but bounded errors and system inputs," *IEEE Transactions on Automatic Control*, vol. 13, no. 1, pp. 22 – 28, 1968.

## BIBLIOGRAPHY

---

- [74] E. Fogel and Y. Huang, "On the value of information in system identification—Bounded noise case," *Automatica*, vol. 18, no. 2, pp. 229–238, 1982.
- [75] M. Milanese and G. Belforte, "Estimation theory and uncertainty intervals evaluation in presence of unknown but bounded errors: Linear families of models and estimators," *IEEE Transactions on Automatic Control*, vol. 27, no. 2, pp. 408–414, 1982.
- [76] E. Walter and H. Piet-Lahanier, "Exact recursive polyhedral description of the feasible parameter set for bounded-error models," *IEEE Transactions on Automatic Control*, vol. 34, no. 8, pp. 911–915, 1989.
- [77] A. Vicino and G. Zappa, "Sequential approximation of feasible parameter sets for identification with set membership uncertainty," *IEEE Transactions on Automatic Control*, vol. 41, no. 6, pp. 774–785, 1996.
- [78] J. Bravo, T. Alamo, and E. Camacho, "Bounded error identification of systems with time-varying parameters," *IEEE Transactions on Automatic Control*, vol. 51, no. 7, pp. 1144–1150, 2006.
- [79] J. Deller Jr, S. Gollamudi, S. Nagaraj, D. Joachim, and Y. Huang, "Convergence analysis of the quasi-OBE algorithm and related performance issues," *International Journal of Adaptive Control and Signal Processing*, vol. 21, no. 6, pp. 499–527, 2007.
- [80] A. Kurzhanskiy and P. Varaiya, "Ellipsoidal Toolbox (ET)," in *Proceedings of the 45th IEEE Conference on Decision and Control*, San Diego, CA, USA, 2006, pp. 1498–1503.
- [81] T. Clement and S. Gentil, "Reformulation of parameter identification with unknown-but-bounded errors," *Mathematics and Computers in Simulation*, vol. 30, no. 3, pp. 257–270, 1988.
- [82] G. Belforte, "Parameter identification for models with bounded errors in all variables," *Systems and Control Letters*, vol. 19, no. 6, pp. 425–428, 1992.
- [83] V. Cerone and D. Regruto, "Parameter bounds for discrete-time Hammerstein models with bounded output errors," *IEEE Trans. on Automatic Control*, vol. 48, no. 10, pp. 1855–1860, 2003.
- [84] F. Chernous'ko, "Optimal Guaranteed Estimates of Indeterminacy With the Aid of Ellipsoids-Part I," *Engineering Cybernetics*, vol. 18, no. 4, pp. 1–9, 1980.
- [85] J. Watkins and S. Yurkovich, "Parameter set estimation algorithms for time-varying systems," *International Journal of Control*, vol. 66, no. 5, pp. 711–732, 1997.
- [86] A. Dax, "The distance between two convex sets," *Linear Algebra and its Applications*, vol. 416, no. 1, pp. 184–213, 2006.
- [87] V. Reppa and A. Tzes, "Fault Detection and Diagnosis relying on Set Membership Identification for Time-Varying Systems," in *Conference on Control and Fault-Tolerant Systems*, Nice, France, 2010, pp. (to appear, Paper FrA1.2).
- [88] —, "Fault Detection and Diagnosis based on Parameter Set Estimation," *IET Control Theory and Appl.*, 2010, (to appear).
- [89] V. Reppa, M. Vagia, and A. Tzes, "Fault Detection and Diagnosis Enhanced by a Reconfiguration Control Scheme for a Micro-Electrostatic Actuator," in *18th Mediterranean Conference on Control and Automation*, Marrakech, Morocco, 2010, pp. 477–482.
- [90] S. Boyd and L. Vandenberghe, *Convex optimization*. Cambridge University Press, 2004.



- [91] V. Reppa and A. Tzes, "Fault Detection and Diagnosis based on Parameter Set Estimation for Measurements corrupted by Bounded Noise," in *18th Mediterranean Conference on Control and Automation*, Marrakech, Morocco, 2010, pp. 460–465.
- [92] A. Vicino and G. Zappa, "Sequential approximation of parameter sets for identification with parametric and nonparametric uncertainty," in *Proceedings of the 32nd Conference on Decision and Control*, San Antonio, Texas, USA, 1993, pp. 2044–2049.
- [93] W. Reinelt, A. Garulli, and L. Ljung, "Comparing different approaches to model error modeling in robust identification," *Automatica*, vol. 38, no. 5, pp. 787–803, 2002.
- [94] J. P. Norton, "Identification and application of bounded-parameter models." *Automatica*, vol. 23, no. 4, pp. 497–507, 1987.
- [95] S. Gollamudi, S. Kapoor, S. Nagaraj, and Y. Huang, "Set-membership adaptive equalization and an updatator-shared implementation for multiple channel communications systems," *IEEE Transactions on Signal Processing*, vol. 46, no. 9, pp. 2372–2385, 1998.
- [96] G. Fedder, "Simulation of microelectromechanical systems," Ph.D. dissertation, University of California, Berkeley, May 1994.
- [97] R. Lin and W. Wang, "Structural dynamics of microsystems current state of research and future directions," *Mechanical Systems and Signal Processing*, vol. 20, no. 5, pp. 1015–1043, 2006.
- [98] Su, C. and Huang, L. and Prater, C. and Bhushan, B., "Torsional resonance microscopy and its applications," in *Applied Scanning Probe Methods V*. Springer Berlin Heidelberg, 2007, pp. 113–148.
- [99] Song, Y. and Bhushan, B., "Modeling of tip-cantilever dynamics in atomic force microscopy," in *Applied Scanning Probe Methods V*. Springer Berlin Heidelberg, 2007, pp. 149–223.
- [100] V. Reppa and A. Tzes, "Application of set membership identification for fault detection of MEMS," in *Proceedings 2006 IEEE International Conference on Robotics and Automation*, Orlando, FL, USA, 2006, pp. 643–648.
- [101] M. Vagia and A. Tzes, "Robust PID control design for an electrostatic micromechanical actuator with structured uncertainty," *IET Control Theory and Applications*, vol. 2, no. 5, pp. 365–373, 2008.
- [102] A. Izadian, L. Hornak, and P. Famouri, "Trajectory Control of MEMS Lateral Comb Resonators Under Faulty Conditions," in *Proceedings of American Control Conference*, New York City, USA, 2007, pp. 3198–3203.
- [103] V. Reppa, M. Vagia, and A. Tzes, "Fault Detection using Set Membership Identification for Micro-Electrostatic Actuators," in *IEEE International Conference on Control Applications*, Singapore, 2007, pp. 789–794.
- [104] V. Reppa and A. Tzes, "Fault Detection relying on Set-Membership techniques for an Atomic Force Microscope," in *7th IFAC Symposium on Fault Detection, Supervision and Safety of Technical Processes*, Barcelona, Spain, 2009, pp. 1186–1191.
- [105] Y. Tung and K. Kurabayashi, "A single-layer PDMS-on-silicon hybrid microactuator with multi-axis out-of-plane motion capabilities-Part I: design and analysis," *Journal of Microelectromechanical Systems*, vol. 14, no. 3, pp. 548–557, 2005.

## BIBLIOGRAPHY

---

- [106] A. Yurtsever, “Nanotribological surface characterization by frequency modulated torsional resonance mode afm,” Ph.D. dissertation, Ludwig-Maximilians University of Munich, Munich, March 2008.
- [107] R. Clough and J. Penzien, “Dynamics of structures, Third Edition,” 2003.
- [108] B. Bhushan, “Nanotribology and nanomechanics,” *Wear*, vol. 259, no. 7-12, pp. 1507–1531, 2005.
- [109] K. Chung, Y. Lee, D. Kim, J. Yoo, and S. Hong, “Tribological characteristics of probe tip and PZT media for AFM-based recording technology,” *IEEE Transactions on Magnetics*, vol. 41, no. 2, pp. 849–854, 2005.
- [110] H. Bhaskaran, A. Sebastian, and M. Despont, “Nanoscale PtSi tips for conducting probe technologies,” *IEEE Transactions on Nanotechnology*, vol. 8, no. 1, pp. 128–131, 2009.
- [111] V. Reppa and A. Tzes, “Fault Detection based on Orthotopic Set Membership Identification for Robot Manipulators,” in *in the Proceedings of the 17th IFAC World Congress*, Seoul, Korea, 2008, pp. 7344–7349.
- [112] K. Astrom and B. Wittenmark, *Adaptive control*. Addison-Wesley Longman Publishing Co., Inc. Boston, MA, USA, 1994.

## Appendix A

# Mathematical Auxiliary Analysis

### A.1 Computation of the Perturbation Ellipsoid

The perturbation ellipsoid  $\Theta^w$  is determined as the ellipsoid that outer bounds the perturbation orthotope given in (2.48). Two approaches are proposed for its computation;  $\Theta^w$  can be represented by the circle that crosses the vertices of  $\Omega^w$ , with its centroid  $w^c$  and shape matrix  $P^w$  computed as:

$$w^c = \left[ \frac{w_1^{\max} + w_1^{\min}}{2}, \dots, \frac{w_n^{\max} + w_n^{\min}}{2} \right]^T, \quad (\text{A.1})$$

$$P^w = \|W\|^2 I, \quad (\text{A.2})$$

$$W = \left[ \frac{w_1^{\max} - w_1^{\min}}{2}, \dots, \frac{w_n^{\max} - w_n^{\min}}{2} \right]^T, \quad (\text{A.3})$$

where  $I$  is the  $n \times n$  identity matrix. The second approach addresses that  $\Theta^w$  is defined as:

$$\Theta^w = \underset{\Theta}{\arg}[\min\{\text{vol}(\Theta) : \Theta \supset \Omega^w\}] \quad (\text{A.4})$$

Therefore,  $\Theta^w$  is computed as the Löwner-John ellipsoid of  $\Omega^w$ , whose center and shape matrix are the solutions of the optimization problem [90]:

$$\begin{aligned} \min \quad & \log(\det(Q^{-1})) \\ \text{s.t.} \quad & \|Q(V_{\Omega^w}^p - w^c)\| \leq 1, \quad p = 0, \dots, 2^n - 1, \end{aligned} \quad (\text{A.5})$$

where  $Q \in \mathbb{R}^{n \times n} \succ 0$ ,  $V_{\Omega^w}^p \in \mathbb{R}^n$  corresponds to the coordinates of the  $p$ th vertex of  $\Omega^w$  and  $P^w = (Q^T Q)^{-1}$

## A.2 Time Invariant Jump Linearly Parametrizable Model

The time invariant parameter vector case implies that

$$w(i) = \mathbf{0}_{n \times 1} \quad \forall i, \quad (\text{A.6})$$

$$\theta(i) = \theta(i-1) = \theta^\circ, \quad i < i^{f_1} \quad (\text{A.7})$$

Under the assumption  $i^{f_0} = 0$ ,  $\Delta\theta(i^{f_0}) = 0$  and according to (3.2) and (3.3) the following equations are valid

$$\begin{aligned} \theta^\circ(i^{f_1}) &= \theta^\circ(i^{f_1} - 1) + (\Delta\theta(i^{f_1}) - \Delta\theta(0)) = \theta^\circ + \Delta\theta(i^{f_1}), \\ \theta^\circ(i^{f_1} + 1) &= \theta^\circ(i^{f_1}) + (\Delta\theta(i^{f_1} + 1) - \Delta\theta(i^{f_1})) \stackrel{1}{=} \theta^\circ + \Delta\theta(i^{f_1}), \\ &\vdots \\ \theta^\circ(i^{f_1} + L_1^\circ - 1) &= \theta^\circ(i^{f_1} + L_1^\circ - 2) + (\Delta\theta(i^{f_1} + L_1^\circ - 1) - \Delta\theta(i^{f_1})) \stackrel{1}{\iff} \\ \theta^\circ(i^{f_2} - 1) &= \theta^\circ(i^{f_2} - 2) = \theta^\circ + \Delta\theta(i^{f_1}), \\ \theta^\circ(i^{f_2}) &= \theta^\circ(i^{f_2} - 1) + (\Delta\theta(i^{f_2}) - \Delta\theta(i^{f_1})) = \theta^\circ + \Delta\theta(i^{f_2}). \end{aligned}$$

In a more compact form,

$$\begin{aligned} \theta(i) &= \theta^\circ + \Delta\theta(i^{f_0}), \quad i^{f_0} \leq i < i^{f_1} \\ \theta^\circ(i) &= \theta^\circ + \Delta\theta(i^{f_1}), \quad i^{f_1} \leq i < i^{f_2}, \\ \theta^\circ(i) &= \theta^\circ + \Delta\theta(i^{f_2}), \quad i^{f_2} \leq i. \end{aligned}$$

Hence, the time invariant jump linearly parametrizable model is described as:

$$y(i) = \phi(i)^T (\theta^\circ + \Delta\theta(i^{f_{j-1}})), \quad \text{for } i^{f_{j-1}} \leq i < i^{f_j}$$

## A.3 Proof of Theorem II.3.6.2

The presence of  $\theta^\circ + \Delta\theta(i^{f_j})$  inside the ellipsoid  $\Theta(i^{f_j})$  implies that:

$$\mathcal{V} = \delta(i^{f_j}) \left[ \tilde{\theta}_2^T P(i^{f_j})^{-1} \tilde{\theta}_2 - 1 \right] \leq 0,$$

$\forall \delta(i^{f_j}) > 0$ , with

$$\tilde{\theta}_2 = \theta^\circ + \Delta\theta(i^{f_j}) - \theta^c(i^{f_j}). \quad (\text{A.8})$$

Taking into account (2.76), the previous equation is transformed to:

$$\begin{aligned}\tilde{\theta}_2 &= [\theta^\circ + \Delta\theta(i^{f_{j-1}}) - \theta^c(i^{f_j} - 1)] - \frac{\tau(i^{f_j})P(i^{f_j} - 1)\phi(i^{f_j})}{\sqrt{G(i^{f_j})}} + [\Delta\theta(i^{f_j}) - \Delta\theta(i^{f_{j-1}})] \\ &= \tilde{\theta}_1 - \frac{\tau(i^{f_j})P(i^{f_j} - 1)\phi(i^{f_j})}{\sqrt{G(i^{f_j})}} + \Delta\tilde{\theta}\end{aligned}\quad (\text{A.9})$$

where  $\Delta\tilde{\theta} = \Delta\theta(i^{f_j}) - \Delta\theta(i^{f_{j-1}})$  and  $G(i^{f_j}) = \phi(i^{f_j})^T P(i^{f_j} - 1)\phi(i^{f_j})$ . The expression of  $\mathcal{V}$  can be simplified as:

$$\begin{aligned}\mathcal{V} &= \delta(i^{f_j}) \left( \tilde{\theta}_1 - \frac{\tau(i^{f_j})P(i^{f_j} - 1)\phi(i^{f_j})}{\sqrt{G(i^{f_j})}} \right)^T P(i^{f_j})^{-1} \left( \tilde{\theta}_1 - \frac{\tau(i^{f_j})P(i^{f_j} - 1)\phi(i^{f_j})}{\sqrt{G(i^{f_j})}} \right) + \\ &\quad 2\delta(i^{f_j})\Delta\tilde{\theta}^T P(i^{f_j})^{-1} \left( \tilde{\theta}_1 - \frac{\tau(i^{f_j})P(i^{f_j} - 1)\phi(i^{f_j})}{\sqrt{G(i^{f_j})}} \right) + \delta(i^{f_j})\Delta\tilde{\theta}P(i^{f_j})^{-1}\Delta\tilde{\theta} - \delta(i^{f_j}) \\ &= \mathcal{V}_1 + \mathcal{V}_2 + \mathcal{V}_3 - \delta(i^{f_j}).\end{aligned}\quad (\text{A.10})$$

Using the matrix inversion lemma, (2.77) can be rewritten as:

$$P(i^{f_j})^{-1} = \frac{1}{\delta(i^{f_j})}P(i^{f_j} - 1)^{-1} - \frac{\sigma(i^{f_j}) - \delta(i^{f_j})}{\delta(i^{f_j})\sigma(i^{f_j})G(i^{f_j})}\phi(i^{f_j})\phi^T(i^{f_j}).\quad (\text{A.11})$$

Substituting  $P(i^{f_j})^{-1}$  into  $\mathcal{V}_1$  yields:

$$\begin{aligned}\mathcal{V}_1 &= \delta(i^{f_j}) \left( \tilde{\theta}_1 - \frac{\tau(i^{f_j})P(i^{f_j} - 1)\phi(i^{f_j})}{\sqrt{G(i^{f_j})}} \right)^T P(i^{f_j})^{-1} \left( \tilde{\theta}_1 - \frac{\tau(i^{f_j})P(i^{f_j} - 1)\phi(i^{f_j})}{\sqrt{G(i^{f_j})}} \right) \\ &= \tilde{\theta}_1^T P(i^{f_j} - 1)^{-1} \tilde{\theta}_1 - \frac{(\phi(i^{f_j})^T \tilde{\theta}_1)^2}{G(i^{f_j})} + \frac{\delta(i^{f_j})}{\sigma(i^{f_j})} \left( \frac{\phi(i^{f_j})^T \tilde{\theta}_1}{\sqrt{G(i^{f_j})}} - \tau(i^{f_j}) \right)^2.\end{aligned}$$

If  $\theta^\circ + \Delta\theta(i^{f_{j-1}}) \in \Theta(i^{f_j} - 1)$ , then  $\tilde{\theta}_1^T P(i^{f_j} - 1)^{-1} \tilde{\theta}_1 \leq 1$ , and  $-\frac{(\phi(i^{f_j})^T \tilde{\theta}_1)^2}{G(i^{f_j})} \leq 0$ , and

$$\mathcal{V}_1 \leq 1 + \frac{\delta(i^{f_j})}{\sigma(i^{f_j})} \left( \frac{\phi(i^{f_j})^T \tilde{\theta}_1}{\sqrt{G(i^{f_j})}} - \tau(i^{f_j}) \right)^2.\quad (\text{A.12})$$

## A. MATHEMATICAL AUXILIARY ANALYSIS

---

Similarly, using (A.11),  $\mathcal{V}_2$  is rewritten:

$$\begin{aligned}
\mathcal{V}_2 &= 2\delta(i^{f_j})\Delta\tilde{\theta}^T P(i^{f_j})^{-1} \left( \tilde{\theta}_1 - \frac{\tau(i^{f_j})P(i^{f_j}-1)\phi(i^{f_j})}{\sqrt{G(i^{f_j})}} \right) \\
&= 2\Delta\tilde{\theta}^T P(i^{f_j}-1)^{-1} \tilde{\theta}_1 - 2\Delta\tilde{\theta}^T \phi(i^{f_j}) \left( \frac{\sigma(i^{f_j}) - \delta(i^{f_j})}{\sigma(i^{f_j})\sqrt{G(i^{f_j})}} \left( \frac{\phi^T(i^{f_j})\tilde{\theta}_1}{\sqrt{G(i^{f_j})}} \right) \right) - \\
&\quad 2\Delta\tilde{\theta}^T \phi(i^{f_j}) \left( \frac{\delta(i^{f_j})\tau(i^{f_j})}{\sigma(i^{f_j})\sqrt{G(i^{f_j})}} \right) \\
&\leq \alpha_2 \|\Delta\tilde{\theta}\|, \tag{A.13}
\end{aligned}$$

where  $\alpha_2 = 2 \left| \frac{\sigma(i^{f_j}) - \delta(i^{f_j})}{\sigma(i^{f_j})\sqrt{G(i^{f_j})}} \left( \frac{\phi^T(i^{f_j})\tilde{\theta}_1}{\sqrt{G(i^{f_j})}} \right) + \frac{\delta(i^{f_j})\tau(i^{f_j})}{\sigma(i^{f_j})\sqrt{G(i^{f_j})}} \right| \|\phi(i^{f_j})\| + 2 \frac{\sqrt{\lambda_{\max}[P(i^{f_j}-1)]}}{\lambda_{\min}[P(i^{f_j}-1)]}$ . In a similar manner,

$$\mathcal{V}_3 \delta(i^{f_j}) \Delta\tilde{\theta}^T P(i^{f_j})^{-1} \Delta\tilde{\theta} \leq \frac{\delta(i^{f_j})}{\lambda_{\min}[P(i^{f_j})]} \|\Delta\tilde{\theta}\|^2 = \alpha_1 \|\Delta\tilde{\theta}\|^2. \tag{A.14}$$

Hence,  $\theta^\circ + \Delta\theta(i^{f_j}) \in \Theta(i^{f_j})$  if  $\mathcal{V} = \mathcal{V}_1 + \mathcal{V}_2 + \mathcal{V}_3 - \delta(i^{f_j}) \leq 0$ , or if

$$\alpha_1 \|\Delta\tilde{\theta}\|^2 + \alpha_2 \|\Delta\tilde{\theta}\| + \alpha_3 \leq 0 \tag{A.15}$$

where  $\alpha_3 = 1 + \frac{\delta(i^{f_j})}{\sigma(i^{f_j})} \left( \frac{\phi(i^{f_j})^T \tilde{\theta}_1}{\sqrt{G(i^{f_j})}} - \tau(i^{f_j}) \right)^2 - \delta(i^{f_j})$ . Inequality (A.15) is a quadratic one in terms of  $\|\Delta\tilde{\theta}\| = \|\Delta\theta(i^{f_j}) - \Delta\theta(i^{f_j-1})\|$  and has a solution if the inequalities noted in Theorem 3.6.2 are satisfied.

### A.4 Computation of Modal-Shape of Torsional Resonant AFM

The undamped free torsional vibration of the cantilever is described by:

$$GJ \frac{\partial^2 \psi(x,t)}{\partial x^2} = \rho I \rho \frac{\partial^2 \psi(x,t)}{\partial t^2}. \tag{A.16}$$

The variables can be separated using

$$\psi(x,t) = \xi(x)\Psi(t). \tag{A.17}$$

Substitution of (A.17) into (A.16) and dividing with  $\xi(x)\Psi(t)$  leads to:

$$\frac{d^2 \xi(x)}{dx^2} \frac{1}{\xi(x)} = \frac{\rho I \rho}{GJ} \frac{\ddot{\Psi}(t)}{\Psi(t)}. \tag{A.18}$$

---

#### A.4 Computation of Modal-Shape of Torsional Resonant AFM

---

Because the left-hand side of this equation is a function of  $x$  only and the right one is a function of  $t$  only, the entire equation can be satisfied for arbitrary values of  $x$  and  $t$  only if each term is a constant in accordance with

$$\frac{d^2\xi(x)}{dx^2} \frac{1}{\xi(x)} = \frac{\rho I_\rho}{GJ} \ddot{\Psi}(t) \frac{1}{\Psi(t)} = -\beta_\psi^2, \quad (\text{A.19})$$

where the single constant involved is designated in the form  $\beta_\psi^2$  for later mathematical convenience. This equation yields two ordinary differential equations:

$$\ddot{\Psi}(t) + \omega^2 \Psi(t) = 0, \quad (\text{A.20})$$

$$\frac{d^2\xi(x)}{dx^2} + \beta_q^2 \xi(x) = 0 \quad (\text{A.21})$$

in which  $\omega_q^2 \equiv \frac{GJ}{\rho I_\rho} \beta_q^2$ . Equation (A.20) is the well known undamped one-degree-of-freedom harmonic oscillator. The solution of (A.21) is:

$$\xi(x) = a_0 \sin(\beta_q x) + b_0 \cos(\beta_q x). \quad (\text{A.22})$$

Considering the clamped and free boundary conditions,  $\xi(x)|_{x=0} = 0$ ,  $GJ \frac{d\xi(x)}{dx} \Big|_{x=L_c} = 0$ , the following characteristic equation is obtained

$$\cos(\beta_q L_c) = 0, \quad (\text{A.23})$$

yielding in:

$$\beta_q = \frac{(2q-1)\pi}{2L_c}, \quad (\text{A.24})$$

$$\omega_q = \frac{(2q-1)\pi}{2L_c} \sqrt{\frac{GJ}{\rho I_\rho}}. \quad (\text{A.25})$$

Finally, the torsional modal shape is given as:

$$\xi(x) = a_0 \sin(\beta_q x), \quad (\text{A.26})$$

where  $a_0$  is an arbitrary constant.

---

## A. MATHEMATICAL AUXILIARY ANALYSIS

---

Based on the previous analysis,  $M^*$ ,  $\mathcal{L}^*$ ,  $\xi_q(L_c)$ ,  $\xi_q(L_c)^2$  are computed as:

$$\xi_q(L_c) = a_0 \sin\left(\frac{(2q-1)\pi}{2}\right) = \begin{cases} a_0, & \text{if } q \text{ is odd} \\ -a_0, & \text{if } q \text{ is even} \end{cases}, \quad (\text{A.27})$$

$$\xi_q(L_c)^2 = a_0^2 \sin^2\left(\frac{(2q-1)\pi}{2}\right) = a_0^2, \quad (\text{A.28})$$

$$\begin{aligned} \mathcal{L}^* &= \int_0^{L_c} \rho I_\rho \xi_q(x) dx = \rho I_\rho a_0 \int_0^{L_c} \sin(\beta_q x) dx = \rho I_\rho a_0 \left[ -\frac{1}{\beta_q} \cos(\beta_q x) \right]_0^{L_c} \\ &= \rho I_\rho a_0 \left[ -\frac{1}{\beta_q} \cos(\beta_q L_c) + \frac{1}{\beta_q} \right]_0^{L_c} = \frac{\rho I_\rho a_0}{\beta_q}, \end{aligned} \quad (\text{A.29})$$

$$\begin{aligned} M_q^* &= \int_0^{L_c} \rho I_\rho \xi_q(x)^2 dx = \rho I_\rho a_0^2 \int_0^{L_c} \sin^2(\beta_q x) dx = \rho I_\rho a_0^2 \left[ \frac{x}{2} - \frac{1}{4\beta_q} \sin(2\beta_q x) \right]_0^{L_c} \\ &= \rho I_\rho a_0^2 \left( \frac{L_c}{2} - \frac{1}{4\beta_q} \sin(2\beta_q L_c) \right) = \rho I_\rho a_0^2 \left( \frac{L_c}{2} - \frac{1}{4\beta_q} \sin\left(2\frac{(2q-1)\pi}{2L_c} L_c\right) \right) \\ &= \frac{\rho I_\rho a_0^2 L_c}{2}. \end{aligned} \quad (\text{A.30})$$

**Orthogonality Relationship:** For  $\omega_q \neq \omega_p$ , the modal shape  $\xi(x)$  satisfies the orthogonality relationship:

$$\begin{aligned} \int_0^{L_c} \xi_q(x) \xi_p(x) dx &= \int_0^{L_c} a_0^2 \sin(\beta_q x) \sin(\beta_p x) dx = a_0^2 \left[ \frac{\sin((\beta_q - \beta_p)x)}{2(\beta_q - \beta_p)} - \frac{\sin((\beta_q + \beta_p)x)}{2(\beta_q + \beta_p)} \right]_0^{L_c} \\ \beta_q - \beta_p &= \frac{(2q-1)\pi}{2L_c} - \frac{(2p-1)\pi}{2L_c} = \frac{(2q-1-2p+1)\pi}{2L_c} = \frac{2(q-p)\pi}{2L_c} = \frac{(q-p)\pi}{L_c}, \\ \beta_q + \beta_p &= \frac{(2q-1)\pi}{2L_c} + \frac{(2p-1)\pi}{2L_c} = \frac{(2q-1+2p-1)\pi}{2L_c} = \frac{2(q+p-1)\pi}{2L_c} = \frac{(q+p-1)\pi}{L_c} \end{aligned}$$

implying that

$$\int_0^{L_c} \xi_q(x) \xi_p(x) dx = a_0^2 \left( \frac{\sin\left(\frac{(q-p)\pi}{L_c} L_c\right)}{2\left(\frac{(q-p)\pi}{L_c}\right)} - \frac{\sin\left(\frac{(q+p-1)\pi}{L_c} L_c\right)}{2\left(\frac{(q+p-1)\pi}{L_c}\right)} \right) = 0. \quad (\text{A.31})$$



## Appendix B

# Algorithms

### B.1 OVE-based Algorithms

---

**Algorithm 1** Ellipsoid Computation using Data-Hyperstrips

---

1.  $\bar{\alpha}(i) \leftarrow \min \left( \frac{y^m(i) - \phi^m(i)^T \hat{\theta}^c(i) + \bar{e}^{\max}(i)}{\sqrt{\phi^m(i)^T \hat{P}(i) \phi^m(i)}}, 1 \right)$ ,  $\underline{\alpha}(i) \leftarrow \max \left( \frac{y^m(i) - \phi^m(i)^T \hat{\theta}^c(i) - \bar{e}^{\max}(i)}{\sqrt{\phi^m(i)^T \hat{P}(i) \phi^m(i)}}, -1 \right)$
  2. **if**  $\bar{\alpha}(i) \leq -1$  **or**  $\underline{\alpha}(i) \geq 1$  **then**
  3.   there is no feasible parameter set and the algorithm stops
  4. **else**
  5.   **if**  $\bar{\alpha}(i)\underline{\alpha}(i) \leq -\frac{1}{n}$  **then**
  6.      $\theta^c(i) \leftarrow \hat{\theta}^c(i)$  and  $P(i) \leftarrow \hat{P}(i)$
  7.   **else**
  8.     **if**  $|\bar{\alpha}(i) + \underline{\alpha}(i)| \leq 2\mu_o$ ,  $\mu_o \simeq 0$  **then**
  9.        $\alpha(i) \leftarrow \max(|\underline{\alpha}(i)|, |\bar{\alpha}(i)|)$ ,  $\tau(i) \leftarrow 0$   
        $\sigma(i) \leftarrow n\alpha(i)^2$ ,  $\delta(i) \leftarrow \frac{n(1-\alpha(i)^2)}{n-1}$
  10.   **else**
  11.      $\beta(i) \leftarrow n(\bar{\alpha}(i) + \underline{\alpha}(i)) + \frac{2(1+\bar{\alpha}(i)\underline{\alpha}(i))}{\bar{\alpha}(i)+\underline{\alpha}(i)}$   
        $\tau(i) \leftarrow \frac{\beta(i) - \text{sign}\left(\frac{\bar{\alpha}(i)+\underline{\alpha}(i)}{2}\right)\sqrt{\beta(i)^2 - 4(n+1)(1+n\bar{\alpha}(i)\underline{\alpha}(i))}}{2(n+1)}$   
        $\sigma(i) \leftarrow \tau(i)[\tau(i) - \beta(i) + n(\bar{\alpha}(i) + \underline{\alpha}(i))] + 1$   
        $\delta(i) \leftarrow \frac{\sigma(i)}{1 - \frac{2\tau(i)}{\bar{\alpha}(i)+\underline{\alpha}(i)}}$
  12.   **end if**
  13.    $\theta^c(i)$ ,  $(P(i))$  is computed using (2.76) and (2.77)
  14. **end if**
  15. **end if**
-

## B. ALGORITHMS

---



---

### Algorithm 2 Ellipsoid Computation using Data-Hypersectors

---

1.  $\bar{\alpha}(i) \leftarrow \min\left(\frac{y^m(i) - \phi^B(i)^T \hat{\theta}^c(i) + \bar{e}^{\max}(i)}{\sqrt{\phi^B(i)^T \hat{P}(i) \phi^B(i)}}, 1\right)$ ,  $\underline{\alpha}(i) \leftarrow \max\left(\frac{y^m(i) - \phi^A(i)^T \hat{\theta}^c(i) - \bar{e}^{\max}(i)}{\sqrt{\phi^A(i)^T \hat{P}(i) \phi^A(i)}}, -1\right)$
  2. **if**  $\bar{\alpha}(i) \leq -1$  or  $\underline{\alpha}(i) \geq 1$  **then**
  3.   there is no feasible parameter set and the algorithm stops
  4. **else**
  5.   **if**  $\bar{\alpha}(i) = -1$  and  $\underline{\alpha}(i) = 1$  **then**
  6.      $\theta^c(i) \leftarrow \hat{\theta}^c(i)$  and  $P(i) \leftarrow \hat{P}(i)$
  7.   **else**
  8.     **if**  $\bar{\alpha}(i) = 1$  and  $-1 < \underline{\alpha}(i) < 1$  **then**
  9.        $\tau(i)$ ,  $\delta(i)$ ,  $\sigma(i)$  are computed through Steps 8–12 of Algorithm 1 and  $\theta^c(i)$ ,  $P(i)$  through Step 13 using  $\phi^A(i)$  instead of  $\phi^m(i)$  in (2.76) and (2.77)
  10.    **else if**  $\underline{\alpha}(i) = -1$  and  $-1 < \bar{\alpha}(i) < 1$  **then**
  11.       $\tau(i)$ ,  $\delta(i)$ ,  $\sigma(i)$  are computed through Steps 8–12 of Algorithm 1 and  $\theta^c(i)$ ,  $P(i)$  through Step 13 using  $\phi^B(i)$  instead of  $\phi^m(i)$  in (2.76) and (2.77)
  12.    **else if**  $-1 < \underline{\alpha}(i) < 1$  and  $-1 < \bar{\alpha}(i) < 1$  **then**
  13.       $\bar{\alpha}(i) \leftarrow 1$
  14.       $\tau(i)$ ,  $\delta(i)$ ,  $\sigma(i)$  are computed through Steps 8–12 of Algorithm 1
  15.       $\theta^{c'}(i) \leftarrow \hat{\theta}^c(i) + \frac{\tau(i) \hat{P}(i) \phi^A(i)}{\sqrt{\phi^A(i)^T \hat{P}(i) \phi^A(i)}}$ ,  
 $P'(i) \leftarrow \delta(i) \hat{P}(i) + [\sigma(i) - \delta(i)] \frac{\hat{P}(i) \phi^A(i) \phi^A(i)^T \hat{P}(i)}{\phi^A(i)^T \hat{P}(i) \phi^A(i)}$
  16.       $\underline{\alpha}(i) \leftarrow -1$ ,  $\bar{\alpha}(i) \leftarrow \min\left(\frac{y^m(i) - \phi^B(i)^T \theta^{c'}(i) + \bar{e}^{\max}(i)}{\sqrt{\phi^B(i)^T P'(i) \phi^B(i)}}, 1\right)$
  17.      **if**  $\bar{\alpha}(i) \leq -1$  **then**
  18.       there is no feasible parameter set and the algorithm stops
  19.      **else**
  20.        $\tau(i)$ ,  $\delta(i)$ ,  $\sigma(i)$  are computed through Steps 8–12 of Algorithm 1
  21.        $\theta^c(i) \leftarrow \theta^{c'}(i) + \frac{\tau(i) P'(i) \phi^B(i)}{\sqrt{\phi^B(i)^T P'(i) \phi^B(i)}}$ ,  
 $P(i) \leftarrow \delta(i) P'(i) + [\sigma(i) - \delta(i)] \frac{P'(i) \phi^B(i) \phi^B(i)^T P'(i)}{\phi^B(i)^T P'(i) \phi^B(i)}$
  22.      **end if**
  23.    **end if**
  24.    **end if**
  25. **end if**
-

## B.2 Backward-in-Time Fault Detection Algorithm

---

**Algorithm 3** Backward-in-Time Fault Detection

---

1.  $\{\mathcal{Z} = \Omega$  in orthotopic FDD and  $\mathcal{Z} = \Theta$  in ellipsoidal FDD}
  2.  $m_1 = 1, m_2 = 0$
  3. **repeat**
  4.  $k = i^{d_j} - m_1$
  5.  $\mathcal{Z}(k-1) \leftarrow \mathcal{Z}^r(k-1)$  using the orthotopic or ellipsoidal resetting procedure according to Theorem (3.5.1) or (3.5.2)
  6. **repeat**
  7.  $\mathcal{Z}(k+m_2) \leftarrow \mathcal{Z}(k+m_2-1) \cap \mathcal{Z}(k+m_2)$  via the OVE-algorithm
  8.  $m_2 = m_2 + 1$
  9. **until**  $\mathcal{Z}(k+m_2) \neq \emptyset$ , OR  $m_2 > L_1 + m_1$
  10.  $m_1 = m_1 + 1$
  11. **until**  $m_1 > L$ , or  $m_2 = L_1 + m_1 - 1$
  12. The fault occurrence is at  $i^{f_j} \leq k$
-